Quantum entanglement generation in trapped ions using coherent and dissipative methods

by

Yiheng Lin

B.S., University of Science and Technology of China, 2009

M.S., University of Colorado Boulder, 2012

A thesis submitted to the

Faculty of the Graduate School of the

University of Colorado in partial fulfillment

of the requirements for the degree of

Doctor of Philosophy

Department of Physics

2015

This thesis entitled:
Quantum entanglement generation in trapped ions using coherent and dissipative methods
written by Yiheng Lin
has been approved for the Department of Physics

David J. Wineland

James Thompson

Date ________________

The final copy of this thesis has been examined by the signatories, and we find that both the content and the form meet acceptable presentation standards of scholarly work in the above mentioned discipline.

Lin, Yiheng (Ph.D., Physics)

Quantum entanglement generation in trapped ions using coherent and dissipative methods

Thesis directed by Prof. Dr. David J. Wineland

Entangled states are a key resource in fundamental quantum physics, quantum cryptography, and quantum computation. In this thesis, we focus on the demonstrations of two novel methods to generate entanglement. First, we implement dissipative production of a maximally entangled steady state on two trapped ions. Dissipative and coherent processes are combined and implemented in a continuous time-independent fashion, analogous to optical pumping of atomic states, continuously driving the system towards the steady entangled state. With this method, we obtain a Bell state fidelity up to 0.89(2). Second, we propose and demonstrate a novel coherent process to confine quantum evolution in a subspace between an initial separable state and the target entangled state. We demonstrate this scheme on two and three ions obtaining a Bell state fidelity up to 0.992(2). Both of these methods are robust against certain types of experimental noise and decoherence. Additionally, we demonstrate sympathetic cooling of ion chains to near the ground state of motion with an electromagnetically-induced-transparency (EIT) method. This results in roughly an order of magnitude faster cooling time while using significantly lower laser power compared to the conventional resolved sideband cooling method. These techniques may be helpful for scaled-up quantum computing.

Dedication

To my parents, grandparents, my wife, my teachers and mentors.

Acknowledgements

Many people deserves acknowledgement to this work and I apologize in advance in case I unintentionally leave anyone out.

It has been a great honor to work in the ion storage group at National Institute of Standards and Technology (NIST) at Boulder Colorado. When I joined the group at April 2010, I had background on theoretical physics and nuclear magnetic resonance (NMR) quantum information processing but I was a complete novice to trapped ion experiments, simply being interested in it. I am very grateful to my advisor Dave Wineland who gave me an opportunity to work in the group. There I met and learnt a lot from many talented and skilled people, and I also had a good time with them. Dave Wineland is also a great advisor. We had a lot of freedom to work on the interesting projects and can choose our own way to tackle the problems, yet he is always ready to help with his massive knowledge and always able to directly or indirectly point out ways to solution. Together I need to thank Dietrich Leibfried, another advisor in our projects who constantly gave us suggestions and guidance, and he provides great help with his expertise in both experiments and theories.

I need to thank my colleagues who worked closely with me in the projects. Special thanks to John Gaebler, who had been the only postdoc in our lab for very long time. He played a crucial role in all the experiments I led or participated in, and he is always generously sharing his knowledge and willing to help. During my first year in the lab, David Hanneke, Jonathan Home and John Jost helped me learn how an ion trap works and operates, from the basics to details. Special thanks to David who helped me become an experimentalist from mostly a theorist and get through this difficult transition. I also need to thank Ryan Bowler, Ting Rei Tan and Yong Wan, with whom

we helped each other on the experiments and beyond.

I also need to express my gratitude to our theoretical collaborators. Special thanks to Florentin Reiter and Anders S. Sørensen from University of Copenhagen, who collaborated on two experiments out of the three I led. Special thanks to Florentin for his expertise and being considerate. Without John Gaebler seeing Florentin's poster at the 2012 Gordon Research Conference and we then met, you may see a very different and perhaps less interesting thesis. I also thank Adam Keith, Emanual (Manny) Knill, Scott Glancy and Kevin Coakley for nice theoretical collaborations at NIST. Special thanks to Manny for all the discussion with him and his insights.

I am also very fortunate meeting these people from whom I leant a lot of experimental skills, and I appreciate their helps and the good time we together: Jason Amini, David Allcock, James C. Bergquist, Mike Biercuk, Brad Blakestad, Justin Bohnet, John Bollinger, Samuel Brewer, Joe Britton, Kenton Brown, Shaun Burd, Peter Burns, Jwo-Sy Chen, James Chou, Kevin Chou, Yves Colombe, Shon Cook, Robert Drullinger, Aaron Hankin, Dustin Hite, David Hume, Wayne Itano, Robert Jördens, Chris Langer, David Leibrandt, Yiheng Lin[1] , Katherine McCormick, Kyle McKay, Christian Ospelkaus, Dave Pappas, Till Rosenband, Brian Sawyer, Daniel Slichter, Raghavendra(Raghu) Srinivas, Carson Teale, Mike Thorpe, Susanna Todaro, Herman Uys, Aaron VanDevender, Ulrich Warring, and Andrew Wilson.

I need to thank my wife Xinchen, my parents and my grandparents, for their care and supports. Also I wanted to list all of my friends during my time in graduate school but here I would specially thank a few of these people, without their support and encourage I could not make it to the finish line: Dong Chen, Jiayan (Phoenix) Dai, Huiling Guo, Liqian Peng, Shuangwen Sheng, Jianfeng Xie, Honghua Yang, Pen-li (Ben) Yu, Yanbao Zhang, and Xiaoge Zeng, etc.

Finally, I need to thank my undergraduate advisors Xinhua Peng and Jiangfeng Du, who showed me the path to the interesting quantum phenomenon; and Luyuan Hao who showed me some basics of optics experiments. I also need to thank my teachers who help building my foundations of knowledge, specially: Guanghua Xu, Bingguang Wu, Liping Lin, Wenyan Sheng.

---

[1] Ah you are reading it carefully

Special thanks to Dave Wineland, Raghu Srinivas and Yong Wan who read this thesis in detail and provided a lot of helpful comments.

Contents

Chapter

1 Introduction 1

1.1 General description of quantum information and entanglement 1

1.2 Scalable quantum computing architecture and sympathetic cooling 4

1.3 General description of entanglement operation and novel methods 6

1.4 Thesis organization 8

2 Ion trapping 9

2.1 Idealised ion trapping theory 9

2.2 Trap configurations 12

2.2.1 Trap wafers 13

2.2.2 Trap RF 14

2.2.3 The linear trap and the junction trap 14

2.3 Other components for ion trapping 15

2.3.1 Ion loading: atom source and photoionization 15

2.3.2 Vacuum system 19

2.3.3 Imaging system 20

2.3.4 Magnetic field coils 22

2.3.5 Experiment controls 23

3 ^{9}Be$^+$ qubit 25

3.1 ^{9}Be$^+$ energy levels . . . 25

3.2 Laser and microwave sources . . . 30

3.3 State initialization . . . 36

3.4 Detection . . . 38

3.4.1 Photon collection . . . 38

3.4.2 Maximal likelihood method . . . 39

3.4.3 Symmetric entangled state detections . . . 42

4 Internal-motional state coupling 44

4.1 Quantization of motional modes . . . 44

4.2 Resolved sideband coupling . . . 46

4.2.1 Electric dipole transition for a free ion . . . 48

4.2.2 Raman transition . . . 49

4.2.3 Raman sideband coupling . . . 51

4.2.4 Raman sideband coupling for two ions: resonant case . . . 52

4.2.5 Raman sideband coupling for two ions: detuned case . . . 53

5 Sympathetic electromagnetically-induced-transparency(EIT) laser cooling 56

5.1 General description of sympathetic laser cooling . . . 57

5.2 Theoretical description of sympathetic EIT cooling . . . 58

5.2.1 EIT effect on a stationary ion . . . 58

5.2.2 EIT effect with a trapped ion in motion . . . 59

5.3 Experiment sympathetic EIT laser cooling . . . 62

5.3.1 EIT cooling on the ^{9}Be$^+$-^{24}Mg$^+$ ion pair . . . 63

5.3.2 EIT cooling on the ^{9}Be$^+$-^{24}Mg$^+$-^{24}Mg$^+$-^{9}Be$^+$ four-ion chain . . . 64

5.3.3 Technical notes for EIT laser cooling . . . 67

5.4 Conclusion and future applications . . . 69

5.5 Appendix: derivation for EIT cooling condition 69

6 Steady state entanglement from dissipation 71

6.1 Theory and concepts 72

6.2 Experimental setup and results 75

6.2.1 Continuous application 76

6.2.2 Stepwise Application 79

6.2.3 Numerical Simulation 83

7 Entanglement generation by confining dynamics in a subspace 89

7.1 Introduction 89

7.2 Two ion implementation 91

7.3 Two ion implementation with a composite pulse sequence 95

7.4 Three ion implementation 97

8 Conclusion 99

Bibliography 101

Tables

Table

3.1 Some field insensitive points with the relevant transitions and frequencies, and the difference of second order sensitivities. Here we list only field-insensitive points for B in the range of 11 mT to 180 mT. In this thesis we mainly work on fields for the first two entries, with $\Delta m_F = \pm 1$. For the higher fields the insensitive points are located at $\Delta F = 0$ transitions, and the higher order field sensitivity is significantly lower than the $\Delta F \neq 0$ insensitive transitions. As this trend and Fig. 3.2 shows, for the high fields, the Zeeman effect is dominant over the hyperfine coupling $hA\mathbf{I}\cdot\mathbf{J}$, and the field sensitivity between $\Delta F = 0$ transitions becomes small. At higher fields of ~819.439 mT, a 303 MHz field insensitive transition between $|m_I = -\frac{3}{2}, m_J = \frac{1}{2}\rangle \leftrightarrow |-\frac{1}{2}, \frac{1}{2}\rangle$ has been demonstrated in a Penning trap [1] for applications as a frequency standard. 29

3.2 List of $2s\ ^2S_{1/2}$ ground states expanded in the $|m_I, m_J\rangle$ basis, with coefficients rounded to the third digit. Compared with the states at zero field, except for the stretch states, the other states have modified coefficients. This table will be useful when calculating the coupling coefficients for the electric dipole transitions, since the selection rules are such that $\Delta m_I = 0$ and $\Delta m_J = 0, \pm 1$. 29

3.3 List of $2p\ ^2P_{1/2}$ states expanded in the $|m_I, m_J\rangle$ basis. Definitions are similar to Table 3.2 for $2p\ ^2P_{1/2}$. These components will be useful when describing the laser dipole coupling matrix element in this thesis. 30

3.4 typical π time of the Rabi flopping of the microwave transitions 36

4.1 Normal motional modes for various ion chain configurations, with the same external potential well for each case. The mode amplitudes are shown consistent with the ion order. For the $^{9}\mathrm{Be}^{+}-{}^{24}\mathrm{Mg}^{+}$ pair, due to the mass imbalance, the COM mode is dominated by motion of the $^{24}\mathrm{Mg}^{+}$ ion, while the stretch mode is dominated by the $^{9}\mathrm{Be}^{+}$ ion. This reduces the sympathetic cooling efficiency of mix-species chains for the modes which the coolant ion has small mode amplitudes. The mode information shown in this table will be useful for the experiments described in the following chapters. 47

6.1 list of parameters for repumping, cooling and heating processes 76

6.2 list of parameters for spontaneous photon scattering processes from Raman laser beams; we use the same numbers for simulation in both the continuous and stepwise cases. 86

6.3 fit values from the Stark experiment decaying flopping 88

Figures

Figure

1.1 A scalable quantum information processing device with trapped ions [2]. The structure consists of linear trapping sections, and junctions. Ions are trapped in long chains, separated, shuttled and recombined. Lasers beams are shown to entangle ion pairs. 5

2.1 Schematic for trapped ion experiment, showing the major components and some more details and requirements of technology therein. 10

2.2 An idealised ion trap with "four-rod" configuration. The gold rods are the RF electrodes, and the segmented ones are DC electrodes. The two RF electrodes are typically shorted together, and provide a quadruple confinement potential in the radial plane. To form confinement of positively charged ions along the axial direction, we apply positive potentials on the outer electrodes and lower potentials on the center electrodes. The axial confinement is designed to be weaker than the radial confinement, so that the ions are trapped along as a linear chain along $\hat{z}$. 11

2.3 View of the linear trap [3]. Only the top wafer is visible. The RF electrode and the segmented DC electrodes are shown, and the DC electrodes are gold ribbon bonded to the filter boards. The bottom figure represents a closed view of the segmented electrodes. The widths of the electrodes from left (O1) to right (L2) are {2,0.2,0.1,0.2,0.36,0.5,0.5,2}mm [3]. The small gaps between the electrodes are 0.02 mm. The electrodes O1-O2 form the experiment region; the electrodes L1-L2 form the loading region. The gap between the DC and RF electrodes in the experiment/loading region is 0.2/0.4 mm wide. 16

2.4 Close view of the junction trap. Only the top wafer is visible. The RF electrode and the segmented DC electrodes are shown, and the DC electrodes are gold-wire-bonded to the filter boards. The bottom figure represents the scale of the segmented electrodes. $\mathcal{L}$, $\mathcal{E}$, $\mathcal{V}$, $\mathcal{F}$, and $\mathcal{C}$ represents the loading zone, the experiment zone, the vertical zone, the “far” zone, and the center of the junction, respectively. The width of the electrode at $\mathcal{E}$ is 200 μm. The narrower electrode next to it is 100 μm wide, specifically for ion separation. The gaps between the electrodes are 20 μm wide. Ions chains can be separated and shuttled back and forth through two different routes, either $\mathcal{E} \to \mathcal{C} \to \mathcal{V} \to \mathcal{C} \to \mathcal{E}$ or $\mathcal{E} \to \mathcal{C} \to \mathcal{F} \to \mathcal{C} \to \mathcal{E}$, and thus enabling ion chain reordering [4]. The inset shows a side view of the junction and connection of the RF electrodes. 17

2.5 Schematic for the ^{9}Be photoionization laser setup. The mirror mount in dash outlines is a pick off mirror, which is not in the setup except for checking spectrum for 705 nm light. The mirror at the output of the tripler has finite transmission that leaks a small portion of 235 nm light for wavelength monitoring. 19

2.6 A mock up of the vacuum setup [3], showing relevant vacuum components. The Quartz cell has six windows made from fused silica for UV light access, and four of them are used for laser access and one is used for imaging. On the input end of the resonator, there is a cylindrical component to connect the center conductor to the ground. The output of the RF source after the amplifier is connected to a small wire loop, mounted inside the can to couple RF power into the resonator. 21

3.1 Schematic for the $^9\text{Be}^+$ ion electronic transitions at 11.9446 mT magnetic field. Laser beams are shown to address various levels, see text. The relevant energy splittings are shown, and the transition $|2,0\rangle \leftrightarrow |1,1\rangle$ with transition frequency 1207.495843 MHz is to first order insensitive to magnetic field fluctuations. A typical Raman laser configuration driving the qubit transition is shown. At 11.9642 mT magnetic field, there is another first order field insensitive transition $|2,1\rangle \leftrightarrow |1,0\rangle$ of frequency 1207.352808 MHz. 26

3.2 a) Energy levels in unit of (h GHz) by diagonalizing Hamiltonian in Eq. 3.1 over the external magnetic field B in mT. The eigenstates are labeled in the format of $|F, m_F\rangle$. For $B \neq 0$, F is no longer a good quantum number although m_F is. Here we just label the levels with the order of the energies, in conjunction with the low field case. b) The energy sensitivity $\frac{dE}{dB}$ in the unit of (h MHz/mT) over the external magnetic field. 28

3.3 Schematic for laser access to the trap, not to scale. The magnetic field coil is set so that the magnetic field is 45° with respect to the trap axis. Be CO and 90 denote the Raman laser beams to address the $^9\text{Be}^+$ ion. PI denotes the photoionization beams. Blue hollow squares denote the outline of the glass chamber and the windows. Figure adapted from [5]. 32

3.4 Schematic for BD laser beams setup. The output of the doubler has a vertical polarization with respect to the laser table. Pos. D. represents a two dimensional position detector (Newport Quadrant Cell); PZT mirror is a dual-piezo-driven mirror, capable of tipping both horizontal and vertical directions. Along the beam path, the first(second) Pos. D. feeds back to the first(second) PZT mirror with proportional-integrator loop. Thus the output beam pointing of the doubler is locked. The AOMs are not shown with actual orientation angle. The dashed beam line forms the BD far-detuned Doppler laser, and the solid beam line after the first AOM forms the BDD resonant/near detuned Doppler laser, with their frequency difference approximately 400 MHz. These two laser beams are combined at the BD det(detuned) SW(switch) AOM, where the BD beam is diffracted on the first order, which is overlapped with the undeflected BD beam. This configuration is due to the requirement of stronger far-detuned beam power than the near detuned one. Here some of the aligning mirrors are not shown. The double pass BD Switch setup uses a 15 cm lens placed at a focal length away from the center of the AOM. A corner cube retro-reflecting the beam with a vertical displacement, placed at the location that forms a one to one telescope with the lens. With this setup, the double pass alignment is insensitive to the change of AOM input frequency. The output of this setup is combined with the RD beams, then sent to the input of a UV fiber. The RF drive for BD switch AOM is actively noise-eat when the pulse is on. For this purpose, a pick-off mirror partially reflect the BD light to a detector, placed after the fiber, so that when the BD light is on, its power is actively stabilized. 33

3.5 Schematic for laser beam generation. “BBO doubling” denotes the doubling cavity setup [6] with BBO as the nonlinear conversion medium. For the seed lasers, we use NKT Koheras Adjustik lasers, and for the upper two amplifiers, we use NKT Koheras Boostik HPA. For the lower two amplifiers, we use IPG Photonic Ytterbium/Erbium Fiber Amplifiers. The respective frequencies of the Raman beams are controlled by the AOM frequencies. The Doppler beams are recombined before sending through a UV capable photonic crystal fiber [7]. To Doppler cool and image on both the experimental zone and the load zone, we further split the Doppler beam on the fiber output with a Glan-laser, with relative intensity controlled by a motorized $\lambda/2$ waveplate. 34

3.6 Schematic for RD laser beams setup. This setup is similar to the BD one, except that the generated beam frequency difference is approximately 1110 MHz, matching with the resonant frequency difference of the $|F = 1, m_F = 1\rangle$ and $|2, 1\rangle$ states. The $\frac{\lambda}{2}$ waveplates modifies the polarization of the laser beam, controlling the beam power splitted at the Glan-laser. The Glan-laser is setup so that the lower output beam is vertically polarized, and the upper output beam is horizontally polarized. The waveplate after the Glan-laser rotates the polarization back to vertical. 35

3.7 Schematic for Raman laser beams setup. This setup splits the Raman beam into the “CO” beam and the “90” beam, as indicated in Fig. 3.3. We adjust the frequency of the 90 AOM to drive transitions $|F = 1, m_F = 1\rangle \leftrightarrow |2, 2\rangle$ and $|1, 1\rangle \leftrightarrow |2, 0\rangle$. The CO beam line has an optional 600 MHz AOM double pass setup, to generate a pair of co-propagating CO beams to drive the carrier transition, which is not shown in the figure. For the double pass setup for Raman beams, the corner cube is replaced with three mirrors, to provide first order insensitive to AOM thermal refraction effect. This method is proposed by T. Rosenband, as shown in Fig. 3.8. 35

3.8 (a) Schematic for the "two mirror" double pass setup in a side-view. Here only the diffracted beams are shown as the AOM outputs but the actual the diffraction directions are perpendicular the page. The dashed orange line shows the deviation angle θ due to the AOM thermal thermal refraction effect. This effect can result from inhomogeneous distribution of RF power inside the AOM, or from inhomogeneous heat dissipation along the vertical directions in the figure. In this case, after double passing the AOM, the angular deviation is doubled. The lens is placed at a focal length f away from the AOM, and the round trip path length between the lens and mirrors is $2f$. (b) Schematic for the "three mirror" double pass setup. For three mirror setup, the deviated beam experiences a cancelling thermal refraction effect and the double pass output is overlapped with the beam where the thermal refraction effect is absent. 36

3.9 Schematic for the dipolar antennas in the experiment, not to scale. The microwave wavelength id denoted by λ. One arm of the antenna is soldered to the center conductor of the SMA, and the other end is soldered to the outer conductor. 37

3.10 Typical histograms collected from a given detection process. (a) Histograms from Ramsey experiments showing the count histograms for various states. From top to bottom, histograms of approximately two, one, and zero ions in the bright states are shown, corresponding to $\phi = \{0, \pi/2, \pi\}$ respectively. Gray vertical dashed lines separate the histogram into sections of count ranges that can distinguish the number of ions in the bright state. (b) Sections in (a) are summed up to form "rebinned" histogram. The new bins are labeled as 1-3. (c) From the rebinned histograms and the predicted populations from the Ramsey sequence, a population reference histograms representing 0-2 ions in the bright state are obtained with the maximum likelihood method. 41

4.1 (a) A simplified Λ configuration of Raman transition between internal states $|i\rangle$ and $|m\rangle$. (b) a Raman sideband transition of $|m,n\rangle \rightarrow |i,n-1\rangle$. 50

4.2 State evolution subject to the sideband Hamiltonian of Eq. 4.30, starting from state $|\downarrow\downarrow,0\rangle$. 54

4.3 Eigenvalues of the detuned sideband. 55

5.1 ^{24}Mg^{+} energy levels, laser setup and a spectrum showing the EIT effect. (a) Relevant energy levels for ^{24}Mg^{+}, in an applied magnetic field of 11.964 mT. The three levels $|g_1\rangle$, $|g_2\rangle$ and $|e\rangle$ serve as a Λ system for EIT cooling. Laser beams with σ^+ and π polarizations couple the ground states to the excited state with Rabi rates Ω_1 and Ω_2 and common detuning Δ. Wavy lines show spontaneous emission from the excited state to the ground states and the excited-level decay rate is denoted by $\gamma \simeq 2\pi\times41$ MHz. The fourth level $|e'\rangle$ can perturb the EIT cooling when the π polarized laser beam has frequency near the $|g_1\rangle$ to $|e'\rangle$ resonance. (b) Beam configuration and a depiction of the ^{9}Be$^+$–^{24}Mg$^+ -^{24}$ Mg$^+$–^{9}Be$^+$ ion, shown as balls from left to right. This figure is viewed in an angle from top view.(c) Simulation of the absorption spectrum of a stationary ion by a weak σ^+ probe beam for $\Delta = 2\pi\times96.7$ MHz, $\Omega_1/2\pi = 30$ MHz, and $\Omega_2/2\pi = 12$ MHz. For simplicity, the fourth level $|e'\rangle$ is ignored. The probe detuning from the $|g_2\rangle$ to $|e\rangle$ resonance is denoted by $\Delta_{\rm P}$. This Fano-like profile contains a narrow and broad feature corresponding to dressed states $|\psi_+\rangle$ and $|\psi_-\rangle$ respectively [8], and the separation between the peak on the right side and the null is labeled as δ. When $\Delta_{\rm P} = \Delta$, absorption vanishes due to coherent population trapping. 60

5.2 Mean motional excitation number $\bar{n}$ for the **I** (red triangles, $\omega/2\pi = 2.1$ MHz) and **O** (blue squares, $\omega/2\pi = 4.5$ MHz) axial modes of a ^{9}Be^{+}-^{24}Mg^{+} ion pair. (a) $\bar{n}$ after 800 μs of EIT cooling as a function of $\delta/2\pi$. Optimal cooling for each mode occurs when δ approximately equals the mode frequency. (b) $\bar{n}$ plotted as a function of EIT cooling duration t_c. From 0 to 74 μs, $\delta \simeq \omega_{\mathrm{O}}$, the out-of-phase mode frequency. From 75 to 85 μs, $\delta \simeq \omega_{\mathrm{I}}$, the in-phase mode frequency. In both figures, error bars represent statistical uncertainty of the sideband amplitude ratios. The solid lines are simulations of the full dynamics including the $|e'\rangle$ level in ^{24}Mg^{+}, measured ambient heating rates, detuning and beam intensities. In the simulations, we truncated the motion to the first 6 Fock states for both modes for the steady-state simulation in (a) and to the first 10 (6) Fock states for the **I** (**O**) mode for temporal simulation in (b). 65

5.3 Sympathetic EIT cooling on a ^{9}Be^{+}-^{24}Mg^{+}-^{24}Mg^{+}-^{9}Be^{+} ion chain. (a)Minimum $\bar{n}$ values for each of the four axial modes of a ^{9}Be^{+}-^{24}Mg^{+}-^{24}Mg^{+}-^{9}Be^{+} ion chain as a function of $\delta/2\pi$ after 800 μs of cooling to ensure steady state. Modes 1 to 4 are shown in the legend, and labeled as red triangles, green squares, black circles and blue diamonds, respectively. (b) $\bar{n}$ plotted as a function of EIT cooling duration t_c. From 0 to 40 μs, $\delta \simeq \omega_3$, the mode 3 frequency. From 40 to 45 μs, $\delta \simeq \omega_1$, the mode 1 frequency. In both figures, error bars represent statistical uncertainty of the sideband amplitude ratios. 66

5.4 (a) Minimum values of $\bar{n}$ for the two-ion **O** mode vs. $\Delta/2\pi$. The peak near 223 MHz results from resonant scattering on the $|g_1\rangle \leftrightarrow |e'\rangle$ transition from the π polarized light. Blue circles are the experimental data and red triangles are simulations based on [8]. Green diamonds are simulations not including $|e'\rangle$ and the black solid line shows $\bar{n} = (\gamma/4\Delta)^2$ [9]. (b) Simulation of 1/e cooling time vs. the mass of ion X^+ that is sympathetically cooled by $^{24}\mathrm{Mg}^+$ (axial modes), with fixed trap potential such that $\omega_{\mathrm{I(O)}}/2\pi = 2.1$ (4.5) MHz when X^+ is $^9\mathrm{Be}^+$. Red triangles are for the **I** mode; blue squares for the **O** mode. Optimum values of δ were chosen for each mode and ion-mass combination, with $\Omega_2/2\pi = 5.9$ MHz and $\Delta/2\pi = 96.7$ MHz. (Here $|e'\rangle$ is neglected) 67

6.1 Sideband interactions together with sympathetic cooling. The former is expressed by blue double arrows and the latter green wavy arrows. Other than the $|\uparrow\uparrow, n = 0\rangle$ state, all other spin states can be driven by the sideband interaction, which produces spin flips and motional excitation simultaneously. However, with sympathetic cooling, the evolution would lead to pumping to the dark state of the sideband, the $|\uparrow\uparrow, n = 0\rangle$ state. This state is dark since the sideband could not flip spin down and subtract motional quanta at the same time. 74

6.2 Energy Levels and Entanglement Preparation Scheme a) The internal energy levels (not to scale) of ^{9}Be$^+$ are shown as solid black lines for the ground motional state and dashed lines for the first excited motional state. The couplings needed to produce steady-state entanglement are shown with blue double arrows for the strong sideband coupling with Rabi rate Ω_s and sympathetic cooling; the patterned and dashed red arrows for the weak microwave coupling with Rabi rate Ω_c, repumper, and spontaneous emission from the $|e\rangle$ state. Wavy arrows depict the dissipative processes. b) Four spin states that span the $|\uparrow\rangle$, $|\downarrow\rangle$ qubit manifold of the two ^{9}Be$^+$ ions are shown as horizontal lines. Transfer processes that are accomplished by the sideband drive and sympathetic cooling are shown as blue arrows, while processes that occur by coupling the $|\uparrow\rangle$ state to the auxiliary $|\mathrm{a}\rangle$ state followed by excitation with the repumper and decay by spontaneous emission are shown as dashed red arrows. Processes shown as thin lines are shifted out of resonance due to the strong sideband coupling, leading to accumulation of population in the maximally entangled state $|\mathrm{S}\rangle$ in steady state. 77

6.3 Steady State Entanglement. The measured populations of the singlet, triplet, $|\uparrow\uparrow\rangle$ and $|\downarrow\downarrow\rangle$ states are shown as squares, crosses, circles, and triangles, respectively, as a function of the duration that all the elements of the dissipative entanglement scheme are applied simultaneously. The system reaches a steady state with a 0.75(3) population in the target singlet state after a few milliseconds. The solid lines are the result of a simulation based on the experimental parameters. The slow decrease in the singlet state fidelity at long times visible in the simulation is due to a leak of the qubits to spin states outside the $|\uparrow\rangle$, $|\downarrow\rangle$, $|\mathrm{a}\rangle$ manifold caused by spontaneous photon scattering from the Raman laser beams that generate the sideband coupling. Strictly speaking this depumping means that the state is only a quasi-steady state. For our parameters there is, however, a clear separation of the preparation and depumping time scales, justifying the description as steady state. Error bars represent standard deviations of each point. 80

6.4 Stepwise application of the dissipative entanglement scheme. a) We show the pulse sequence for one step. In this case, we set the repump and cooling to be full power, and we turn them on with enough duration so that they act as a complete pumping step. These pulses remain short compared with the coherent pulse, thus not introducing too much gap time in between the coherent evolution. b) We assume initial state to be the target $|S\rangle$ state, and we show a simulation with the sideband and microwave drives are applied simultaneously. In this case, with $\Omega_s/\Omega_c \approx 7$, similar to the parameter in the stepwise experiment. We can see the microwave flops part of the $|S\rangle$ state out to the auxiliary level but the population can be fully revived at certain durations, as shown by an arrow in the figure. We set the duration of the coherent pulse in a) to be at one of those durations, so we eliminate the leakage out from the $|S\rangle$ state. 82

6.5 Entanglement With Stepwise Scheme. The measured populations of the singlet, triplet, $|\uparrow\uparrow\rangle$ and $|\downarrow\downarrow\rangle$ states are shown as squares, crosses, circles, and triangles, respectively, as a function of the number of applied steps. Each step has a duration of approximately 220 μs. The solid lines are the result of a model as explained in the Methods section. Error bars represent standard deviations of each point. 84

7.1 Schematics for confined dynamics, for the cases of (a) two ions, and (b) three ions. The thin black double arrows depict the relatively weak microwave coupling, and the thick blue double arrow depicts the strong laser sideband coupling. With $|\uparrow ... \uparrow\rangle$ states initially populated (red dots), the microwaves drive the state down the symmetric manifold, the states on the left, where $|\overline{W}\rangle = \frac{|\uparrow\downarrow\downarrow\rangle+|\downarrow\uparrow\downarrow\rangle+|\downarrow\downarrow\uparrow\rangle}{\sqrt{3}}$ in (b). However, the sideband excitations perturb the lower states, coupling them to other states, denoted by $|S\rangle$ and $|W_\mathrm{c}\rangle = \frac{e^{i2\pi/3}|\uparrow\uparrow\downarrow\rangle+|\uparrow\downarrow\uparrow\rangle+e^{-i2\pi/3}|\downarrow\uparrow\uparrow\rangle}{\sqrt{3}}$. Thus the microwave induced dynamics are confined between the two highest energy states on the symmetric manifold. For (b) we only show the states that are relevant to the dynamics. 91

7.2 Two ion population evolution for confined dynamics with microwave and sideband excitations applied simultaneously. Population mainly evolves between the $|\uparrow\uparrow\rangle$ and the $|T\rangle$ state, while other states have very small populations. The pink diamonds, blue triangles, red squares and green circles represent the measured populations of states with all spins down, one spin up, two spins up and the $|T\rangle$ state, respectively. The difference between P_1 and $P_{|T\rangle}$ is due to the populations in the $|S\rangle$ state. The solid lines shows the results of the numerical simulation taking into account known experimental imperfections, with the same coloring convention as for the measured populations. The black dashed line shows unit population. The error bars for $P_{|T\rangle}$ state are indicated by the size of the symbols. All error bars are from data resampling of a maximum likelihood analysis. 94

7.3 State evolution for confined dynamics of two trapped ions using a composite pulse sequence. Similar to Fig. 7.2, populations are mainly confined to the $|\uparrow\uparrow\rangle$ and $|T\rangle$ states. The coloring and labeling conventions are the same as Fig. 7.2. The laser phase and detuning are flipped 25.4 μs after the start of the experiment. Note that the oscillations of $|\downarrow\downarrow\rangle$ are enhanced at $t > 25.4$ μs; however the maximal population of $|T\rangle$ state is increased compared to the single pulse used for the data in Fig. 7.2. All error bars are from data resampling of a maximum likelihood analysis. 96

Chapter 1

Introduction

In this thesis we will describe the primary research accomplishments with trapped ions (1) demonstrating sympathetic electromagnetic-induced-transparency (EIT) laser cooling on a mixed ion chain, (2) generating steady state quantum entanglement with dissipation and (3) generating quantum entanglement with novel engineered quantum dynamics. These works have different contexts and backgrounds, so it is hard to pick one of them to emphasize a motivation for the entire thesis. Instead, we will briefly describe the overall background of quantum information processing and its implementations on trapped ion experiments, and highlight the role of the three topics above.

1.1 General description of quantum information and entanglement

Information technology is undoubtedly one of the most important breakthroughs in the 20th century. Its development has been following the Moore's law [10] for decades, where the number of transistors in an integrated chip would double every eighteen months. This marked growth of the level of integration that has led to an increase in the computational and storage capabilities. When the size of the electronic devices on the chip approaches the size of the atoms, on the order of half a nanometer, the quantum theory predicts a limit to the Moore's law [11]. One possible solution to this problem is to try to process information taking advantage of the quantum effects. It turns out with those effects, computation can be substantially faster for solving particular mathematical problems on a large scale, for example [11–13], known as quantum computing. Also for simulation of quantum systems, use of quantum resources can significantly outperform those with classical resources [14]. For these reasons, research on quantum computing and quantum simulation have been hot topics for both theoretical [15] and experimental researchers [16–18].

The advantages of using quantum effects derive from superposition. Classically, high or low electric potentials/currents of electric components are labeled as bit 0 and 1. However, the quantum bits (qubits) are quantum states, labeled with $|0\rangle$ and $|1\rangle$. In analog to the spin-1/2 system, we also label $\{|0\rangle, |1\rangle\}$ as $\{|\uparrow\rangle, |\downarrow\rangle\}$ The qubits can be realized with various objects, for example electronic states in neutral atoms, atoms in a cavity [19], Rydberg atoms [20], laser trapped atoms [21], trapped ions [22], linear optics [23], photons coupled to ions [24] and the collective charge or flux in a superconducting circuit [25]. The criteria for the choice of qubit is that they have well-defined quantum mechanical states, which can be detected and distinguished, and with proper coherence time be "alive" quantum mechanically, as described below. The use of quantum states to store information enables quantum superposition, especially quantum entanglement, a unique property of quantum mechanics giving the advantages. A quantum state $|\psi\rangle$, if we assume it is defined within one-qubit states, can be generally be expressed by

$$|\psi\rangle = \alpha|0\rangle + \beta|1\rangle, \tag{1.1}$$

where α and β are complex numbers, representing the amplitude of $|\psi\rangle$ being in each of the states; $|\alpha|^2$ and $|\beta|^2$ represent the probabilities of being in each of the states, with their sum to be unity by definition. We can remove the common phase between them since this phase is usually non-detectable. However, in general, $|\psi\rangle$ represents a quantum state that is *simultaneously* in $|0\rangle$ and $|1\rangle$, and the complex phase difference between α and β is also well-defined, giving the so-called quantum coherence, so we need 2 real numbers to fully characterize this state. It is convenient to express the qubits in the vector form, so that $|0\rangle = \begin{pmatrix} 1 \\ 0 \end{pmatrix}$ and $|1\rangle = \begin{pmatrix} 0 \\ 1 \end{pmatrix}$. We also denote the complex conjugate of $|\Psi\rangle$ as $\langle\Psi| = |\Psi\rangle^\dagger$. Thus the one qubit rotation operation can be in general expressed as $R\{\theta, \phi\}$, defined in matrix form as $R\{\theta, \phi\} = \begin{pmatrix} \cos(\frac{\theta}{2}) & -ie^{-i\phi}\sin(\frac{\theta}{2}) \\ -ie^{i\phi}\sin(\frac{\theta}{2}) & \cos(\frac{\theta}{2}) \end{pmatrix}$. Interestingly for N qubits, the superposition would involve in general 2^N states, and one needs $2^{N+1}-2$ real numbers to fully expand the state $|\psi_N\rangle$ in the $|0\rangle, |1\rangle$ manifolds for each qubit,

$$|\psi_N\rangle = \alpha_1|00...00\rangle + \alpha_2|00...01\rangle + \alpha_3|00...10\rangle + ... + \alpha_{2^N}|11...11\rangle, \tag{1.2}$$

where $\sum_{i=1}^{2^N}|\alpha_i|^2 = 1$. An example is that for 300 qubits, it would involve more than 10^{90} states. This exponential scaling can in principle give a large win in computation. A simple comparison [11, 26] is given by considering a classical machine that takes input x and gives output $f(x)$ with a certain function f. For N bits the input state can be any one of the classical inputs from $00...00, 00...01, 00...10, ..., 11...11$, but this computation can only happen once at a time, suppose we have only one machine. For the quantum case, we define the operation to be input state $|x\rangle|0\rangle$ and outputs state $|x\rangle|f(x)\rangle$. One can input an equal superposition of all the states

$$|\psi_{\text{in}}\rangle = \frac{1}{\sqrt{2^N}}(|00...00\rangle + |00...01\rangle + |00...10\rangle + ... + |11...11\rangle)|0\rangle, \tag{1.3}$$

which can be expressed as $|\psi_{\text{in}}\rangle = \sum_x \frac{1}{\sqrt{2^N}}|x\rangle|0\rangle$, where x is the binary number range from 00...00 to 11...11. The output would be $|\psi_{\text{out}}\rangle = \sum_x \frac{1}{\sqrt{2^N}}|x\rangle|f(x)\rangle$, as if all the computations happen simultaneously, giving the advantage known as so-called quantum parallelism[1] Interestingly, $|\psi_{\text{out}}\rangle$ can not be expressed as a product state of different qubits in general. An example for two qubits is what we call the triplet state in this thesis,

$$|T\rangle = \frac{1}{\sqrt{2}}(|01\rangle + |10\rangle). \tag{1.4}$$

The qubit states are highly correlated, and an attempt to express the states of each qubit separately, i.e., writing $|T\rangle = |\psi_1\rangle|\psi_2\rangle$, is impossible mathematically. This interesting phenomenon is called quantum entanglement, a unique feature of quantum mechanics compared with the classical counterparts. Entanglement is known to be the key property of quantum information processing [11], such as quantum computing, quantum key distribution for secure communication, and quantum simulation.

---

[1] The information of $f(x)$ can be further extracted by performing quantum Fourier transformation, to create interference between states associated with $|x\rangle$ [27].

Entanglement also has many other applications, including but not limited to the following. It can help to show the non-local fundamental feature of quantum mechanics, such as through Bell's inequality [28–31]. For spectroscopy, quantum entanglement could help suppressing the uncertainty of measurement [32, 33], and improve the readouts of the atomic clocks [34–36]. Due to its importance, generating quantum entanglement is one of the main topics in this thesis, and we will describe both the traditional and novel methods developed during my thesis work. In the following section we will describe scalable quantum computation and motivate the need of the cooling technique we develop.

In practice, due to dissipative processes in the experiments, a quantum state needs to be expressed as a density matrice ρ, in general represents a statistical mixture of different states $|\Psi_i\rangle$ with probability P_i, with $\rho \equiv P_i|\Psi_i\rangle\langle\Psi_i|$. For a pure state $|\Psi\rangle$ similar to the states above, the corresponding density matrix is $|\Psi\rangle\langle\Psi|$. Thus given an experiment result ρ, the probability of obtaining state $|\Psi\rangle$ can be expressed as the fidelity, in this thesis we use the definition $\langle\Psi|\rho|\Psi\rangle$.

1.2 Scalable quantum computing architecture and sympathetic cooling

There are many different ways to implement quantum computing. One way is to trap linear chains of ions as elementary modular unit, and different modules are coupled by photons emitted by the communication ion in the chains [37]. Another promising architecture is the scalable CCD architecture for trapped ions [2, 22], as depicted by Fig. 1.1. In this scheme, ions are trapped in different trap zones, and by controlling the electric potentials, ions can be separated, recombined and shuttled between different zones. Ions can be individually addressed to perform single qubit operations, for example the spin rotations and detections. And ions can also be entangled by pairs in certain zones and then separated and reshuffled to entangle with other ions in the architecture. In practice, the individual addressing can be realized by laser beams focused to single trap zone or by microwave fields with ions moved to different locations in a field gradient [38]. To generate entanglement, one way is to put pairs of ions together in the same trap zone and employ the shared motional modes in the ion crystal [39]. An alternative way is to trap them in two close but distinguishable zones [40, 41].

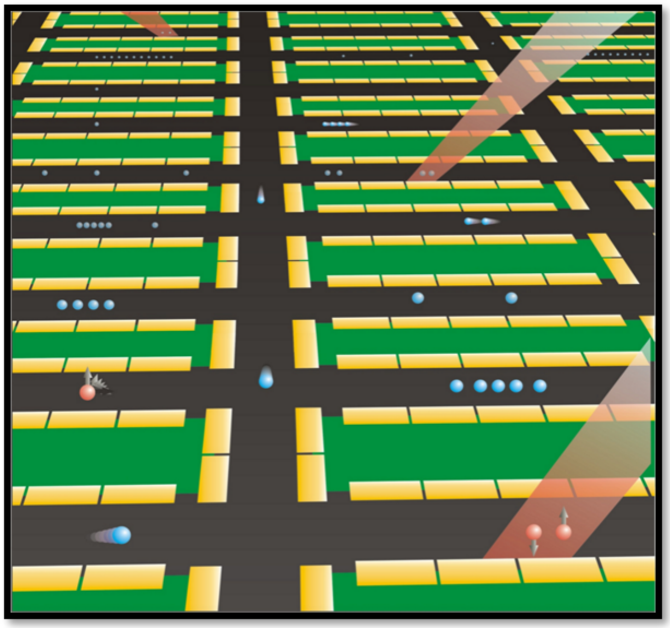

Figure 1.1: A scalable quantum information processing device with trapped ions [2]. The structure consists of linear trapping sections, and junctions. Ions are trapped in long chains, separated, shuttled and recombined. Lasers beams are shown to entangle ion pairs.

In the trap-array method, ions are frequently separated, shuttled and recombined. Traditionally, these operations impart significant motional excitation to the ions [42], which affects subsequent entangling operations [43]. Direct cooling of the logic ions involves driving transitions of the internal states accompanied by spontaneous emissions, which destroys the quantum states that store information. For this reason, a technique called sympathetic cooling can be used [44], where we co-trap a different species of "coolant" ion with the logical ion in the same trap, utilizing the shared motional modes. We then apply cooling laser beams to the coolant ion to cool the entire crystal to the motional ground state. Since the cooling laser beams are far off-resonant and essentially decoupled from any transition of the logic ion, the stored information is preserved.

Traditionally, Doppler cooling and Raman sideband cooling are applied, but the typical duration is on the order of hundreds of microseconds [42]. Even with the latest improvements of diabatic and cold ion separation and shuttling [45], several rounds of Raman sideband cooling are needed. One drawback is that to drive high fidelity Raman transitions, high Raman laser power is needed for sufficient detuning [46]. To address these problems, we examine a technique called sympathetic electromagnetically-induced-transparency (EIT) cooling. This technique uses relatively low power and a near-detuned pair of laser beams to create dressed states that can provide fast cooling and simultaneously cool a broad frequency range of motional modes. We apply this technique to chains of $^9\mathrm{Be}^+ -^{24}\mathrm{Mg}^+$ and $^9\mathrm{Be}^+ -^{24}\mathrm{Mg}^+ -^{24}\mathrm{Mg}^+ -^{9}\mathrm{Be}^+$ ions, where $^{24}\mathrm{Mg}^+$ serves as coolant ions and we demonstrate near gound state cooling of all the axial modes with an order of magnitude improvement on cooling speed while decreasing the applied laser power by two orders of magnitude compared to experiments that use traditional sideband cooling.

1.3 General description of entanglement operation and novel methods

To generate entangled states, it is conceptually convenient to introduce the controlled-not(C-NOT) operation. Here, if the state on the control qubit is at the $|0\rangle$ state, no operation would be applied to the target qubit; if the control qubit is at the $|1\rangle$ state, then the target qubit would get a spin flip, an operation known as a NOT logic gate. A special case is that if the control qubit is initialized to an equal superposition of $|0\rangle$ and $|1\rangle$, and the target qubit is initialized to spin down, after this operation a triplet state is created as in Eq. 1.4.

Entangling operations require a mutual coupling between the two qubits. To entangle trapped ions, a common way is to trap ions in the same electric potential, and due to the Coulomb interaction, ion motion consists of normal modes. For example, for the case of two equal mass ions, the motional modes are the common mode, where the ions oscillate with the same phase; and the stretch mode, where they oscillate out of phase. As detailed in Chapter 4, one can apply a motional sideband transition, where a pair of non co-propagating laser is tuned to have frequency difference equal to the qubit transition plus/minus a motional mode frequency. Starting from the ground qubit state, this pair of laser beams would flip the qubit state while at the same time excite/de-excite one quanta of the relevant motional mode. One simple way to generate spin-spin coupling is to apply the pair of laser beams focused on the two ions separately; in this case the spin-dependent motional excitation on one ion can be used as a trigger for spin flip for the other one [15, 47]. Other techniques have also been explored [48–53]. These also involve laser sideband couplings for qubit spin flip of qubit phase accumulation.

In this thesis, we introduce two novel methods to generate entanglement. The first method is to have the sideband transition as a perturbation and thus constrain the quantum dynamics, known as the Quantum Zeno dynamics [54–56]. Here the qubit rotations can be implemented with microwaves, which can have very high fidelities [57–59]. We can then drive a transition from an unentangled initial state to an entangled state within the constrained manifold. Since the transition is not directly driven by the laser, the requirement of precise control of the timing of the laser pulse, laser intensity, laser detuning and motional mode frequency stability are not stringent, compared to the quantum logic operations mentioned above. We demonstrate this scheme with two ions and obtain a high fidelity triplet state creation. This scheme can be generalized to three ions in a straightforward manner, and we demonstrate generation of the W-state, an equal superposition of two spin up and one spin down states.

The second method is more complicated, where we generate a state that does not couple to the sideband interaction. Furthermore, this method reaches a steady state using dissipative techniques, where we induce cooling, optical pumping, microwave transitions, and laser sideband interaction all together, and the system is pumped to an entangled state which does not couple to any of the interactions above. Here the target state is a "dark" state, while the other states of the system are pumped to and trapped in the dark state. In previous experiments, entanglement has been generated by applying dissipation to atomic ensembles coupled by electromagnetic modes to generate [60], and by applying quantum logic gates and dissipation processes to trapped ions [61]. Our experiment is the first demonstration of steady state production using dissipation for trapped ions without using quantum logic gates, and can be further deployed as a stabilization technique, where if the target state suffers an error, the continuous application of the interactions can actively pump the state back to the target state [62].

1.4 Thesis organization

In Chapter 2 we describe the general features of our apparatus, giving some technical details, including the structure of the ion trap, vacuum system, laser beam lines, microwave setup, imaging/detection setup and control systems. In Chapter 3 we describe the energy structure of the $^9\mathrm{Be}^+$ ion, the qubit ion in our experiments. We further describe the operations on the qubit, including initializing and manipulating the qubit spin and motional states, with laser beams and microwave fields, and detection of spin and motional state. In Chapter 4 we describe the spin-motional coupling induced by laser beams. In Chapter 5 we describe the EIT cooling method mentioned above. We start with the general EIT theory, and we describe the experimental setup and the experiment process. We further describe the technical details of our experiment and possibility of applying the technique to other species of coolant ions. In Chapter 6, we describe the steady state entanglement generation and stabilization using the dissipative method. In Chapter 7, we describe the theory and experiment of the Zeno dynamics. We further present a composite pulse sequence technique to our scheme for better performance, and also we present the application to three ions. For Chapters 6 and 7, we will describe our understanding of the error sources, the construction of numerical simulations, and we compare the experimental results with the simulations. Finally, we will conclude this thesis with remarks on future applications of techniques in this thesis.

If you find this thesis interesting or have questions or remarks, please send me an email at yiheng.lin@colorado.edu or yihenglin.ustc@gmail.com.

Chapter 2

Ion trapping

In this chapter we will describe various apparatus for the trapped ion experiments in this thesis. The beauty/complexity of a trapped ion experiment is that it involves many different technologies. In Fig. 2.1, a basic structure of the trapped ion setup is shown with some examples of specific equipment. In this chapter we will briefly describe the various tasks and requirements in Fig. 2.1 are satisfied. In the first and second sections we describe the general theory of ion trapping and the trap configurations we are using, respectively. In the third section we describe a few other components for the trapped ion experiment: the magnetic field coils, the vacuum system, imaging system, and the experimental control system.

2.1 Idealised ion trapping theory

An idealised ion trap with a "four-rod" configuration is depicted in Fig. 2.2; to begin with we describe the theory for trapping a single ion [22, 63]. An RF voltage with optional offset $V(t) = V_0 \cos(\Omega_\mathrm{T} t) + U_r$ is applied to the RF electrodes. We ignore the phase of the RF because it does not affect the trapping in this configuration. Near the center of the radial plane, the potential expanded to second order has the form

$$\Phi \approx \frac{(V_0 \cos(\Omega_\mathrm{T} t) + U_\mathrm{r})}{2}(1 + \frac{x^2 - y^2}{R^2}), \tag{2.1}$$

where R is approximately the distance from the center to the nearest surface of the electrodes. DC voltages U_0 are applied to the high voltage DC electrodes and 0V applied to the low voltage

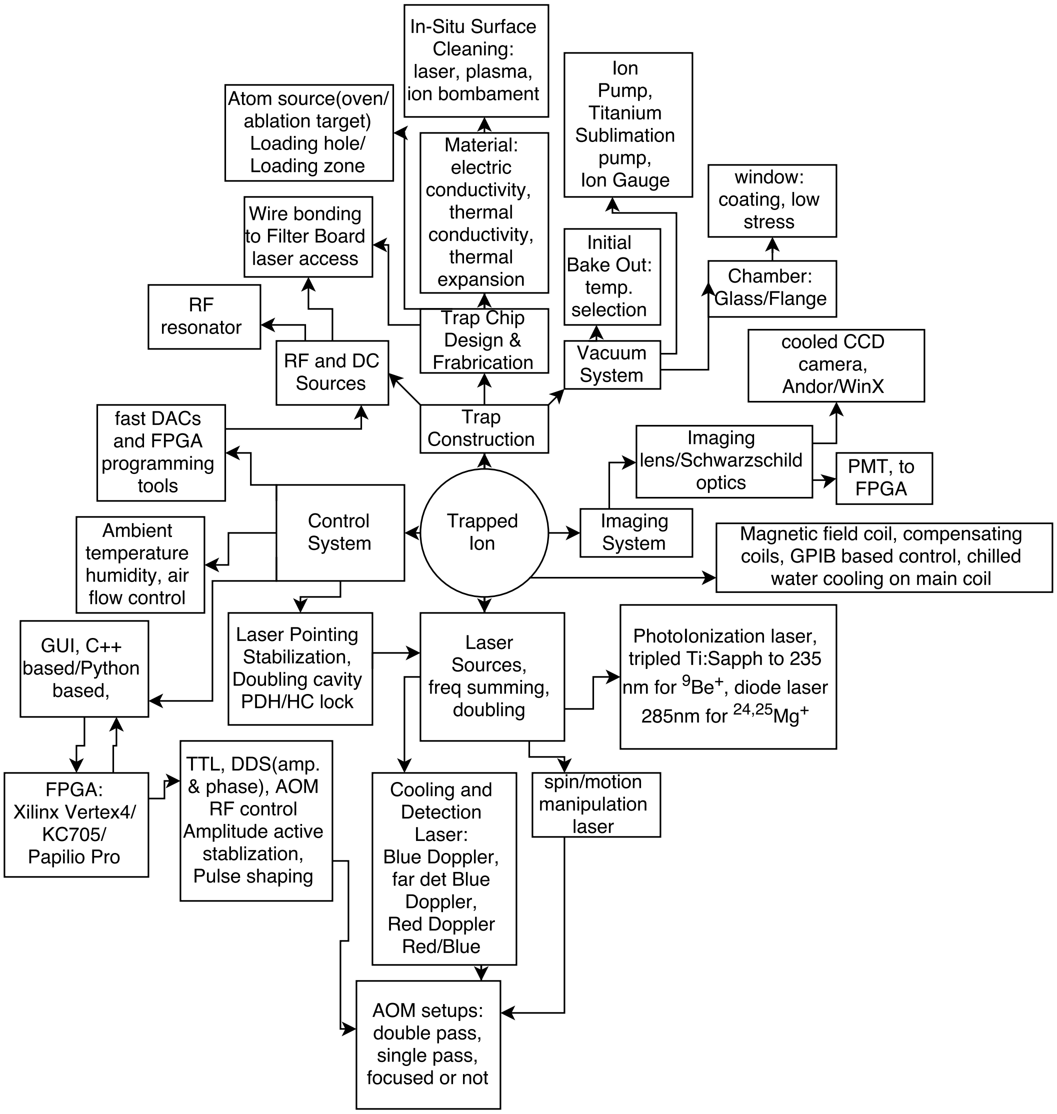

Figure 2.1: Schematic for trapped ion experiment, showing the major components and some more details and requirements of technology therein.

electrodes. Note that the potential satisfies Laplace's equation $\nabla^2\Phi = 0$. Along the trap axis near the center, to the second order a static potential is created of the form

$$\Phi_s \approx \kappa U_0 (z^2 - \frac{x^2+y^2}{2}) = \frac{m}{2q}\omega_z^2 (z^2 - \frac{x^2+y^2}{2}), \tag{2.2}$$

where m and q are the mass and charge of the ion, $\omega_z = \sqrt{2\kappa q U_0/m}$ is the oscillation frequency along the axial direction and κ is the geometrical factor determined by the actual trap geometry, which can be numerically calculated with a finite element method. We call ω_z the center-of-mass(COM) motional frequency. This frequency is independent of the number of a collection of ions with identical mass and charge, as long as the expansion of Eq. 2.2 is valid.

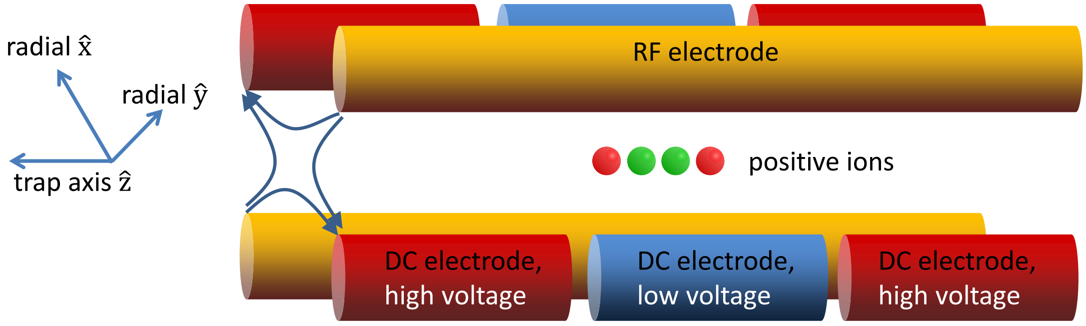

Figure 2.2: An idealised ion trap with "four-rod" configuration. The gold rods are the RF electrodes, and the segmented ones are DC electrodes. The two RF electrodes are typically shorted together, and provide a quadruple confinement potential in the radial plane. To form confinement of positively charged ions along the axial direction, we apply positive potentials on the outer electrodes and lower potentials on the center electrodes. The axial confinement is designed to be weaker than the radial confinement, so that the ions are trapped along as a linear chain along ẑ.

We first describe the radial direction of motion. With Eq. 2.1, Eq. 2.2 and Newton's second law, equations of motion can be expressed in the form of the Mathieu equations

$$\frac{d^2x}{d^2\xi^2} + (a_x + 2q_x \cos(2\xi))x = 0, \tag{2.3}$$

$$\frac{d^2y}{d^2\xi^2} + (a_y + 2q_y \cos(2\xi))y = 0, \tag{2.4}$$

where $\xi = \Omega_{\mathrm{T}} t/2$, $a_x = (\frac{4q}{m\Omega_{\mathrm{T}}^2}(\frac{U_r}{R^2} - \kappa U_0))$, $a_y = (-\frac{4q}{m\Omega_{\mathrm{T}}^2}(\frac{U_r}{R^2} + \kappa U_0))$, and $q_x = -q_y = \frac{2qV_0}{m\Omega_{\mathrm{T}}}$. Here we ignore the radial potential from the DC electrodes. Note that U_r breaks the degeneracy of the two equations. And the existence of the DC voltages can also break the degeneracy. To solve for Eq. 2.3, the Floquet theorem can be applied due to the periodic nature of the equations. With a proper choice of parameters the solution represents a non diverging trajectory, or the stable trapping region [64, 65]. Typically with $a_i < q_i^2 \ll 1, i \in \{x, y\}$, a stable solution can be achieved and can be described by an infinite series of harmonic oscillators with decreasing amplitudes for higher orders. The two lowest orders are given by

$$u_i(t) \approx A_i(\cos(\omega_i t + \phi_i)(1 + \frac{q_i}{2}\cos(\Omega_\mathrm{T} t) + \frac{q_i^2}{32}\cos(2\Omega_\mathrm{T} t)) + \beta_i \frac{q_i}{2}\sin(\omega_i t + \phi_i)\sin(\Omega_\mathrm{T} t)), \tag{2.5}$$

where $u_i = \{x, y\}$, A_i and ϕ_i depend on the initial conditions, and

$$\omega_i = \beta_i \frac{\Omega_\mathrm{T}}{2},\ \beta_i \approx (a_i + q_i^2/2)^{1/2}. \tag{2.6}$$

The ω_i is known as the secular motion frequency of the radial direction, and the motion for low energy, corresponds to that of a harmonic oscillator. From Eq. 2.5 and $a_i < q_i^2 \ll 1, i \in \{x, y\}$, the motion is modulated by a fast oscillation with frequency Ω_T, called the micromotion. However with experimental imperfections such as stray charges, unbalanced DC electric voltages, the ion can be displaced from the trap axis so the micromotion is not negligible. This can be compensated by applying extra potentials on the DC electrodes, known as “shims”, as described in [5].

For linear traps, typically the radial confinement is made to be much stronger than the axial confinement. If multiple ions are trapped in the same potential, the ions form a linear chain along the axial direction. For two identical ions, the motion of the ions are coupled due to the strong Coulomb repulsion. To solve for the equation of motion, typically one would start from solving the equilibrium location of the ions, then perform an expansion to solve for the secular motions. For identical ions, introducing the length scale $s = q^{2/3}/(4\pi\epsilon_0 m\omega_z^2)^{1/3}$ would be convenient. For $^9\mathrm{Be}^+$ ion, with $\omega_z = 2\pi \times 3.58$ MHz, $s \approx 3.12\mu m$. For two ions, the separation of the two ions is $s_2 = 2^{1/3}s$; and for three ions the neighboring separation is $s_3 = (5/4)^{1/3}s$. For the motional modes, the center of mass mode is not changed for small chain of ions, but more motional modes would appear for multiple ions. More detailed analysis will be provide in Chapter 4.

2.2 Trap configurations

In recent years significant attention has been given to planar trap configurations [66], where the four rods and other electrodes are flattened and can be fabricated onto a planar surface. This enables the use of on-chip microwave lines for single- and multiple-ion logic gates, and in the future can enable the use of on-chip detectors and laser waveguides [67, 68]. Here we focus on describing the three dimensional traps used in the experiments in this thesis. We will first describe the basic components including the trap wafer and trap RF, which form the trap. Then we will describe two types of traps, the linear and the junction traps, which we use in the experiments.

2.2.1 Trap wafers

In the experiments described in this thesis, a three dimensional trap configuration is used, similar to the four-rod configuration above. The rods have evolved to various geometries in the experiments, such as four blades [69]; in our lab it was implemented as a wafer structure. The wafer is constructed from laser machined polished alumina substrates. A through slot is laser machined on each wafer to provide optical access with ions accessible through the middle of the slots. The electrodes are formed by either patterned sputter-coated gold or electroplated gold deposition [3, 70, 71] surrounding the slot. The separate wafers were stacked together by hand with annealed stainless steel screws, with alumina spacers in between and gauge-pin holes for alignment. In addition to the electrodes that form the "four rod" configuration, an extra wafer is needed to provide a biased electric field, named as the "bias board". The bias board is needed to provide DC potentials along the direction of RF electrodes (radial y-direction in Fig. 2.2), since the two RF electrodes are shorted together. All the electrodes on the wafer are extended to the edge of the wafer, with larger widths near the edge of wafer for wire bonding or ribbon bonding to the back plane.

The back plane is also called the filter board, providing low-pass filtering for the DC electrodes to block frequencies near the trap frequencies, on the order of a few MHz and higher. The filter board has electrodes that at one end match with the size of the electrode on the wafer for wire/ribbon bonding and the other side has larger size for soldering to leads that connect to voltage sources. For on board filtering, these electrodes also have gaps for on-chip resistors; one end of the capacitors are soldered onto the electrode after the resistor and the other end connected to the ground pad on the board. The electrodes are then further connected via feed throughs to connections outside of the vacuum. The resistor is typically $\sim 250\ \Omega$ and capacitor ~800 pF, to have a corner frequency below 1 MHz.

To realise the basic components of scalable quantum information processing [2], multiple segmented electrodes are fabricated on the trap, enabling multiple trap zones and control of ion transport, including ion shuttling, combining ions from separated zones into the same zone and the reversed processes(ion separating). Typically, a range of DC electrode voltages of -10 to 10 V is enough to perform ion transport, as well as forming axial trapping potentials of ~4 MHz for one $^9\mathrm{Be}^+$ ion, and performing micromotion nulling.

2.2.2 Trap RF

In our experiment, the RF source[1] ranges from -1 dBm to -4 dBm, which is further amplified[2] to ~2 Watts of power. As we describe above, we need a high voltage amplitude on the RF electrode for stable trapping. Typically we capacitively couple the output of the amplifier to an RF $\lambda/4$ coaxial resonator [72]. One end of the center rod is connected to the grounded outer cylinder, and the other end is connected to the trap RF electrode and is open circuited. The length of the outer cylinder is longer than the inner rod, so it also functions as a shielding cover for the trap chip, with holes to allow optical access. Also it functions as a support structure to hold the trap chip and oven in place. With Q~100 we can achieve a voltage on the electrode to be ~200 V.

2.2.3 The linear trap and the junction trap

The first ion trap in my experiments is configured to trap ions in multiple multiple zones of a linear trap, designed by Murray Barrett and built by John Jost [3]. The trap chip, filter board and segmented electrode scales are depicted by Fig. 2.3. With this trap a number of experiments were performed to demonstrate techniques for quantum information processing, including demonstration of a magnetic field insensitive qubit for $^9\mathrm{Be}^+$ [73], entangled ion motion in separate trap zones [74],

---

[1] Agilent Oscillator, Rohde & Schwarz signal generator SMT 02

[2] Amplifier Research, 36 dB Gain

and a two qubit quantum processor with quantum logic gates and ion transport [42, 45, 75–77]. For this thesis, we demonstrate EIT cooling [78] and dissipative entanglement [79] with this trap. Up to nine $^9\mathrm{Be}^+$ ions in a linear chain have been trapped and tested for separation waveforms [45]. In our experiments we trap with $^9\mathrm{Be}^+$ - $^{24}\mathrm{Mg}^+$ ion pair and $^9\mathrm{Be}^+$ - $^{24}\mathrm{Mg}^+$ - $^{24}\mathrm{Mg}^+$ - $^9\mathrm{Be}^+$ ion chains.

When we moved the apparatus to another building at NIST, we set up the experiment based on a trap designed and built by R. Bradford Blakestad [4], shown in Fig. 2.4. The unique feature of this trap is the “x” shape junction that provides capability of re-ordering the ions in a chain by shuttling the ions through the junction. Such junctions are important building blocks of a scalable architecture of trapped ion quantum computing [2], depicted by Fig. 1.1. In this architecture, single qubit rotations, two/multiple qubit operations, and spin detections are dedicated to different trap zones, and junctions are needed to extend this architecture to two dimensional. The junction enables coupling between arbitrary pairs of ions, in contrast to linear trap which can only easily couple neighboring pairs of ions. In the experiment described in this thesis, we trap ions only at the load zone and the experiment zone.

2.3 Other components for ion trapping

Many other components are required for an ion trap experiment. Here we describe a few of these. For loading ions in the trap, we describe the atom source and lasers used for photoionization. We then briefly describe the vacuum system, imaging system, and the coils for the external magnetic field. Finally we describe the laser and microwave sources for atomic state manipulation, and the experiment controls.

2.3.1 Ion loading: atom source and photoionization

In our traps, a trapping zone is dedicated to loading ions. The loading process involves emitting atoms form a thermal source (the oven), and atoms are subsequently ionized by electron beam collision or by photoionization (PI). These processes can contaminate the nearby trap surface

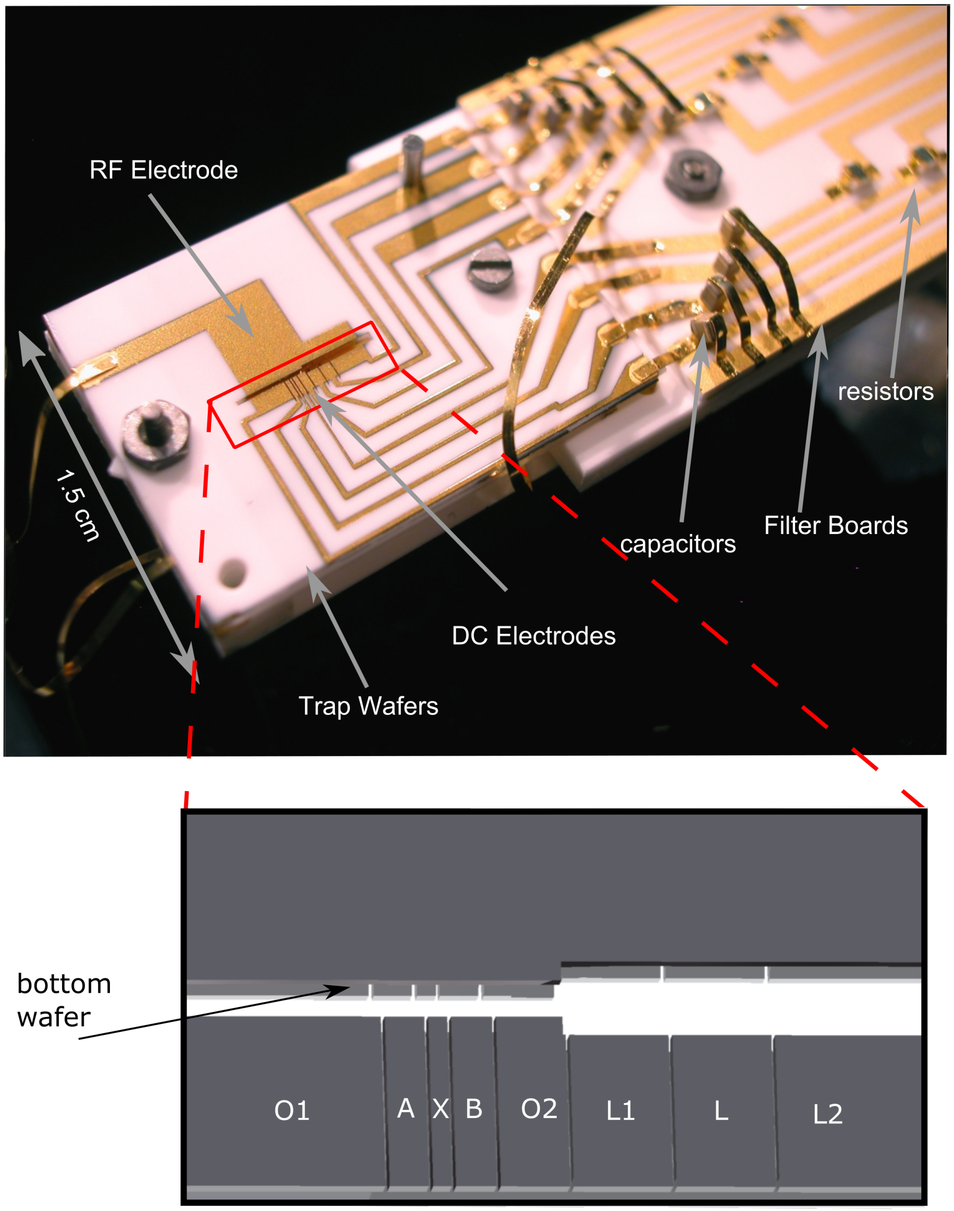

Figure 2.3: View of the linear trap [3]. Only the top wafer is visible. The RF electrode and the segmented DC electrodes are shown, and the DC electrodes are gold ribbon bonded to the filter boards. The bottom figure represents a closed view of the segmented electrodes. The widths of the electrodes from left (O1) to right (L2) are {2,0.2,0.1,0.2,0.36,0.5,0.5,2}mm [3]. The small gaps between the electrodes are 0.02 mm. The electrodes O1-O2 form the experiment region; the electrodes L1-L2 form the loading region. The gap between the DC and RF electrodes in the experiment/loading region is 0.2/0.4 mm wide.

and increase the motional heating rate. Such a problem can be mitigated by dedicating a load zone

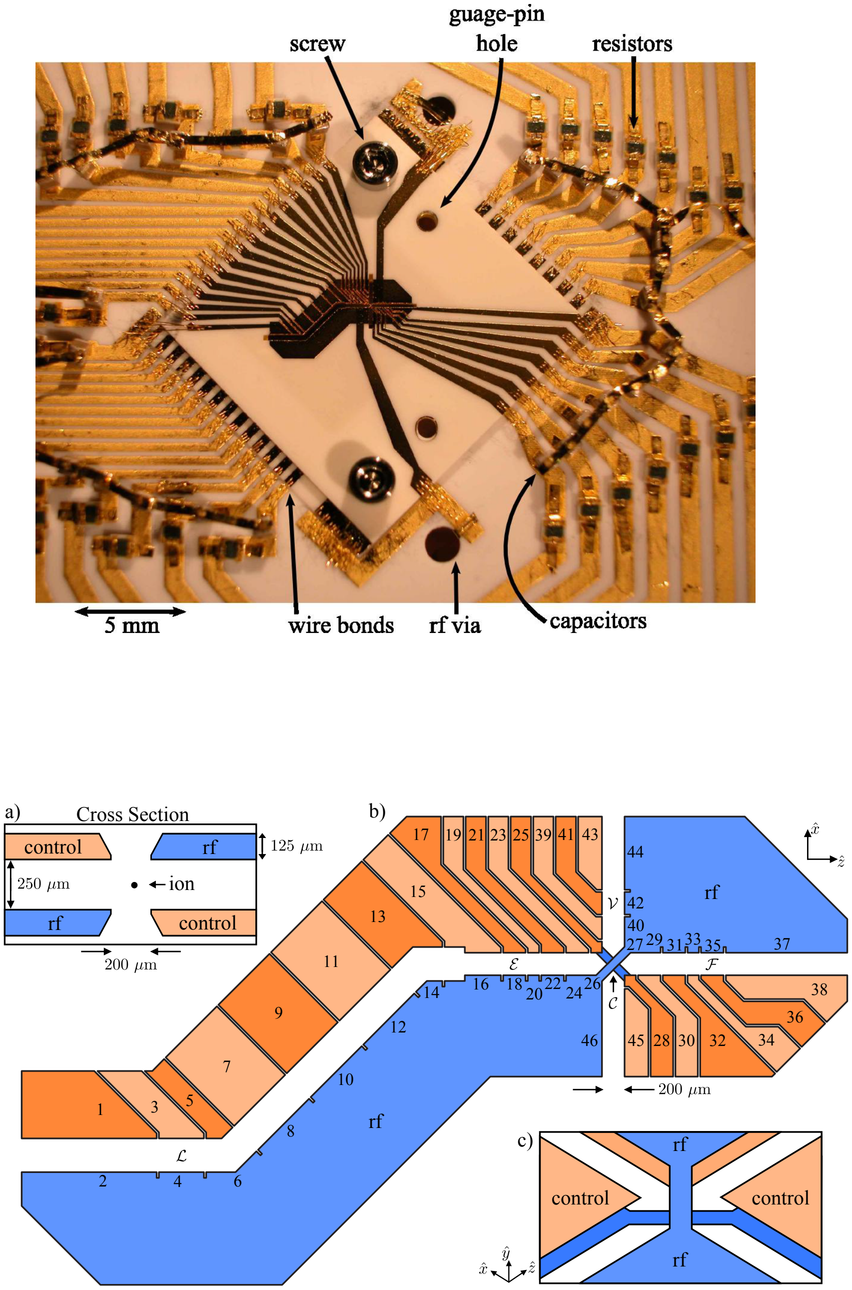

Figure 2.4: Close view of the junction trap. Only the top wafer is visible. The RF electrode and the segmented DC electrodes are shown, and the DC electrodes are gold-wire-bonded to the filter boards. The bottom figure represents the scale of the segmented electrodes. $\mathcal{L}$, $\mathcal{E}$, $\mathcal{V}$, $\mathcal{F}$, and $\mathcal{C}$ represents the loading zone, the experiment zone, the vertical zone, the "far" zone, and the center of the junction, respectively. The width of the electrode at $\mathcal{E}$ is 200 μm. The narrower electrode next to it is 100 μm wide, specifically for ion separation. The gaps between the electrodes are 20 μm wide. Ions chains can be separated and shuttled back and forth through two different routes, either $\mathcal{E} \rightarrow \mathcal{C} \rightarrow \mathcal{V} \rightarrow \mathcal{C} \rightarrow \mathcal{E}$ or $\mathcal{E} \rightarrow \mathcal{C} \rightarrow \mathcal{F} \rightarrow \mathcal{C} \rightarrow \mathcal{E}$, and thus enabling ion chain reordering [4]. The inset shows a side view of the junction and connection of the RF electrodes.

away from the experiment zone. A mask layer for shielding neutral atom flux to the experimental zone also helped. After the ions are trapped and Doppler cooled in the load zone, they are shuttled to the experiment zone by applying a voltage waveform on the DC electrodes.

We have ovens as sources of ^{9}Be and ^{24}Mg(^{25}Mg) atoms. The ^{9}Be oven is composed of a ^{9}Be wire twisted onto a tungsten wire, which is made into a spiral which is mounted to leads that are connected to a current source which heats the oven. Resulting ^{9}Be atoms that pass through the load zone are ionized by either an electron gun, or using a 235 nm photoionization laser, detailed below. The Mg ovens are composed of metal tubes that can be heated with current, with a slit pointing towards the trap, filled with enriched/non enriched ^{24}Mg atoms. The non enriched oven contains ^{25}Mg and ^{26}Mg atoms, and the loading of isotope is determined by the exact wavelength of the 285 nm photoionization laser. There is a oven shield to block unwanted atom emission to the trap chip with a hole for the load zone.

We use a 235 nm pulsed laser source to ionize neutral ^{9}Be atoms. The process is to drive a transition from $1s^2 2s^2$ to $1s^2 2s2p$, centered at 234.9329 nm [80], and then further excite to the continuum for the $2p$ electron at a wavelength below resonance at 306.492 nm. We use one pulsed laser at 235 nm to drive this two-step process. Additionally, the 313 nm Doppler cooling laser for loading can also drive the second stage of transition. The setup, as depicted in Fig. 2.5 is mainly composed of a 705 nm laser source and a frequency “tripler” producing 235 nm light. The 705 nm source is composed of a 532 nm 5 W Verdi pumped Ti:Sapph mode locked laser from K-M labs[3] , where we tune the center wavelength to 705 nm, the spectrum with a full width half maximum of ∼13 nm, repetition rate ∼100 MHz and pulse duration of sub-100 fs. This beam is then sent into a frequency tripler from APE[4] , where the frequency is first doubled to 352.5 nm then sum with 705 nm to produce 235 nm light.

With normal operation of the Verdi V5 at 5.5 W, we typically obtain 600 mW average power on the 705 nm laser, and 8 mW average power on the 235 nm output. We find that even with 4

---

[3] the KM Labs Griffin Ti:Sapphire pulsed laser

[4] APE GmbH Prüfprotokoll frequency trippler setup

mW average power before injecting to the chamber, we typically load a ^{9}Be$^+$ ion within tens of seconds[5] .

For ionization of ^{24}Mg and ^{25}Mg atoms, we use a 285 nm CW source, frequency doubled from a 570 diode laser source[6] . This source excites ^{24}Mg atom from the $3s^2\ ^1S_0$ state to the $3s3p\ ^1P_1$ and further to the continuum state [81, 82].

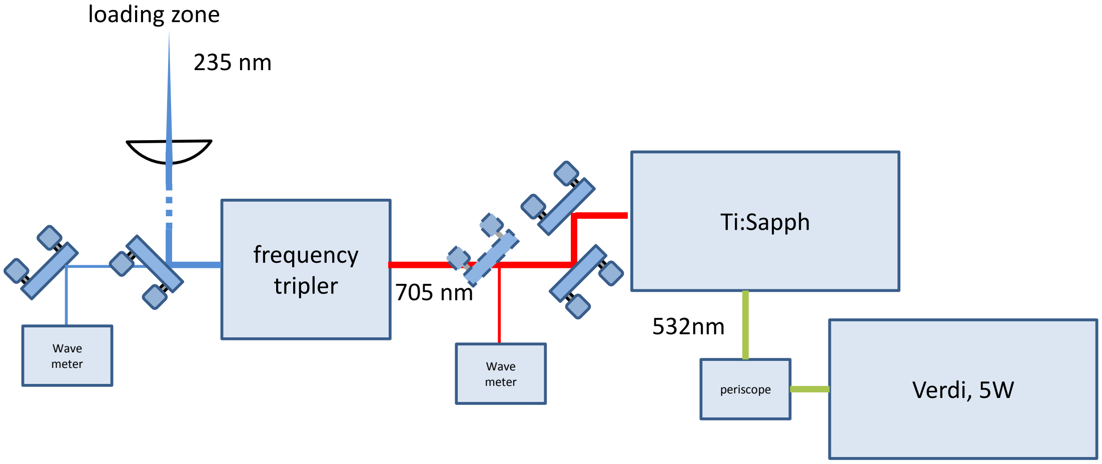

Figure 2.5: Schematic for the ^{9}Be photoionization laser setup. The mirror mount in dash outlines is a pick off mirror, which is not in the setup except for checking spectrum for 705 nm light. The mirror at the output of the tripler has finite transmission that leaks a small portion of 235 nm light for wavelength monitoring.

2.3.2 Vacuum system

The vacuum system is required to provide low background gas collision rates. The elastic collisions can lead to ion motional heating, excitation to complicated motional trajectory (decrystalization). The worst effect of the collisions is that can lead to chemical effects and turn Be$^+$ or Mg$^+$ ions into molecules. A typical example is for ^{9}Be$^+$ ion experiments, during detection, repumping or Doppler cooling, lasers are applied repeatedly to drive the $^2\mathrm{S}_{1/2} \rightarrow ^2 \mathrm{P}_{1/2,3/2}$ transitions, and the excited P states of a ^{9}Be$^+$ ion are chemically reactive to collisions with an H_2 molecule, and

---

[5] Loading time is limited by the warm up time of the oven.

[6] MPB Raman Amplifier system, seeded by Sacher diode laser ∼1140 nm and doubled by PPLN crystal. Output power 1.6 W. Wavelength set to 570.5925 nm

can be converted to a BeH^+ ion [22].[7]

A typical vacuum pressure for our system is 8×10^{-10} Torr $\sim$ 1×10^{-7} Pa. The vacuum assembly consists of a quartz cell joined to stainless steel Conflat vacuum parts, depicted in Fig. 2.6. The windows for laser access are made from UV-grade fused silica. Other parts in the system are: an ion pump[8] to maintain the vacuum environment; a titanium sublimation pump (TSP) to aid in removing excess hydrogen molecules; a quartz cell to cover the trap and resonator; and a Conflat interface for an ion gauge and electrical feed-throughs for the RF, DC and oven connections.

2.3.3 Imaging system

The imaging system is consist of magnifying imaging optics, an iris at the intermediate focus for blocking stray scattered light, and a flipper mirror to direct fluorescence to either a UV sensitive charge coupled device (CCD) camera[9] or a photo multiplier tube (PMT)[10] . The CCD camera provides a relatively large field of view that is very helpful for beam alignment to the trap features (corners, gaps and junctions), checking unwanted laser background scattering, and most importantly for identification of individual ions loaded in the trap. The PMT functions as a single pixel sensitive detection device that give counts for ion state dependent photon scattering, as the main measurement device for ion spin states. Typically for 300 μs detection duration for a single $^9\mathrm{Be}^+$ ion, the imaging system gives ~1 count if the ion is in the dark spin state, an ~25 counts in the bright state. The path of fluorescence to either the CCD camera or the PMT is switched by the mechanical flipper mirror. A housing made from aluminum provide mounting for the CCD camera, PMT and the flipper, also provides shielding from ambient room light.

For the linear trap setup, we use a two-step magnification for $^9\mathrm{Be}^+$ ion detection. The first step is a 5x ~f/1 lens, whose input surface is located ~40 mm from the ion trap. A second stage

---

[7] This turns out to be a significant problem for quantum simulation experiments in a Penning trap [83], where hundreds of $^9\mathrm{Be}^+$ ions are trapped and the BeH^+ ions are frequently observed. A technique is developed to dissociate the molecule back to $^9\mathrm{Be}^+$ ion with a 157 nm UV laser, guided with nitrogen gas tube to prevent high laser power loss in air [84].

[8] Agilent Varian StarCell pump

[9] Princeton Instrument PhotonMax 512

[10] Hamamatsu R7600P

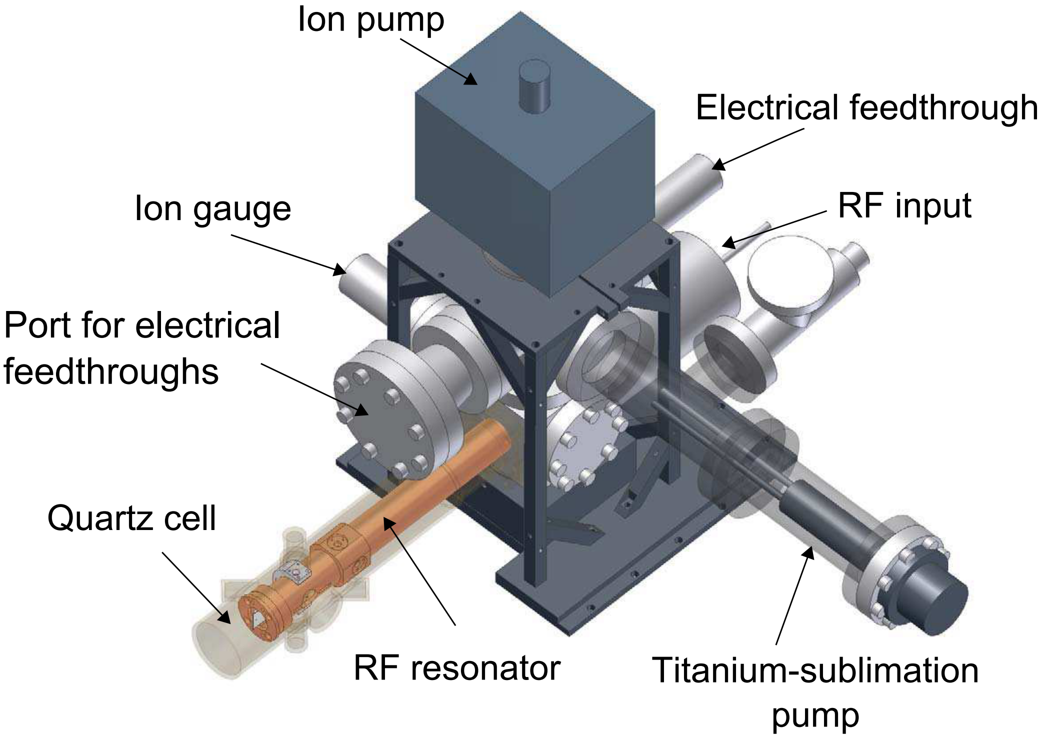

Figure 2.6: A mock up of the vacuum setup [3], showing relevant vacuum components. The Quartz cell has six windows made from fused silica for UV light access, and four of them are used for laser access and one is used for imaging. On the input end of the resonator, there is a cylindrical component to connect the center conductor to the ground. The output of the RF source after the amplifier is connected to a small wire loop, mounted inside the can to couple RF power into the resonator.

of $\sim$ 25x magnification is provided by a UV microscope objective. For the junction trap, since we need to image both $^{9}\mathrm{Be}^{+}$ and $^{25}\mathrm{Mg}^{+}$ at the same time without moving the imaging optics, we use a Schwardzchild imaging optics [85], design by P. Huang and D. Leibfried, and built by Sill optics. The idea is to use curved reflective optics with proper coating for both the 313 nm and 280 nm laser throughout. For this setup, the Schwarzschild imaging optics provides an amplification of 10x, and the output is further amplified by 5x through a second stage of a curved-flat mirror set, built by T. R. Tan. To compensate for the differential refraction of 313 nm and 280 nm light through the fused-silica vacuum window, a combination of fused-silica and CaF_2 optical components are included between the vacuum window and the first reflective curved mirror.

2.3.4 Magnetic field coils

We apply an external magnetic field to lift the degeneracy of the hyperfine states of the ion.[11] The field coil is in a Helmholtz configuration, to provide a nearly homogeneous field near the trap center. With this external field, the lasers have a well-defined quantization axis, where $\sigma^{\pm}$ polarized light propagates along the field direction, and π polarized light propagates perpendicular to the field direction with the electric field pointing along the magnetic field direction. Details are described in the Sec. 3.2. Laser beam access to the trap determines the design of the magnetic field coil so that the field is oriented 45° with respect to the trap axis, and the gap of the two Helmholtz coils provides laser beam access to the π light. The shape of the coil is designed to be approximately square (about the coil axis) for ease of installation.

For $^9\text{Be}^+$ ions, we apply an 11.9446 mT field, to minimize the magnetic field sensitivity on two of the ground hyperfine states, which we select as qubits. Details are described in Sec. 3.1. To generate this relatively high field, we need to apply 62.38 A static current[12] to the coil (4.8 V) made with 9 turns of copper tubing through which water is circulated [3]. In addition to the main coil, we also have other smaller coils whose fields are mutually orthogonal. The ones along the direction of the main quantization field provides fine tuning of the field strength to match the qubit insensitive point; other coils that are orthogonal to the main quantization field, to fine tune the magnetic field direction to be aligned with the axis of the $\sigma^{\pm}$ laser beams, and have the option to compensate for unwanted field gradients across the ion chain. More importantly, these coils can

---

[11] The external magnetic field could be generated by a permanent magnet, but the thermal stability of the field strength from these magnets was a concern. Despite this drawback, by bringing the magnet close enough to the ion location, a significant magnetic field gradient can be generated, which can be used to generate spin-motion coupling [86]. For experiments where decoherence due to the magnetic field stability is not a major issue, a simple coil with moderate current to generate a few Gauss is enough to resolve the hyperfine states.

[12] Agilent 5682A

provide compensation of the slow magnetic field drift, by recalibrating the currents after every 5 min[13] .

2.3.5 Experiment controls

For the experiments, we need to (1) dynamically control the duration, phases, frequency and amplitudes of laser and microwave pulses, (2) collect photons and (3) we need to dynamically control the voltages on the electrodes for ion shuttling, separation and recombination. This control system is based on various field-programable-gate-arrays (FPGAs) and a graphical-user-interface (GUI) [5, 87]. An FPGA consists of reconfigurable integrated circuits that can form user-specified digital logic operations, between the inputs and outputs. The first requirement is achieved by control of the input radiofrequency, to the AOMs for the laser and to the dipolar antenna, described in previous sections. The second requirement is achieved by taking the output of the PMT as a transistortransistor logic (TTL) signal which is sent to the master FPGA. The last requirement is satisfied with a waveform generator with fast digital-analog-convertors (DACs) and a onboard FPGA described in detail at [5].

The RF is generated by Direct-Digital-Synthesizers (DDS)[14] that outputs frequencies up to approximately 480 MHz, referenced to a 1 GHz clock. This clock is derived by the 10 MHz Hydrogen maser source at NIST. We amplify the DDS RF signal up to ∼2 W to drive the AOMs. To generate microwave signals, we take the DDS outpupt signal centered at 250 to 300 MHz and double twice to reach the ion transition frequencies at 1 to 1.2 GHz for $^9\text{Be}^+$.[15] To generate a pulse, the RF signal is connected to a TTL controlled RF switch. We use 16 independent TTL channels and 16 independent DDS channels, controlled by a FPGA[16] with a commercial evaluation board[17] clocked at 62.5 MHz. The FPGA receives the commands sent by the user through the

---

[13] These smaller coils are either driven by Agilent U8001A with typical current of 0.6 A or computer controlled with Agilent 6614C with General Purpose Interface Bus (GPIB) to Universal Serial Bus (USB) interface. Experimentally we observe the field on the ion has a noticeable dependence with the location of the aluminum lens mounts near the trap.

[14] The DDS we use are AD9858. A newer versions AD9914 is deployed for the ion clock experiments.

[15] Similar procedure with an extra doubling step is done for $^{25}\text{Mg}^+$ ion for other experiments.

[16] Xilinx Virtex-IV

[17] Xilinx Xtreme DSP kit

GUI, then sends out signals that changes the status of the TTL and DDS modules.

The laser amplitude control is done by using a Newport LB1005 servo box, where shortly after the laser pulse is turned on, the servo box is triggered to start servoing the RF amplitude to stabilize the laser intensity. We partially reflect the UV laser beam out of the UV fiber to photodetectors. Thus the laser beam pointing fluctuations before the fibers are converted to intensity fluctuations at the output. So this system takes care of beam pointing fluctuations as well as laser power fluctuations. The lock point of the intensity on the servo lock is either set by hand, or can be set by a GPIB controlled voltage source. Thus we can scan the laser intensity if needed. When the pulse is turned off, the servo box is set to the holding stage, keeping the output voltage to be constant without active servoing. [18]

---

[18] This process can be simplified by using a digital servo system, designed by David Leibrandt at NIST. This system uses a local FPGA, with Xilinx Spartan Spartan 6 LX150 with Opal Kelly XEM6010-LX150 evaluation board. The photodetector signal is digitized by a analog-digital-convertor (ADC), processed by the FPGA, and the servo signal is generated by DAC. This system is much more versatile than the analog counterpart, and custom servo functions and filters can be programmed.

Chapter 3

^{9}Be$^+$ qubit

A qubit for a trapped ion can be implemented with two internal hyperfine states. For the case of ^{9}Be$^+$ ion, the magnetic dipole radiative decay lifetime between the eight hyperfine ground states is very long, on the order of 10^{15} s [22]. The coherence time between the two hyperfine states can be affected by fluctuations in the ambient magnetic field; however frequency fluctuations can be made equal between specific pair of hyperfine states by properly setting the magnetic field. Using such states as qubits, the coherence time can be made very long, up to tens of seconds with proper choice of magnetic field [73]. To perform quantum information processing, before the experiment, we need to initialize one qubit state with high probability. Also after the experiment, we need to detect the populations of the qubit states. In this chapter, we will describe these processes.

3.1 ^{9}Be$^+$ energy levels

Beryllium, and in general the alkaline earth atoms, have two valence electrons. For ^{9}Be$^+$ ion, the valence electronic structure is similar to alkali atoms which is commonly used in trapped neutral atom experiments. The ^{9}Be$^+$ ion ground electronic configuration is the $1s^22s\ ^2S_{1/2}$ states, and for excited states we normally only take into account the $1s^22p\ ^2P_{1/2}$ and $1s^22p\ ^2P_{3/2}$ states. As depicted in Fig. 3.1, the electric dipole transition wavelength between the S to P states is approximately 313 nm, and the frequency difference between the two P states is approximately 197 GHz [88]. The hyperfine splitting between the $2s\ ^2S_{1/2}$ states is 1.2 GHz, due to the coupling between the ^{9}Be$^+$ nuclear spin $I = \frac{3}{2}$ and the spin of the valence electron. The hyperfine levels are labeled as F=1 and F=2, the former with higher energy.

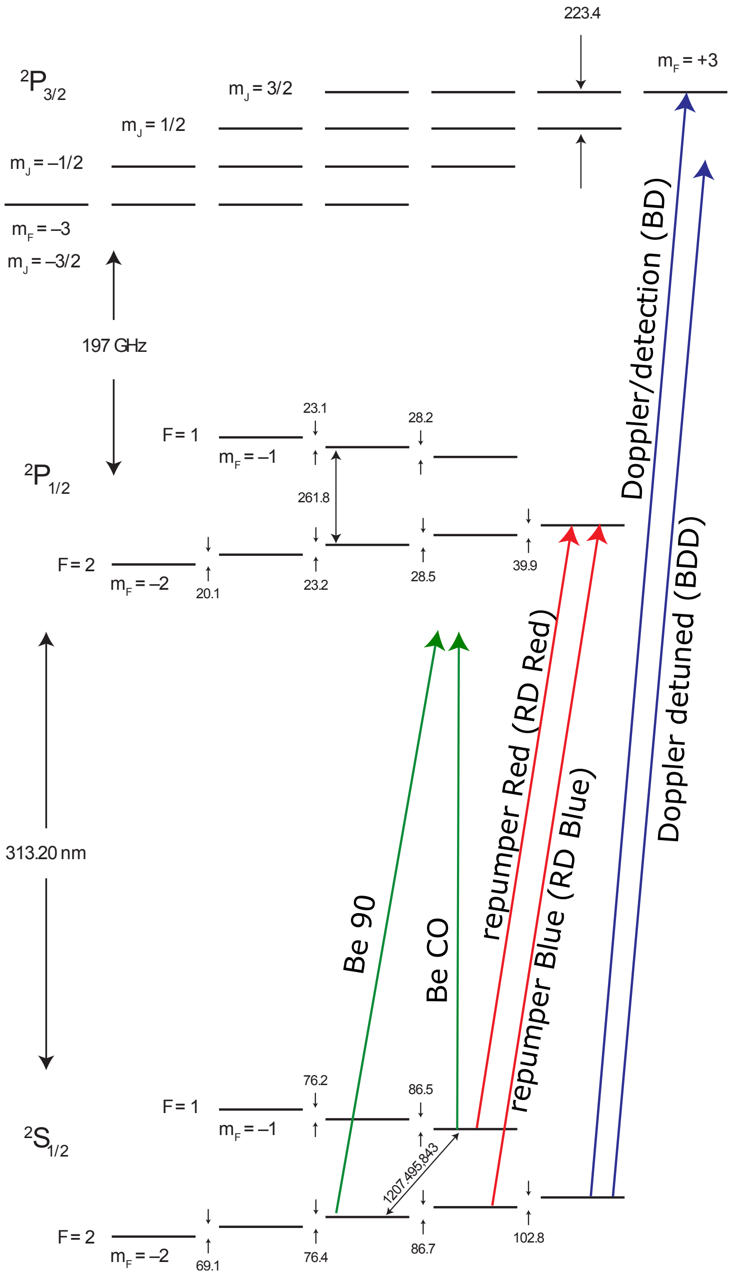

Figure 3.1: Schematic for the ^{9}Be$^+$ ion electronic transitions at 11.9446 mT magnetic field. Laser beams are shown to address various levels, see text. The relevant energy splittings are shown, and the transition $|2,0\rangle \leftrightarrow |1,1\rangle$ with transition frequency 1207.495843 MHz is to first order insensitive to magnetic field fluctuations. A typical Raman laser configuration driving the qubit transition is shown. At 11.9642 mT magnetic field, there is another first order field insensitive transition $|2,1\rangle \leftrightarrow |1,0\rangle$ of frequency 1207.352808 MHz.

To further split and resolve the hyperfine manifolds, we apply an external magnetic field to induce the Zeeman effect. A typical field strength in our experiment is 11.9446 mT to obtain first order insensitivity to field amplitude fluctuations for certain transitions. For the $2s\ ^2S_{1/2}$ states, the Hamiltonian considering the electron spin, nuclear spin under the influence of their interactions and the magnetic field $\mathbf{B}$ is

$$H_{\text{Zeeman}} = hA\mathbf{I}\cdot\mathbf{J} - \boldsymbol{\mu}\cdot\mathbf{B} \tag{3.1}$$

$$= hA\mathbf{I}\cdot\mathbf{J} + \mu_B(g_J\mathbf{J} + g_I\mathbf{I})\cdot\mathbf{B}, \tag{3.2}$$

where h is the Planck constant, $\mathbf{J} = \{\sigma_x, \sigma_y, \sigma_z\}/2$ is the angular momentum operator for the $2s\ ^2S_{1/2}$ states, $\sigma_{x,y,x}$ are the Pauli operators, $\mu_B = h13.996$ MHz/mT is the Bohr magneton, $A = -625.008837048(10)$ MHz is the hyperfine constant [89] and $g_{J/I}$ is the corresponding Landé g-factor. The measured values are g_J=2.00226206(42) and $\frac{g_I}{g_J}$=2.134779853(2)$\times10^{-4}$ [89]. In general, $g_J \approx 1 + \frac{J(J+1)+S(S+1)-L(L+1)}{2J(J+1)}$. $\mathbf{I} = \{I_x, I_y, I_z\}$ is the nuclear spin operator, where

$$I_x = \frac{1}{2}\begin{pmatrix} 0 & \sqrt{3} & 0 & 0 \\ \sqrt{3} & 0 & 2 & 0 \\ 0 & 2 & 0 & \sqrt{3} \\ 0 & 0 & \sqrt{3} & 0 \end{pmatrix}, I_y = \frac{1}{2}\begin{pmatrix} 0 & -\sqrt{3}i & 0 & 0 \\ \sqrt{3}i & 0 & -2i & 0 \\ 0 & 2i & 0 & -\sqrt{3}i \\ 0 & 0 & \sqrt{3}i & 0 \end{pmatrix}, \tag{3.3}$$

$$\text{and } I_z = \frac{1}{2}\begin{pmatrix} 3 & 0 & 0 & 0 \\ 0 & 1 & 0 & 0 \\ 0 & 0 & -1 & 0 \\ 0 & 0 & 0 & -3 \end{pmatrix}. \tag{3.4}$$

Here we choose the z-axis along the magnetic field with $B = B_z = |\mathbf{B}|$, and the z projections of $\mathbf{I}$ and $\mathbf{J}$ are labeled as m_I and m_J, respectively. At $B = 0$, the total angular momentum $\mathbf{F} = \mathbf{I} + \mathbf{J}$ is conserved, and thus $|F, m_F = m_I + m_J\rangle$ represent the eigenstates. The eigenenergies and eigenstates can be found by using the Breit-Rabi formula [90]. At low field, the energy shifts for the $|F, m_F\rangle$ states are well approximated by $(hg_F\mu_B B m_F)$, where $g_F = \frac{F(F+1)+J(J+1)-I(I+1)}{2F(F+1)} = \pm\frac{1}{4}$

for $F = 2$ and $F = 1$, respectively. These energy shifts can be obtained by treating the second term of Eq. 3.1 as a perturbation. However, for higher magnetic fields, the perturbation theory is no longer valid, and we need to diagonalize Eq. 3.1 to obtain the correct energy levels and eigen-energy E, as depicted in Fig. 3.2, where we also plot the energy sensitivity $\frac{dE}{dB}$. At certain B field amplitudes, the sensitivities of the levels are equal, so that any fluctuations of the B field amplitude will be first order homogeneous to these levels. Thus, transition frequency between these levels are to the first order insensitive to B field fluctuations. In Table. 3.1 we summarize the field insensitive points, the relevant transitions between the $|i\rangle$ and $|j\rangle$ states, and the difference of second order sensitivities $\Delta\frac{d^2E}{dB^2} = |\frac{d^2E_i}{dB^2} - \frac{d^2E_j}{dB^2}|$.

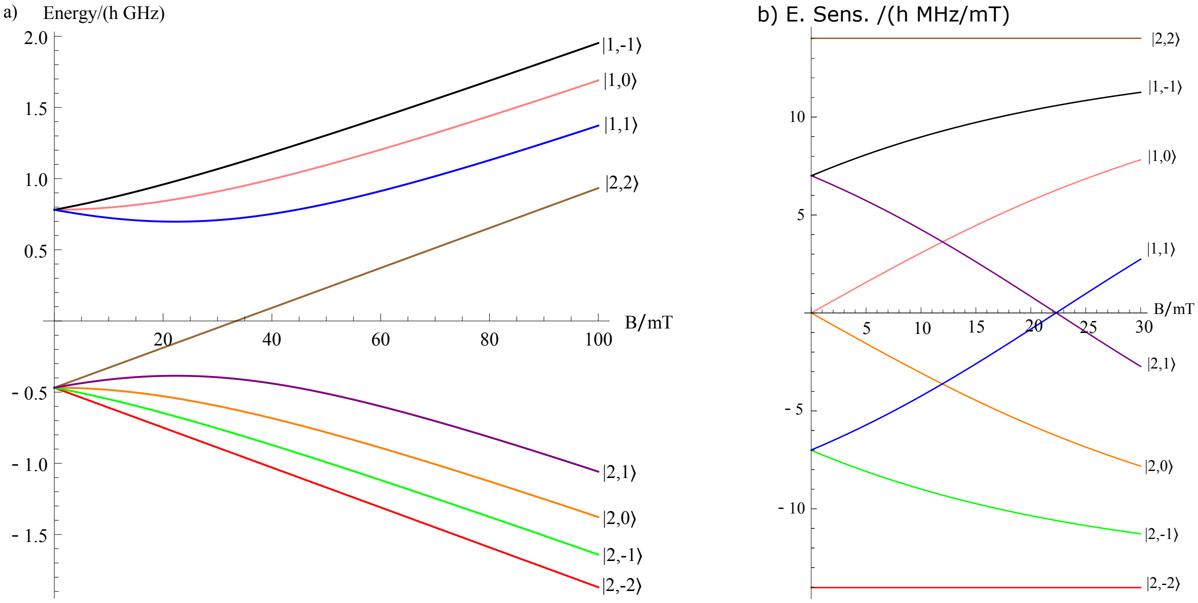

Figure 3.2: a) Energy levels in unit of (h GHz) by diagonalizing Hamiltonian in Eq. 3.1 over the external magnetic field B in mT. The eigenstates are labeled in the format of $|F, m_F\rangle$. For $B \neq 0$, F is no longer a good quantum number although m_F is. Here we just label the levels with the order of the energies, in conjunction with the low field case. b) The energy sensitivity $\frac{dE}{dB}$ in the unit of (h MHz/mT) over the external magnetic field.

Normally we operate at a magnetic field $B \approx$11.944618 mT. At this field, the field sensitivity $\frac{dE}{dB}$ of the $|F = 2, m_F = 2\rangle \leftrightarrow |1, 1\rangle$ transition is 17.644091 (h MHz)/mT. This is important for the $|1, 1\rangle \leftrightarrow |2, 2\rangle$ transition for state initialization and detection, as we describe in Sec. 3.3. At this field, the eigenvalues for the hyperfine states are listed in Table 3.2, compared with the case of zero

transition	frequency (GHz)	B (mT)	$\Delta\frac{d^2E}{dB^2}$(h MHz/mT^2)
$\lvert F=2,m_F=0\rangle \leftrightarrow \lvert 1,1\rangle$	1.207496	11.944618	0.609734
$\lvert 2,1\rangle \leftrightarrow \lvert 1,0\rangle$	1.207353	11.964241	0.609765
$\lvert 2,1\rangle \leftrightarrow \lvert 1,1\rangle$	1.082547	22.307269	0.725158
$\lvert 1,0\rangle \leftrightarrow \lvert 1,1\rangle$	0.322552	160.181925	0.001059
$\lvert 2,0\rangle \leftrightarrow \lvert 2,1\rangle$	0.324548	174.719221	0.000625

Table 3.1: Some field insensitive points with the relevant transitions and frequencies, and the difference of second order sensitivities. Here we list only field-insensitive points for B in the range of 11 mT to 180 mT. In this thesis we mainly work on fields for the first two entries, with $\Delta m_F = \pm 1$. For the higher fields the insensitive points are located at $\Delta F = 0$ transitions, and the higher order field sensitivity is significantly lower than the $\Delta F \neq 0$ insensitive transitions. As this trend and Fig. 3.2 shows, for the high fields, the Zeeman effect is dominant over the hyperfine coupling $hA\mathbf{I}\cdot\mathbf{J}$, and the field sensitivity between $\Delta F = 0$ transitions becomes small. At higher fields of ~819.439 mT, a 303 MHz field insensitive transition between $\lvert m_I = -\frac{3}{2}, m_J = \frac{1}{2}\rangle \leftrightarrow \lvert -\frac{1}{2}, \frac{1}{2}\rangle$ has been demonstrated in a Penning trap [1] for applications as a frequency standard.

field.

states	expanded at $B = 11.944618$ mT	expanded at $B = 0$
$\lvert F=2, m_F=2\rangle$	$\lvert m_I = 3/2, m_J = 1/2\rangle$	$\lvert m_I = 3/2, m_J = 1/2\rangle$
$\lvert 2,1\rangle$	$0.609\lvert 3/2,-1/2\rangle + 0.793\lvert 1/2,1/2\rangle$	$\frac{1}{2}\lvert 3/2,-1/2\rangle + \frac{\sqrt{3}}{2}\lvert 1/2,1/2\rangle$
$\lvert 2,0\rangle$	$0.793\lvert 1/2,-1/2\rangle + 0.609\lvert -1/2,1/2\rangle$	$\frac{1}{\sqrt{2}}\lvert 1/2,-1/2\rangle + \frac{1}{\sqrt{2}}\lvert -1/2,1/2\rangle$
$\lvert 2,-1\rangle$	$0.912\lvert -1/2,-1/2\rangle + 0.410\lvert -3/2,1/2\rangle$	$\frac{\sqrt{3}}{2}\lvert -1/2,-1/2\rangle + \frac{1}{2}\lvert -3/2,1/2\rangle$
$\lvert 2,-2\rangle$	$\lvert -3/2,-1/2\rangle$	$\lvert -3/2,-1/2\rangle$
$\lvert 1,1\rangle$	$0.793\lvert 3/2,-1/2\rangle - 0.609\lvert 1/2,1/2\rangle$	$\frac{\sqrt{3}}{2}\lvert 3/2,-1/2\rangle - \frac{1}{2}\lvert 1/2,1/2\rangle$
$\lvert 1,0\rangle$	$0.609\lvert 1/2,-1/2\rangle - 0.793\lvert -1/2,1/2\rangle$	$\frac{1}{\sqrt{2}}\lvert 1/2,-1/2\rangle - \frac{1}{\sqrt{2}}\lvert -1/2,1/2\rangle$
$\lvert 1,-1\rangle$	$0.410\lvert -1/2,-1/2\rangle - 0.912\lvert -3/2,1/2\rangle$	$\frac{1}{2}\lvert -1/2,-1/2\rangle - \frac{\sqrt{3}}{2}\lvert -3/2,1/2\rangle$

Table 3.2: List of $2s\ ^2S_{1/2}$ ground states expanded in the $\lvert m_I, m_J\rangle$ basis, with coefficients rounded to the third digit. Compared with the states at zero field, except for the stretch states, the other states have modified coefficients. This table will be useful when calculating the coupling coefficients for the electric dipole transitions, since the selection rules are such that $\Delta m_I = 0$ and $\Delta m_J = 0, \pm 1$.

For the $2p\ ^2P_{1/2}$ and $2p\ ^2P_{3/2}$ states, $g_J \approx \{\frac{2}{3}, \frac{4}{3}\}$, respectively. The zero-field hyperfine splittings in the $2p\ ^2P_{1/2}$ states are 237 MHz [88]; the $2p\ ^2P_{3/2}$ hyperfine splitting is < 1 MHz [91]. At the field of 11.9446 mT, the Zeeman splitting of $2p\ ^2P_{3/2}$ can be approximated by $(hg_J\mu_B B m_J) \approx hm_J \times 223$ MHz with eigenstates approximated by $\lvert m_I, m_J\rangle$, since the Zeeman effect is dominant over the hyperfine couplings. For $2p\ ^2P_{1/2}$ states, a calculation similar to the $2s\ ^2S_{1/2}$ is performed.

This is done by using Eq. 3.1 $A_{\frac{1}{2}} \approx -118.6(3.6)$ MHz, and $g_I = 0.784955\frac{\mu_B}{\mu_N}$ [88], where μ_N is the nuclear magneton. More energy splittings are shown in Fig. 3.1.

states	expanded at $B = 11.944618$ mT
$\lvert F=2, m_F=2\rangle$	$\lvert m_I = 3/2, m_J = 1/2\rangle$
$\lvert 2,1\rangle$	$0.69458\lvert 3/2,-1/2\rangle + 0.719415\lvert 1/2,1/2\rangle$
$\lvert 2,0\rangle$	$0.844109\lvert 1/2,-1/2\rangle + 0.536171\lvert -1/2,1/2\rangle$
$\lvert 2,-1\rangle$	$0.934293\lvert -1/2,-1/2\rangle + 0.356505\lvert -3/2,1/2\rangle$
$\lvert 2,-2\rangle$	$\lvert -3/2,-1/2\rangle$
$\lvert 1,1\rangle$	$0.719415\lvert 3/2,-1/2\rangle - 0.69458\lvert 1/2,1/2\rangle$
$\lvert 1,0\rangle$	$0.536171\lvert 1/2,-1/2\rangle - 0.844109\lvert -1/2,1/2\rangle$
$\lvert 1,-1\rangle$	$0.356505\lvert -1/2,-1/2\rangle - 0.934293\lvert -3/2,1/2\rangle$

Table 3.3: List of $2p\ ^2P_{1/2}$ states expanded in the $\lvert m_I, m_J\rangle$ basis. Definitions are similar to Table 3.2 for $2p\ ^2P_{1/2}$. These components will be useful when describing the laser dipole coupling matrix element in this thesis.

3.2 Laser and microwave sources

From previous subsection, we have seen that the $^2S_{1/2}$ and $^2P_{1/2}$ hyperfine states can be expanded in the $\lvert m_I, m_J\rangle$ basis. Transitions can be driven with laser fields or microwaves. For $^9\text{Be}^+$ and $^{24}\text{Mg}^+$, we do not consider metastable states. For laser dipole transitions, the selection rule is that the laser can drive transitions that satisfy $\Delta L = 1$, $\Delta m_I = 0$ and $\Delta m_J = \{0, \pm 1\}$. Here L is the orbital angular momentum quantum number, the second condition is due to the fact that laser field interacts very weakly, and the latter depends on the laser polarization. From Table 3.2, when expanding the eigenstates in $\lvert m_I, m_J\rangle$ basis, at the field for our case the Zeeman effect only shifts the coefficients of the expansion compared with $B = 0$, without involving extra $\lvert m_I, m_J\rangle$ components. Thus we can safely view laser dipole transitions between $\Delta m_F = \{0, \pm 1\}$ for the selection rule, consistent with $\Delta m_F = \Delta m_I + \Delta m_J = \{0, \pm 1\}$. However it is important to note that the eigenstates are not precisely $\lvert F, m_F\rangle$, since F is not a good quantum number, and should be addressed by treatments leading to Table 3.2 and 3.3.

We use laser beams for cooling, detection, and spin and motional state manipulation. To simplify the laser setup, for transitions that are close to each other, we split a laser beam and modify their frequencies with Acousto-Optic Modulators (AOM) [92]. For a $^9\text{Be}^+$ ions, the transitions are depicted in Fig. 3.1. The $2p\ ^2P$ state linewidth is $\Gamma=2\pi\times19.4$ MHz. The “BD” (blue-Doppler) near detuned/detection laser, with wavelength approximately 313.13 nm, drives the cycling transition between the $2s\ ^2S_{1/2}|F=2, m_F=2\rangle$ state and the $2p\ ^2P_{3/2}|F=3, m_F=3\rangle$ excited state, to provide far and near detuned Doppler cooling, and to drive a cycling transition [93] to scatter photons for detection. The 400 MHz red detuned BD laser addressing $2p\ ^2P_{3/2}|3,3\rangle$ state is named with “BDD” (blue Doppler detuned), and is typically much stronger than other Doppler lasers, to power broaden the transition. It provides Doppler cooling to ions in case they are in a high-energy motional state due to background collisions or during the loading process. Since it’s far red detuned, this laser also provides optical pumping to clear the populations from other than the ground $|2,2\rangle$ state. More detail is described in Sec. 3.3

The repumper laser beams are named with “RD” (red Doppler). They repump the ground $|2,1\rangle$ and $|1,1\rangle$ states, are further named with RD blue and RD red respectively, with wavelength approximately 313.2 nm.[1] These RD lasers provide fine pumping to the $|2,2\rangle$ state with high probability, typically $\sim$0.999 in a few μs.

To drive the transition between the ground states, we apply two laser beams setup in a “Λ” configuration, as shown in Fig. 3.1, to implement two-photon stimulated Raman transitions. For the two beams with different incident angles, these beams can also serve to drive spin-motional excitation. These two beams are named as “Be CO” and “Be 90”, with frequency difference $\sim$1.2 GHz[2] . The Raman beam wavelengths are approximately either 313.29 nm or 313.36 nm for different experiments in this thesis. Details will be described in Chapter 4.

The laser beam access is depicted in Fig. 3.3. All the Doppler laser beams are ideally purely σ^+ polarized, to minimize depumpings from the $|2,2\rangle$ state. The Raman laser beams are set so that the Be 90 beam contains both $\sigma^\pm$ polarizations and the Be CO beam has π polarization[3] . To

---

[1] It is a historical reason for this naming although the RD lasers are not mainly setup to provide Doppler cooling.

[2] The Raman beams can be set to have frequency difference $\sim$1.0 GHz to drive motional sidebands on the $|2,2\rangle \leftrightarrow |1,1\rangle$ transition. The “CO” beam is also used as one of the co-propagating beams to drive Raman transitions in other experiments [92]. The “90” beam is 90 degree from the “CO” beams.

[3] In the case of driving co-carrier transitions, the CO beam can contain simultaneously π polization and $\sigma^\pm$

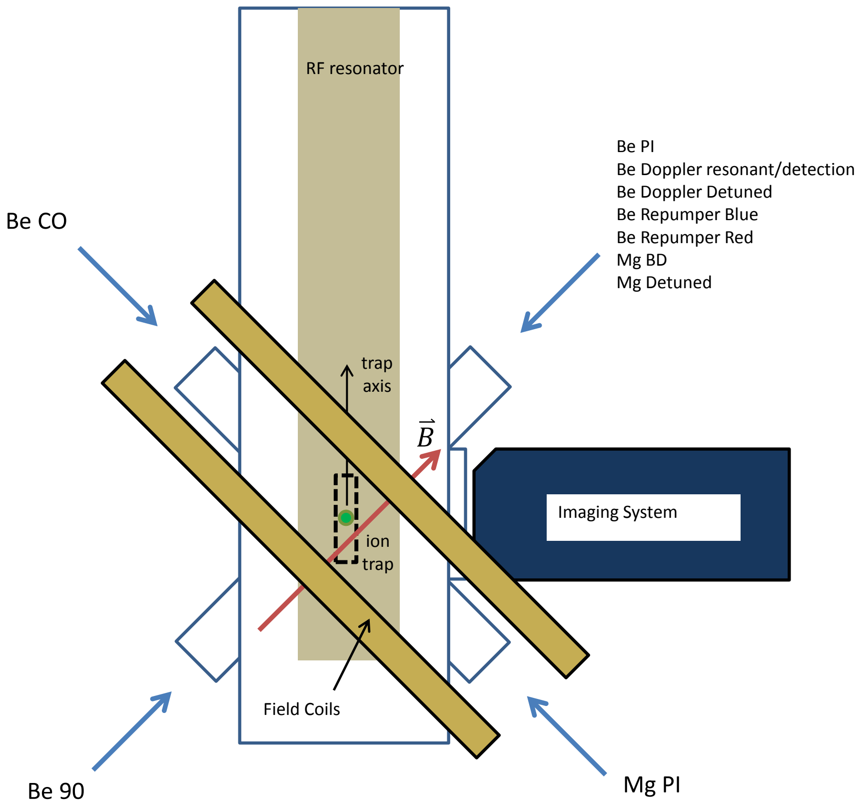

Figure 3.3: Schematic for laser access to the trap, not to scale. The magnetic field coil is set so that the magnetic field is 45° with respect to the trap axis. Be CO and 90 denote the Raman laser beams to address the $^9\text{Be}^+$ ion. PI denotes the photoionization beams. Blue hollow squares denote the outline of the glass chamber and the windows. Figure adapted from [5].

generate the laser beams above, we first generate 626 nm laser beams by frequency summing 1550 nm and 1050 nm fiber laser beams [94], then frequency doubling to 313 nm with a bowtie cavity with a Barium borate (BBO) crystal, as depicted in Fig. 3.5. To reference the frequency of the Doppler beams, we lock the 626 nm Doppler lasers to Doppler-free absorption lines from I_2 vapor cells, feeding back to piezos in the Doppler IR fiber seed lasers. The AOM setups to generate the BD and RD laser beams are shown in Fig. 3.4 and Fig. 3.6. After these beams are generated, they are combined with a 50/50 beam splitter and coupled through the UV fiber and sent to the trap. The Raman laser setup is shown in Fig. 3.7.

We also use microwave fields to drive transitions within the ground state manifold shown

---

polarizations by setting the beam to be linearly polarized with an angle between 0° and 90° from the magnetic field.

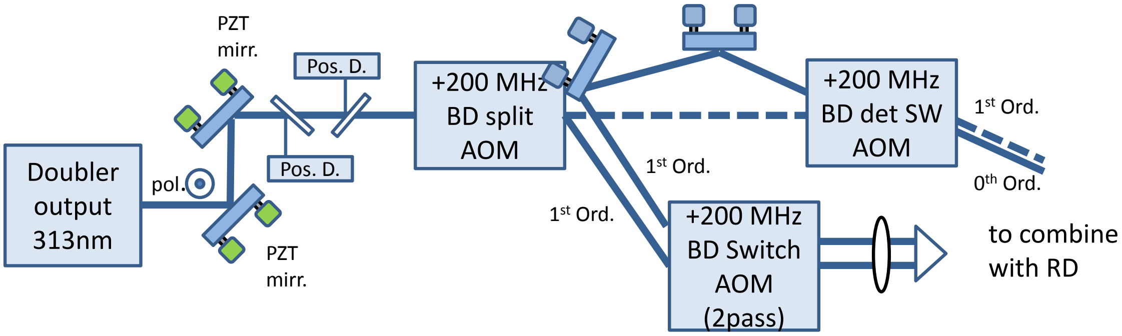

Figure 3.4: Schematic for BD laser beams setup. The output of the doubler has a vertical polarization with respect to the laser table. Pos. D. represents a two dimensional position detector (Newport Quadrant Cell); PZT mirror is a dual-piezo-driven mirror, capable of tipping both horizontal and vertical directions. Along the beam path, the first(second) Pos. D. feeds back to the first(second) PZT mirror with proportional-integrator loop. Thus the output beam pointing of the doubler is locked. The AOMs are not shown with actual orientation angle. The dashed beam line forms the BD far-detuned Doppler laser, and the solid beam line after the first AOM forms the BDD resonant/near detuned Doppler laser, with their frequency difference approximately 400 MHz. These two laser beams are combined at the BD det(detuned) SW(switch) AOM, where the BD beam is diffracted on the first order, which is overlapped with the undeflected BD beam. This configuration is due to the requirement of stronger far-detuned beam power than the near detuned one. Here some of the aligning mirrors are not shown. The double pass BD Switch setup uses a 15 cm lens placed at a focal length away from the center of the AOM. A corner cube retro-reflecting the beam with a vertical displacement, placed at the location that forms a one to one telescope with the lens. With this setup, the double pass alignment is insensitive to the change of AOM input frequency. The output of this setup is combined with the RD beams, then sent to the input of a UV fiber. The RF drive for BD switch AOM is actively noise-eat when the pulse is on. For this purpose, a pick-off mirror partially reflect the BD light to a detector, placed after the fiber, so that when the BD light is on, its power is actively stabilized.

in Fig. 3.1. The microwave transitions used in this thesis are summarized in Table 3.4. These transitions are used for various purposes, such as spin flopping and transferring from the $|2,2\rangle$ state to the spin state. For detection, we transfer one of the “bright” spin states to the $|2,2\rangle$ state for fluorescence detection.

Microwave transitions are induced in a brute-force manner with a dipole antenna, depicted in Fig. 3.9, that is external to vacuum system. This antenna is constructed by soldering two sections of copper wires to a SMA female connector. The length of these wires are set to 1/4 of the desired microwave wavelength. For ^{9}Be$^+$ and ^{25}Mg$^+$, two antennas are built for center frequencies of 1.2

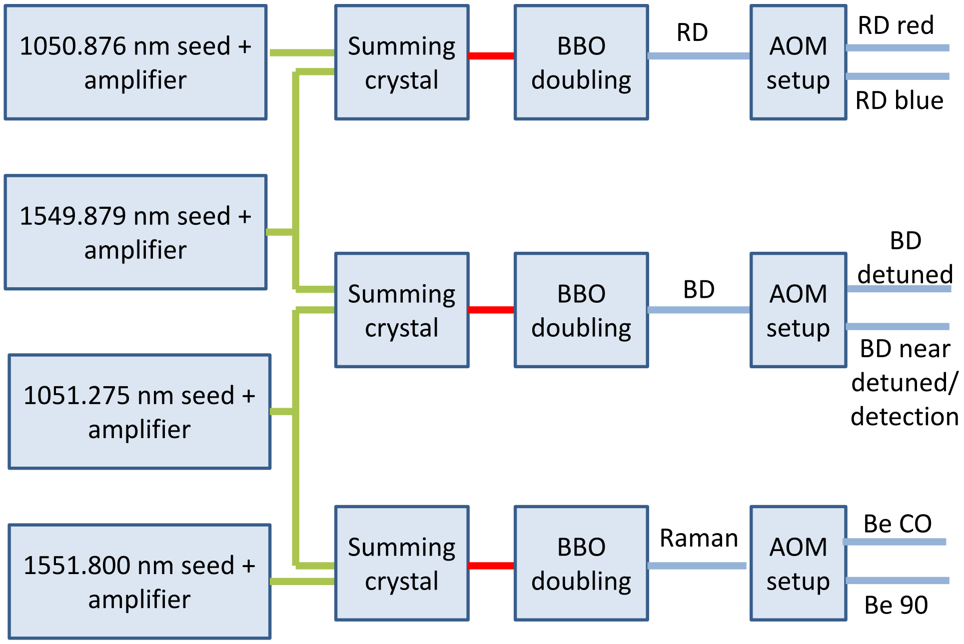

Figure 3.5: Schematic for laser beam generation. “BBO doubling” denotes the doubling cavity setup [6] with BBO as the nonlinear conversion medium. For the seed lasers, we use NKT Koheras Adjustik lasers, and for the upper two amplifiers, we use NKT Koheras Boostik HPA. For the lower two amplifiers, we use IPG Photonic Ytterbium/Erbium Fiber Amplifiers. The respective frequencies of the Raman beams are controlled by the AOM frequencies. The Doppler beams are recombined before sending through a UV capable photonic crystal fiber [7]. To Doppler cool and image on both the experimental zone and the load zone, we further split the Doppler beam on the fiber output with a Glan-laser, with relative intensity controlled by a motorized $\lambda/2$ waveplate.

GHz and 1.8 GHz respectively. The antennas are placed vertically above the trap, on top of the quartz cell. We further impedance match this antenna to the microwave source with a stub-tuner. The microwave frequency is generated by doubling the signal from the direct-digital-synthesizer (DDS) twice or three times, filtered, and then amplified with a 30 W amplifier[4] . With this configuration, the Rabi flopping π time for ^{9}Be$^+$ with various transitions is summarized in Table 3.4.

---

[4] Mini Circuit ZHL-30W-252+

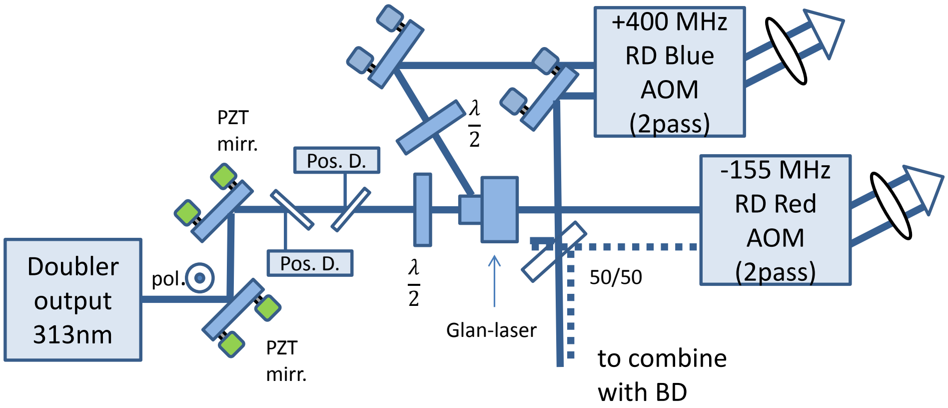

Figure 3.6: Schematic for RD laser beams setup. This setup is similar to the BD one, except that the generated beam frequency difference is approximately 1110 MHz, matching with the resonant frequency difference of the $|F = 1, m_F = 1\rangle$ and $|2, 1\rangle$ states. The $\frac{\lambda}{2}$ waveplates modifies the polarization of the laser beam, controlling the beam power splitted at the Glan-laser. The Glan-laser is setup so that the lower output beam is vertically polarized, and the upper output beam is horizontally polarized. The waveplate after the Glan-laser rotates the polarization back to vertical.

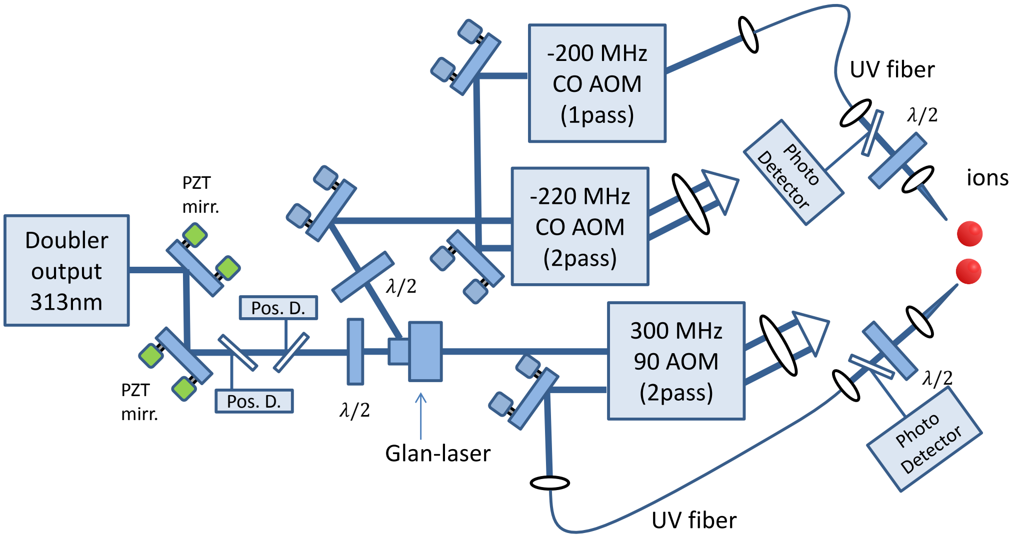

Figure 3.7: Schematic for Raman laser beams setup. This setup splits the Raman beam into the "CO" beam and the "90" beam, as indicated in Fig. 3.3. We adjust the frequency of the 90 AOM to drive transitions $|F = 1, m_F = 1\rangle \leftrightarrow |2, 2\rangle$ and $|1, 1\rangle \leftrightarrow |2, 0\rangle$. The CO beam line has an optional 600 MHz AOM double pass setup, to generate a pair of co-propagating CO beams to drive the carrier transition, which is not shown in the figure. For the double pass setup for Raman beams, the corner cube is replaced with three mirrors, to provide first order insensitive to AOM thermal refraction effect. This method is proposed by T. Rosenband, as shown in Fig. 3.8.

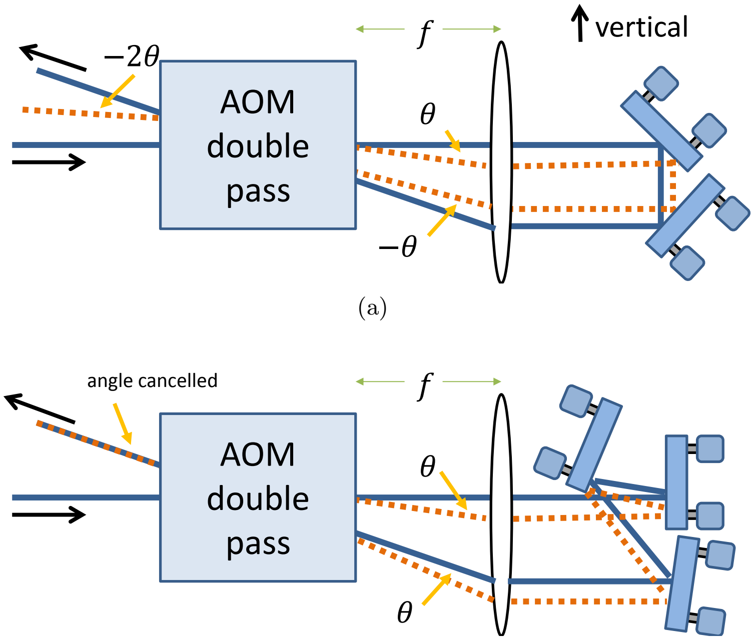

(a)

(b)

Figure 3.8: (a) Schematic for the "two mirror" double pass setup in a side-view. Here only the diffracted beams are shown as the AOM outputs but the actual the diffraction directions are perpendicular the page. The dashed orange line shows the deviation angle θ due to the AOM thermal thermal refraction effect. This effect can result from inhomogeneous distribution of RF power inside the AOM, or from inhomogeneous heat dissipation along the vertical directions in the figure. In this case, after double passing the AOM, the angular deviation is doubled. The lens is placed at a focal length f away from the AOM, and the round trip path length between the lens and mirrors is $2f$. (b) Schematic for the "three mirror" double pass setup. For three mirror setup, the deviated beam experiences a cancelling thermal refraction effect and the double pass output is overlapped with the beam where the thermal refraction effect is absent.

transition	frequency(MHz)	π time(μs)
$\|F=2, m_F=2\rangle \leftrightarrow \|1,1\rangle$	1018.007400	7.4
$\|1,1\rangle \leftrightarrow \|2,0\rangle$	1207.495843	7.2
$\|2,0\rangle \leftrightarrow \|1,0\rangle$	1294.042400	11.7
$\|2,0\rangle \leftrightarrow \|1,-1\rangle$	1370.290005	88.8
$\|2,1\rangle \leftrightarrow \|1,1\rangle$	1120.806368	4.4
$\|2,1\rangle \leftrightarrow \|1,0\rangle$	1207.352925	10.6

Table 3.4: typical π time of the Rabi flopping of the microwave transitions

3.3 State initialization

As we have seen in previous section, the ^{9}Be$^+$ ion has multiple ground states. To have a repeatable starting point for the experiment, we need to transfer, or reset, the ion population to a

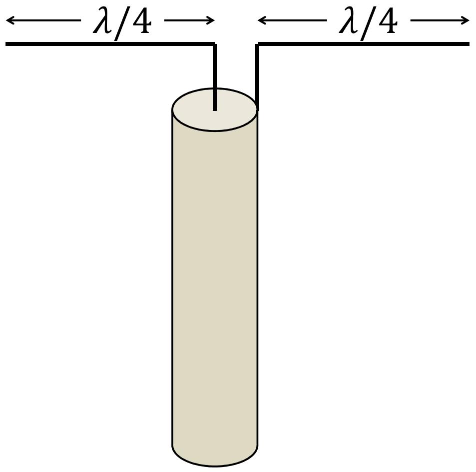

Figure 3.9: Schematic for the dipolar antennas in the experiment, not to scale. The microwave wavelength id denoted by λ. One arm of the antenna is soldered to the center conductor of the SMA, and the other end is soldered to the outer conductor.

fixed state. This operation is referred to as state initialization or state preparation. We apply optical pumping, a dissipative process that takes advantage of the selection rules of the transition between the ground and excited states. Consider transitions between $^2S_{1/2}$ and $^2P_{3/2}$ states. For a σ^+ polarized[5] BD detuned laser beam due to power broadening, it can off-resonantly drive transitions from several of the $^2S_{1/2}$ states to the excited $^2P_{3/2}$ states, with selection rule $\Delta m_J = +1$. The excited state decays back to the ground manifold with selection rule of $\Delta m_J = 0, \pm 1$. Thus for one round of excitation-decay process, the net transition rule at the ground manifold is $\Delta m_J = 0, +1, +2$. Thus with one BD detuned beam, repeated pumping within the ground manifold occurs so that the m_J quantum number is being increased, until reaching the maximum number $m_J = 2$, corresponding to the $^2S_{1/2}|F = 2, m_F = 2\rangle$ state. This state is sometimes called the "stretched" state.

Due to the imperfections of the polarization of the BDD detuned beam, there is a finite probability that the wrong polarization can drive transitions with an overall change $\Delta m_F = -2, -1, 0$, a

---

[5] controlled by a combination of Glan-polarizer, $\lambda/4 - \lambda/2$ waveplate, mounted on a tip-tilt stage with waveplate rotations

depumping process. The equilibrium of the pumping and small depumping process results in a majority of the population in the stretched state, but there can still be a finite population[6] remaining in the $^2S_{1/2}|F=2, m_F=1\rangle$ and $|1,1\rangle$ states.

To increase the pumping success probability, we apply the σ^+ polarized "repumper" beams, the RD Red and RD Blue beams, to resonantly drive transitions of $^2S_{1/2}|F=2, m_F=1\rangle \rightarrow^2 P_{1/2}|F=2, m_F=2\rangle$, and $^2S_{1/2}|F=1, m_F=1\rangle \rightarrow^2 P_{1/2}|F=2, m_F=2\rangle$ respectively, and pump to the desired $^2S_{1/2}|F=2, m_F=2\rangle$. These beams will not drive transitions from the $^2S_{1/2}|F=2, m_F=2\rangle$ states, since $m_F=3$ states do not exist in the $^2P_{1/2}$ manifold. For imperfections of the polarizations of the RD Blue repumper, the nearest depumping transitions $^2S_{1/2}|F=2, m_F=2\rangle \rightarrow^2 P_{1/2}|F=2, m_F=\{2,1\}\rangle$ are $\sim$100 and $\sim$ 60 MHz detuned from resonance. Thus the depumping process is suppressed.

With the application of the BD detuned beam, then simultaneously the RD blue and red beams, we typically achieve a population $\sim$0.999 in the $^2S_{1/2}|F=2, m_F=2\rangle$ state.

For experiments where we want to initialize the ion to other states, we drive from the $|F=2, m_F=2\rangle$ to the desired state with either Raman transitions or microwave transitions. A typical desired initial state is the $|F=1, m_F=1\rangle$ state. Due to the magnetic field sensitivity of this transition, which leads to transition frequency fluctuations, we can apply the composite pulse technique [95]. One sequence we used for the experiment is $R\{\frac{\pi}{2}, 0\} - R\{\frac{3\pi}{2}, \frac{\pi}{2}\} - R\{\frac{\pi}{2}, 0\}$, where R denotes the rotation operation, θ and ϕ denotes the rotation angle and the azimuthal angle of a vector in the spin x-y frame about which the spin is rotated.

3.4 Detection

3.4.1 Photon collection

To detect the presence of the $^2S_{1/2}|F=2, m_F=2\rangle$ state, we use the BD resonant beam, which drives the "cycling" transition between this state to the excited $^2P_{3/2}|m_I=3/2, m_J=3/2\rangle$ state. The name cycling comes form the fact that the excited state can only decay back to the

---

[6] typically $< 1\%$ of population

${}^2S_{1/2}|F=2, m_F=2\rangle$ state. With the BD detection beam tuned close to resonance with the transition, when the ion is in the ${}^2S_{1/2}|F=2, m_F=2\rangle$ state, photons are repeatedly scattered, and thus the ion appears to be "bright". When the ion is in the other states, the number of the scattered photons will be significantly less, and the ion appears to be "dark". However, the BD detection beam can off-resonantly repump other ${}^2S_{1/2}$ states to the $|F=2, m_F=2\rangle$ state, and the ion subsequently becomes bright. This effect is significant for the $F=2$ states, and less significant for the $F=1$ states, due to the $\sim$1 GHz splitting in energy. The other effect is the lower the value of m_F, the more repump steps it takes to reach the bright $m_F=2$ state. Thus for detecting of the spin manifold $|F=2, m_F=0\rangle$ and $|F=1, m_F=1\rangle$ states, we first use a microwave π pulse to drive $|F=1, m_F=1\rangle \rightarrow |F=2, m_F=2\rangle$, so the bright state represents the $|F=1, m_F=1\rangle \equiv |\uparrow\rangle$. When a photon scattering event occurs, any superposition of the spin states will be "collapsed" into either the bright or dark state, and ideally remain therein through out the detection. We also apply a "shelving" technique [63, 96], to essentially make the "dark" $|F=2, m_F=0\rangle \equiv |\downarrow\rangle$ state even darker by transferring it to the $|1,-1\rangle$ state. However, experimentally we find this transition is much weaker than other transitions as shown in Table 3.4, and the transfer fidelity is not high due to magnetic field sensitivity. Thus we apply another microwave pulse before detection to transfer the residual populations in the $|2,0\rangle$ state to $|1,0\rangle$ state.

3.4.2 Maximal likelihood method

The photons collected can be shown as a histogram constructed over many repeated identical experiments; typical ones for two ions are shown in Fig. 3.10 (a). The histogram approximately follows Poisson distributions. The Poisson distribution describes the collection of photons, for an ion with a constant photon scattering rate, for a fixed duration of detection. With i ions in the bright state, the mean photon count is approximately proportional to i, and mean number of bright counts is typically $\sim$40 counts for a detection duration of 330 μs, as shown in Fig. 3.10 (a). Another example is the photon scattering of the $\frac{1}{2}(|\uparrow\uparrow\rangle + |\uparrow\downarrow\rangle + |\downarrow\uparrow\rangle + |\downarrow\downarrow\rangle)$ state. A simple procedure is to fit the histograms with with Poisson distributions to extract the probability of different ions in the bright state [87]. However, due to experimental imperfections, e.g. optical pumping, the photon scattering rate may not be constant since the dark state has a finite probability to be repumped into the bright state and start scattering photons. Similarly the bright state has a finite probability to be depumped and scatter less photons over time. Thus the histogram does not precisely consist of Poissonian components, and to fit it with high precision we need to model the repumping and depumping processes [87, 97, 98].

Recently, an alternative detection program has been developed to provide analysis independent of the model of the photon count distribution. This program[7] is coded in Python and Matlab developed by A. Keith, S. Glancy, K. Coakley and E. Knill at NIST, using maximum-likelihood method [99]. We first obtain a reference histogram with a microwave "Ramsey" pulse sequence of $R\{\frac{\pi}{2}, 0\} - R\{\pi, 0\} - R\{\frac{\pi}{2}, \phi\}$ flopping between the $|F = 2, m_F = 2\rangle$ and $|F = 1, m_F = 1\rangle$ states[8] , where ϕ is a scanned variable. Thus we obtain histograms shown in Fig. 3.10 (a) To mitigate the effects from finite number of experiments and speed up the analysis process, we apply a "rebinning" method, to sum up events in certain count ranges. As an example, the histograms in Fig. 3.10 (a) are divided into three sections, shown with vertical dashed lines. Each of the sections are summed up to form the histograms in Fig. 3.10 (b), respectively. We can see this rebinning process reflects the populations of P_i for each of the histogram, where P_i denotes probability of i ions in the bright state. For each of the reference histograms, we predict the coefficients for linear combinations of P_i from the Ramsey flopping, which we assume with negligible errors[9] . Then we numerically find the optimal histograms for $P_i = 1, i = 0 - 2$ to match with the coefficients and the rebinned reference histograms, as shown in Fig. 3.10 (c). This numerical process follows the maximum-likelihood method. This optimal histogram is used as a new reference to extract spin population from data of other experiments. For the entangled state experiments, to obtain the population of the target state $|\psi\rangle$, we also use maximum-likelihood method to find the best fit of density matrix ρ to both

---

[7] We compared the analysis given by this program with the model with the repumping and depumping processes and they give similar result.

[8] we use this sequence to echo out spin processions between the pulses due to slow magnetic field drifts

[9] To obtain the histogram for all ion bright, a more precise way is to directly measure the population after repumping to the $|2, 2\rangle$ state; and for all ion dark, a possible improvement is to apply a composite π pulse followed by shelving and ion fluorescence.

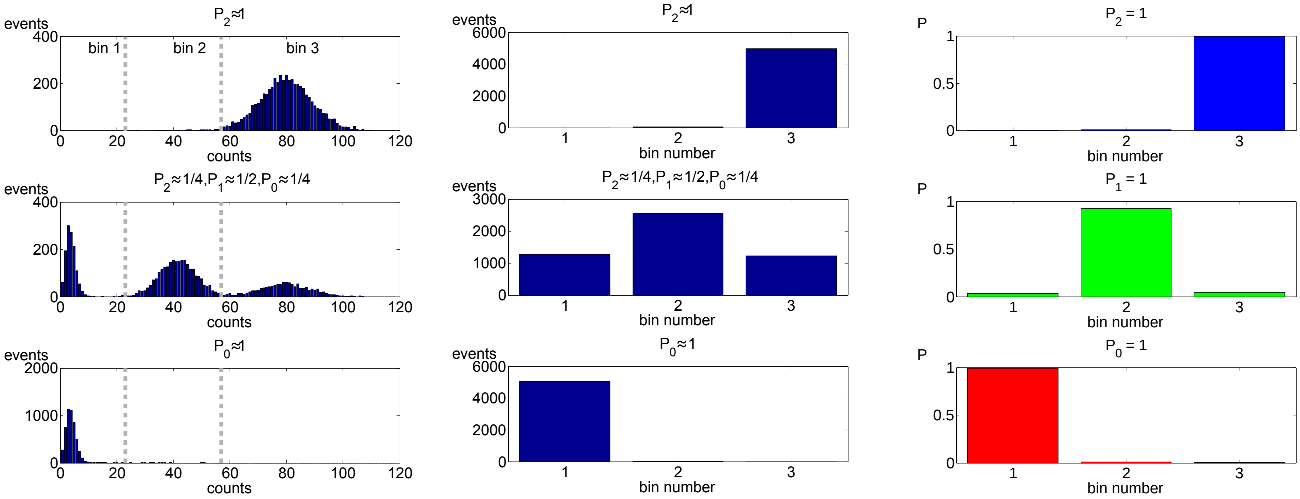

(a) (b) (c)

Figure 3.10: Typical histograms collected from a given detection process. (a) Histograms from Ramsey experiments showing the count histograms for various states. From top to bottom, histograms of approximately two, one, and zero ions in the bright states are shown, corresponding to $\phi = \{0, \pi/2, \pi\}$ respectively. Gray vertical dashed lines separate the histogram into sections of count ranges that can distinguish the number of ions in the bright state. (b) Sections in (a) are summed up to form "rebinned" histogram. The new bins are labeled as 1-3. (c) From the rebinned histograms and the predicted populations from the Ramsey sequence, a population reference histograms representing 0-2 ions in the bright state are obtained with the maximum likelihood method.

the histograms with and without the “analysis pulse”, detailed in the following section, according to the reference histogram. Then we obtain the population $P_\psi = \langle\psi|\rho|\psi\rangle$.

3.4.3 Symmetric entangled state detections

In this subsection, we will describe a general method of detection state $|\psi\rangle$, particularly for the symmetric entangled state for two and three ions. This is useful since for some experiments we have not had the capability to individually address the ions for detection. Here we set the dark and bright states to correspond to the states in vector form of $|\uparrow\rangle = \begin{pmatrix} 1 \\ 0 \end{pmatrix}$ and $|\downarrow\rangle = \begin{pmatrix} 0 \\ 1 \end{pmatrix}$ respectively. For an experimental outcome density matrix ρ of two ions, after we apply a unitary rotation U known as the “analysis pulse”, the detection of population P_i for i ions in the bright state can be expressed as

$$P_{i,U} = \mathrm{Tr}(\mathrm{U}\rho\mathrm{U}^\dagger\mathrm{A_i}) = \mathrm{Tr}(\rho\mathrm{U}^\dagger\mathrm{A_i}\mathrm{U}), \tag{3.5}$$

where $A_0 = |\uparrow\uparrow\rangle\langle\uparrow\uparrow|$, $A_1 = |\uparrow\downarrow\rangle\langle\uparrow\downarrow| + |\downarrow\uparrow\rangle\langle\downarrow\uparrow|$, $A_2 = |\downarrow\downarrow\rangle\langle\downarrow\downarrow|$ are the measurement operators to give the probability of i ions bright and Tr denotes the trace. Here we assume the unitary rotation and detection are global, and the populations stay within the symmetric states. Thus $P_{i,U}$ contains information of the experiment outcome. On the other hand, a theoretical measurement of the overlap of ρ and $|\psi\rangle$ is given by

$$P_{|\psi\rangle} = \langle\psi|\rho|\psi\rangle = \mathrm{Tr}(\rho|\psi\rangle\langle\psi|). \tag{3.6}$$

We can see $|\psi\rangle\langle\psi|$ is an observation of the state $|\psi\rangle$. Thus with the linear property of the matrix trace, we can find linear combinations of $U^\dagger A_i U$ to form the observation $|\psi\rangle\langle\psi|$. Here we apply U as single qubit rotation $R\{\theta,\phi\} = \begin{pmatrix} \cos(\frac{\theta}{2}) & -ie^{-i\phi}\sin(\frac{\theta}{2}) \\ -ie^{i\phi}\sin(\frac{\theta}{2}) & \cos(\frac{\theta}{2}) \end{pmatrix}$. With varied θ and ϕ. Changing notation, we write operator $R^\dagger\{\theta,\phi\}A_iR\{\theta,\phi\} = R_i\{\theta,\phi\}$. Here we give some examples of the pulse sequence and observations for different entangled states.

$|\psi_\phi\rangle = \frac{1}{\sqrt{2}}(|\uparrow\uparrow\rangle + e^{i\phi}|\downarrow\downarrow\rangle)$:

$$\begin{aligned}|\psi_\phi\rangle\langle\psi_\phi| = \frac{1}{2}(&A_0 + A_2\\ &+ (R_2\{\frac{\pi}{2}, \frac{\phi}{2} + \frac{\pi}{2}\} + R_0\{\frac{\pi}{2}, \frac{\phi}{2} + \frac{\pi}{2}\} - R_1\{\frac{\pi}{2}, \frac{\phi}{2} + \frac{\pi}{2}\})\\ &- (R_2\{\frac{\pi}{2}, \frac{\phi}{2}\} + R_0\{\frac{\pi}{2}, \frac{\phi}{2}\} - R_1\{\frac{\pi}{2}, \frac{\phi}{2}\}))\end{aligned}$$

$|T\rangle = \frac{1}{\sqrt{2}}(|\uparrow\downarrow\rangle + |\downarrow\uparrow\rangle)$: $\quad |T\rangle\langle T| = \frac{1}{2}A_1 + \frac{1}{2}\mathbb{1} - \langle R_1\{\frac{\pi}{2}, \phi\}\rangle_\phi$

$|S\rangle = \frac{1}{\sqrt{2}}(|\uparrow\downarrow\rangle - |\downarrow\uparrow\rangle)$: $\quad |S\rangle\langle S| = \frac{1}{2}A_1 - \frac{1}{2}\mathbb{1} + \langle R_1\{\frac{\pi}{2}, \phi\}\rangle_\phi$

Here $\mathbb{1}$ denotes the identity matrix, $\langle\cdot\rangle_\phi$ denotes an average of measurements over ϕ. For three ions, we have

$|W\rangle = \frac{1}{\sqrt{3}}(|\uparrow\uparrow\downarrow\rangle + |\uparrow\downarrow\uparrow\rangle + |\downarrow\uparrow\uparrow\rangle)$: $|W\rangle\langle W| = \frac{2}{3}A_3 + A_2 + \frac{1}{2}A_1 + \frac{1}{3}A_0 - \frac{3}{2}\langle R_2\{\cos^{-1}(\frac{1}{3}), \phi\}\rangle_\phi$.

For $|T\rangle$, we can give an intuitive explanation of the measurement operators. Since $|T\rangle$ is in the 1-ion bright manifold, we only need to distinguish it from $|S\rangle$, the other state in this manifold, in which case a measurement for A_1 can provide the population of $|T\rangle$ (as well as $|S\rangle$). In general, the key process of symmetric measurement is to distinguish the symmetric state (here $|T\rangle$) with the asymmetric states (here $|S\rangle$). We insert a microwave $\pi/2$ "analysis" pulse with variable phase before the collection of histograms. This pulse rotates the $|T\rangle$ state into superpositions of $|\uparrow\uparrow\rangle$ and $|\downarrow\downarrow\rangle$ states, while the $|S\rangle$ state is invariant. Measurement of populations in $|\uparrow\uparrow\rangle$ and $|\downarrow\downarrow\rangle$ states allow us to extract the $|T\rangle$ population. To make the measurement simple, we only need to subtract the residual population in the 1-ion manifold. Thus to get the $|T\rangle$ population subtract $R_1\{\frac{\pi}{2}, \phi\}$ from the combination of A_0 and A_2, and to get the $|S\rangle$ population, the $R_1\{\frac{\pi}{2}, \phi\}$ is added to A_0 and A_2.

Chapter 4

Internal-motional state coupling

The ions are typically coupled through their shared motional modes. Thus through this motional bus, the electronic states (spins) can be effectively coupled through an internal-motional state coupling. One method to realize this coupling is to use the position dependence of the laser or microwave fields, so that the motional information is imprinted to the spin transitions. In this chapter, we will start with describing the quantization of motional states. Then we will describe the laser induced spin-motion interaction, with various aspects that are important to the experiments in this thesis.

4.1 Quantization of motional modes

We continue the description in Sec. 2.1, and provide a quantum mechanical treatment for the axial motional modes. Here we ignore the micromotion. For one ion, from Eq. 2.2, the axial component of the motional Hamiltonian is

$$\begin{aligned} H_m &= \frac{p^2}{2m} + q\Phi_s && (4.1)\\ &= \frac{p^2}{2m} + \frac{1}{2}m\omega_z^2 z^2 && (4.2)\\ &= \hbar\omega_z(a^\dagger a + \frac{1}{2}), && (4.3)\end{aligned}$$

where m is the ion mass, and the last step results from a transformation of $z = \sqrt{\frac{\hbar}{2m\omega_z}}(a + a^\dagger)$, $p = i\sqrt{\frac{m\omega_z\hbar}{2}}(a^\dagger - a)$, and the commutation relation $[a, a^\dagger] = 1$. The eigenstates of H_m are labeled as "Fock" states $|n\rangle$ [100], with $n \geqslant 0$ and $a^\dagger a|n\rangle = n|n\rangle$, and properties $a|n\rangle = \sqrt{n}|n-1\rangle$ and $a^\dagger|n\rangle = \sqrt{n+1}|n+1\rangle$.

With more than one ions in the same well, the above process is modified to include the Coulomb repulsion between the ions. For two ions of charge q and masses m_1 and m_2, the potential energy is

$$V = \frac{1}{2}m_1\omega_{z,1}^2 z_1^2 + \frac{1}{2}m_2\omega_{z,2}^2 z_2^2 + \frac{q^2}{4\pi\epsilon_0|z1 - z2|}, \tag{4.4}$$

where ϵ_0 is the permittivity, z_i and $\omega_{z,i}$ are the position and single-ion motional frequency for the i^{th} ion. Since the trapping potential is independent of the ion mass, quantity $V_0 = m_i\omega_{z,i}^2$ is a constant. Assuming $z_1 > z_2$, and solving $\frac{\partial V}{\partial z_{1,2}} = 0$, we can obtain the equilibrium position of the ions $\{z_1^0, z_2^0\}$. For two ions, these equations can be solved analytically, $z_1^0 = -z_2^0 = \left(\frac{q^2}{16\pi\epsilon_0 V_0}\right)^{\frac{1}{3}}$. For a typical $\omega_z = 2\pi \times 3.58$ MHz, for two ${}^9\mathrm{Be}^+$ ions, we find the equilibrium positions $z_1^0 = -z_2^0 \approx 1.97\mu m$. With $z_i = z_i^0 + z_i'$, $i = 1, 2$, the potential energy can be expanded to the second order in z_i' as

$$V \approx V_0((z_1')^2 + (z_2')^2 - z_1'z_2'), \tag{4.5}$$

where we ignore the constant term. Combined with the kinetic energy, the Hamiltonian is thus

$$H \approx \frac{P_1^2}{2m_1} + \frac{P_2^2}{2m_2} + V_0((z_1')^2 + (z_2')^2 - z_1'z_2'). \tag{4.6}$$

Similar to the one ion case, we need to diagonalize the Hamiltonian. Here we apply a transformation

$$z_1' = \cos\theta\sqrt{\frac{\hbar}{2m_1\omega_1}}(a_1 + a_1^\dagger) - \sin\theta\sqrt{\frac{\hbar}{2m_1\omega_2}}(a_2 + a_2^\dagger) \tag{4.7}$$

$$z_2' = \cos\theta\sqrt{\frac{\hbar}{2m_2\omega_2}}(a_2 + a_2^\dagger) + \sin\theta\sqrt{\frac{\hbar}{2m_2\omega_1}}(a_1 + a_1^\dagger) \tag{4.8}$$

$$P_1 = \cos\theta\sqrt{\frac{\hbar m_1\omega_1}{2}}(ia_1^\dagger - ia_1) - \sin\theta\sqrt{\frac{\hbar m_1\omega_2}{2}}(ia_2^\dagger - ia_2) \tag{4.9}$$

$$P_2 = \cos\theta\sqrt{\frac{\hbar m_2\omega_2}{2}}(ia_2^\dagger - ia_2) + \sin\theta\sqrt{\frac{\hbar m_2\omega_1}{2}}(ia_1^\dagger - ia_1), \tag{4.10}$$

where a_i is the annihilation operators for normal motional mode $i = 1, 2$, θ satisfies $\cos 2\theta =$

$\frac{m_1-m_2}{\sqrt{m_1^2+m_2^2-m_1m_2}}$, and

$$\omega_1^2 = \frac{3V_0}{m_1+m_2+\sqrt{m_1^2+m_2^2-m_1m_2}} \tag{4.11}$$

$$\omega_2^2 = \frac{3V_0}{m_1+m_2-\sqrt{m_1^2+m_2^2-m_1m_2}}. \tag{4.12}$$

Thus the Hamiltonian is diagonalized such that

$$H = \hbar\omega_1(a_1^\dagger a_1 + \frac{1}{2}) + \hbar\omega_2(a_2^\dagger a_2 + \frac{1}{2}). \tag{4.13}$$

The eigenmodes expressed interms of the two ions motion is thus

$$a_1 + a_1^\dagger = \sqrt{\frac{2\omega_1}{\hbar}}(\cos\theta\sqrt{m_1}z_1' + \sin\theta\sqrt{m_2}z_2'), \tag{4.14}$$

$$a_2 + a_2^\dagger = \sqrt{\frac{2\omega_2}{\hbar}}(\cos\theta\sqrt{m_2}z_2' - \sin\theta\sqrt{m_1}z_1'), \tag{4.15}$$

we can see the eigenmodes contains motion of both ions, and the component of the two ion's motion in mode 1 and 2 is represented by unit vectors $\{\cos\theta, \sin\theta\}$ and $\{-\sin\theta, \cos\theta\}$ respectively, the mode amplitudes. They combined with the $\sqrt{\frac{2\omega_j}{\hbar}}\sqrt{m_i}$ factor fully express the j^{th} eigenmode in terms of the motion of the i^{th} ion. For the two ions with same sign of mode amplitudes, they are oscillating with the same phase; this mode is designated the common (COM) mode. The other mode with opposite signs of amplitudes is called the stretch mode. The motional mode analysis above can be extended to more ions numerically. In Table 4.1, we show the mode amplitudes and mode frequencies for the case of one, two and three $^9\text{Be}^+$ ions, a $^9\text{Be}^+ - {}^{24}\text{Mg}^+$ ion pair and a $^9\text{Be}^+ - {}^{24}\text{Mg}^+ - {}^{24}\text{Mg}^+ - {}^9\text{Be}^+$ ion chain, in the same potential well.

4.2 Resolved sideband coupling

In chapter 3 we describe laser beams driving transitions of ions' electronic states. Here we will start with describing laser driven electric dipole transitions for a stationary ion. We then include the ion motion. Intuitively, in the ion's frame, the laser beam frequencies are modulated by the ions' motion through the Doppler effect, thus creating laser "sidebands" in the frequency domain. These sidebands are spaced by the motional frequency, and the amplitudes are proportionally to the Bessel

config	ion chain	mode	frequency ($2\pi\times$MHz)	mode amplitudes
case 1	^{9}Be$^+$	COM	3.58	1
	^{9}Be$^+$ – ^{9}Be$^+$	COM	3.58	$\{\frac{1}{\sqrt{2}}, \frac{1}{\sqrt{2}}\}$
	^{9}Be$^+$ – ^{9}Be$^+$	stretch	6.20	$\{\frac{1}{\sqrt{2}}, -\frac{1}{\sqrt{2}}\}$
	^{9}Be$^+$ – ^{9}Be$^+$ – ^{9}Be$^+$	COM	3.58	$\{\frac{1}{\sqrt{3}}, \frac{1}{\sqrt{3}}, \frac{1}{\sqrt{3}}\}$
	^{9}Be$^+$ – ^{9}Be$^+$ – ^{9}Be$^+$	stretch	6.20	$\{\frac{1}{\sqrt{2}}, 0, -\frac{1}{\sqrt{2}}\}$
	^{9}Be$^+$ – ^{9}Be$^+$ – ^{9}Be$^+$	"Egyptian"	8.62	$\{\frac{1}{\sqrt{6}}, -\frac{2}{\sqrt{6}}, \frac{1}{\sqrt{6}}\}$
case 2	^{9}Be$^+$	COM	2.97	1
	^{9}Be$^+$ – ^{24}Mg$^+$	COM	2.10	{0.378,0.926}
	^{9}Be$^+$ – ^{24}Mg$^+$	stretch	4.46	{0.926,-0.378}
case 3	^{9}Be$^+$	COM	2.71	1
	^{9}Be$^+$ – ^{24}Mg$^+$ – ^{24}Mg$^+$ – ^{9}Be$^+$	COM	1.96	{0.322,0.629,0.629,0.322}
	^{9}Be$^+$ – ^{24}Mg$^+$ – ^{24}Mg$^+$ – ^{9}Be$^+$	stretch	4.12	{0.466,0.532,-0.532,-0.466}
	^{9}Be$^+$ – ^{24}Mg$^+$ – ^{24}Mg$^+$ – ^{9}Be$^+$	"Egyptian"	5.53	{0.629,-0.322,-0.322,0.629}
	^{9}Be$^+$ – ^{24}Mg$^+$ – ^{24}Mg$^+$ – ^{9}Be$^+$	"FUNK"	5.78	{0.532,-0.466,0.466,-0.532}

Table 4.1: Normal motional modes for various ion chain configurations, with the same external potential well for each case. The mode amplitudes are shown consistent with the ion order. For the ^{9}Be$^+$–^{24}Mg$^+$ pair, due to the mass imbalance, the COM mode is dominated by motion of the ^{24}Mg$^+$ ion, while the stretch mode is dominated by the ^{9}Be$^+$ ion. This reduces the sympathetic cooling efficiency of mix-species chains for the modes which the coolant ion has small mode amplitudes. The mode information shown in this table will be useful for the experiments described in the following chapters.

function $J_n(\eta)$ classically, where n denotes the n^{th} order sideband, and η is the modulation index equals to a product of the ion motion amplitude and the laser $\boldsymbol{k}$-vector along the motion direction, which is also known as Lamb-Dicke parameter detailed below. Thus with proper configurations as detailed below, a laser detuned by the motional frequency can drive an electronic transition at the same time excite/de-excite the ion's motion, known as a sideband transition. This transition will be used to induce spin-motion coupling[1] .

---

[1] There are other ways to implement internal-motional state coupling, such as applying a strong static field gradient [86], or applying a microwave field gradient. [101]

4.2.1 Electric dipole transition for a free ion

Here we treat the laser beam as a classical oscillating electric field and ignore the magnetic components, since the frequencies of relevant magnetic dipole transitions are far off-resonance from typical laser frequencies. In a one dimensional model, the laser field can be modeled as $\mathbf{E}(z,t) = \mathbf{E}_0 \cos(kz - \omega_L t + \phi)$, where $\mathbf{E}_0 = \hat{\epsilon} E_0$ contains the field polarization $\hat{\epsilon}$ and amplitude E_0, $k = \frac{2\pi}{\lambda}$ is the wavenumber of the laser, λ is the wavelength of the laser, z is the ion position relative to equilibrium, ω_L is the laser frequency and ϕ is the optical phase. For $^9\mathrm{Be}^+$ in a magnetic field as in chapter 3, to drive a transition from the $2s\ ^2S_{\frac{1}{2}}$ to $2p\ ^2P_{\frac{1}{2}}$ state, the laser frequency needs to be near resonant with the transition frequency ω_0. The Hamiltonian is thus

$$H = H_0 + V \tag{4.16}$$

$$V = -\boldsymbol{\mu}_\mathrm{d} \cdot \mathbf{E}(z,t), \tag{4.17}$$

where H_0 represents the electronic energy levels, $\boldsymbol{\mu}_\mathrm{d} = -|e|\mathbf{r}$ is the electric dipole operator for the transition, e is the electron charge, and $\mathbf{r}$ is the operator representing position from the nuclei to the electron. To express H as a matrix in the hyperfine manifold, we typically only need to obtain the matrix elements between the hyperfine levels $|i\rangle$ and $|e\rangle$ that are relevant to the transition. Thus

$$H_0 = \hbar\omega_i |i\rangle\langle i| + \hbar\omega_e |e\rangle\langle e| \tag{4.18}$$

$$V = 2\hbar(\Omega_{ie}|i\rangle\langle e| + \Omega_{ei}|e\rangle\langle i|)\cos(kz - \omega_L t + \phi), \tag{4.19}$$

where $\hbar\omega_{i,e}$ is the energy of the state $|i\rangle$ and $|e\rangle$, ω_L is the laser frequency, and $\Omega_{ie} = \Omega_{ei}^* = -\frac{1}{\hbar}|e|E_0\langle i|\mathbf{r}\cdot\hat{\epsilon}|e\rangle/2$ can be calculated by integrating with the state $|i\rangle$ and $|e\rangle$ expressed with wavefunctions in radial and angular coordinates. The angular coordinates for $^9\mathrm{Be}^+$ states can be obtained from description in Table 3.2 and Table 3.3.

To obtain the dynamics, it is useful to transform Eq. 4.19 to an interaction picture for the internal states. For the Hamiltonian $H = H_0 + V$, in the interaction picture, $H_\mathrm{int} = e^{iH_0 t/\hbar} V e^{-iH_0 t/\hbar}$, corresponding to viewing the wavefunction $|\Psi\rangle$ in a frame with transformation $|\Psi'\rangle = e^{iH_0 t/\hbar}|\Psi\rangle$.

Here we have

$$H_{\text{int}} = e^{iH_0t/\hbar} V e^{-iH_0t/\hbar} \tag{4.20}$$

$$= 2(\Omega_{ie}|i\rangle\langle e|e^{i(\omega_i-\omega_e)t} + \Omega_{ei}|e\rangle\langle i|e^{i(\omega_e-\omega_i)t})\cos(kz-\omega_L t+\phi). \tag{4.21}$$

By rewriting $\cos(kz-\omega_L t+\phi) = \frac{1}{2}(e^{i(kz-\omega_L t+\phi)} + e^{-i(kz-\omega_L t+\phi)})$, the time dependent part contains two frequencies, $|\omega_i - \omega_e \pm \omega_L|$. If we assume $|i\rangle$ and $|e\rangle$ are the ground/excited states and we set $\Delta \equiv \omega_L - (\omega_e - \omega_i)$, with $\Delta \ll (\omega_e - \omega_i)$, thus one of the frequency difference is Δ but the other frequency is very high and is approximately twice the frequency difference between the ground/excited states. In this case we can make the rotating wave approximation (RWA) to neglect the high frequency component. Thus the Hamiltonian in the interaction picture is

$$H_{\text{int}} = \hbar\Omega_{ie}|i\rangle\langle e|e^{i(\Delta t-kz-\phi)} + H.C., \tag{4.22}$$

where $H.C.$ denotes Hermitian conjugate.

4.2.2 Raman transition

To drive transitions optically between two hyperfine states, we need a Λ configuration, depicted in Fig. 3.1 and Fig. 4.1. This Λ involves two dipole transitions with the close detuning from the same excited state. In this case, the Hamiltonian in the interaction picture is

$$H_{\text{int},\Lambda} = \hbar\Omega_{ie}|i\rangle\langle e|e^{i(\Delta t-kz-\phi)} + \hbar\Omega_{me}|m\rangle\langle e|e^{i(\Delta' t-k'z-\phi')} + H.C., \tag{4.23}$$

where the ground hyperfine states are denoted $|i\rangle$ and $|m\rangle$, and Δ and Δ' denote the detunings of the lasers driving the $|i\rangle \rightarrow |e\rangle$ and $|m\rangle \rightarrow |e\rangle$ transitions. With Δ much larger than Ω_{ie} and Ω_{me}, a second order perturbation theory is performed [102] and we obtain

$$H_{\text{eff}} = \hbar\frac{|\Omega_{ie}|^2}{\Delta}|i\rangle\langle i| + \hbar\frac{|\Omega_{me}|^2}{\Delta'}|m\rangle\langle m| + \hbar(\frac{\Omega_{ie}\Omega_{me}^*}{\Delta}|i\rangle\langle m|e^{i(\nu t+(k'-k)z+\phi'-\phi)} + H.C.), \tag{4.24}$$

assuming the frequency difference of the laser beams $\nu = \Delta - \Delta'$ is such that $|\nu| \ll |\Delta|$. The first two terms of this effective Hamiltonian represent the Stark shifts of the ground states by the two laser beams, and can be nulled by setting the difference frequency of the laser beams to be $\nu' = \nu - (\frac{|\Omega_{me}|^2}{\Delta'} - \frac{|\Omega_{me}|^2}{\Delta})$. The third terms represent an effective coupling between the ground states, with Rabi rate $\Omega_0 = |\frac{\Omega_{ie}\Omega^*_{me}}{\Delta}|$. With the Stark shift nulled, this drives a resonant two-photon stimulated-Raman transition between ground states $|i\rangle$ and $|m\rangle$.

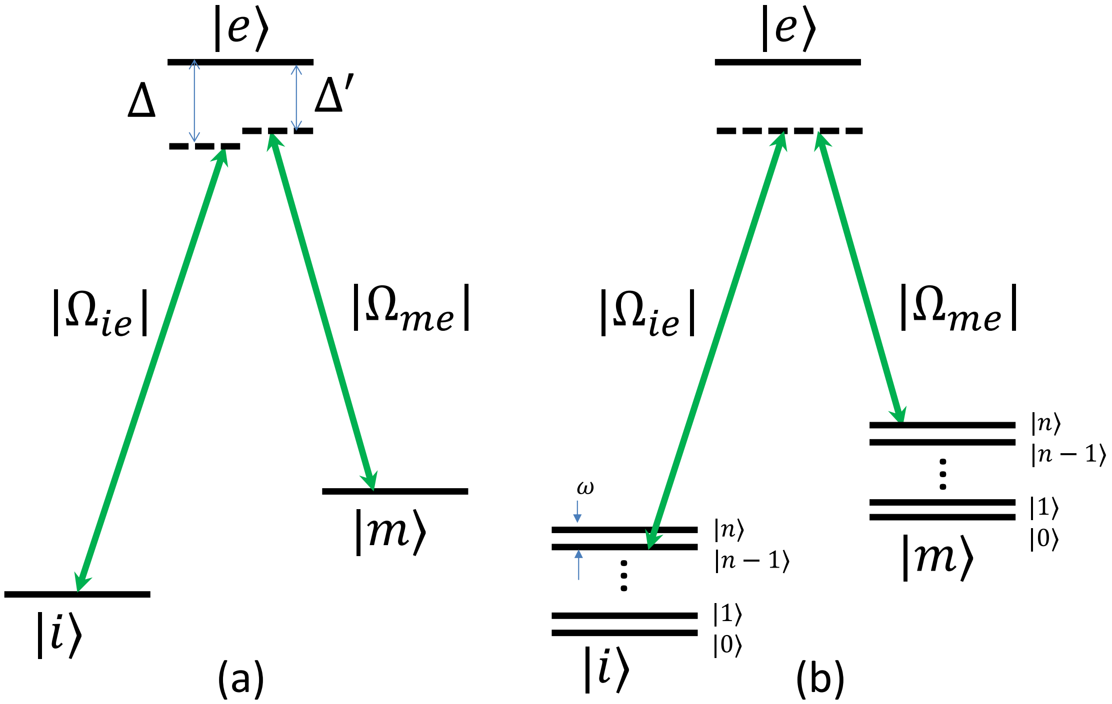

Figure 4.1: (a) A simplified Λ configuration of Raman transition between internal states $|i\rangle$ and $|m\rangle$. (b) a Raman sideband transition of $|m, n\rangle \rightarrow |i, n-1\rangle$.

The major draw back of using a Raman transition is the off-resonant couplings from the ground states to the excited states which are subject to decay; this can destroy coherence and may also cause incoherent hyperfine state changes through spontaneous emission [46]. With the excited state decay rate Γ, the spontaneous emission rate $\gamma_{SE} \propto \Gamma\frac{|\Omega_{ie,je}|^2}{\Delta^2}$. Since the Raman transition Rabi rate scales as $\frac{1}{\Delta}$, we can decrease γ_{SE} relative to the Rabi rate by increasing Δ, at the cost of proportionally increasing the laser intensities to maintain the Raman transition Rabi rate.

4.2.3 Raman sideband coupling

With $\Delta k = k' - k \neq 0$, the two laser beams create a phase gradient in space, and thus the ion motion needs to be taken into account. With one ion, the motional Hamiltonian is $H_s = \hbar\omega a^\dagger a$, neglecting the constant term. From Sec. 4.1, we have $z = z_0(a+a^\dagger)+z^0$, where z^0 is the equilibrium position of the ion, z_0 is the spread of the wavepacket, and a is the annihilation operator. We define the quantity $\Delta k z_0 \equiv \eta$, the Lamb-Dicke parameter. For $\eta \ll 1$, we can expand H_{eff} to the orders of η, and in the interaction picture of H_s, H_{eff} becomes

$$H_{\text{eff}} = \hbar\Omega_0|i\rangle\langle m|e^{i(\nu' t+\phi'-\phi+\Delta k z^0)}(1 + i\eta(e^{-i\omega t}a + e^{i\omega t}a^\dagger) + ...) + H.C.. \tag{4.25}$$

The interesting case is for $\nu' - \omega \equiv \delta \ll 1$, where the laser beam frequency difference is offset from the hyperfine state energy difference by a motional frequency, called the first sideband of the hyperfine transition[2] . In this case the Raman transition is de-exciting the motion while driving the transition from $|m\rangle$ to $|i\rangle$[3] . From Eq. 4.25, we need to include all terms in the expansion of $e^{i\eta(a+a')}$ that have time dependence equal to $e^{-i\omega t}$ [22, 103, 104]. We have

$$H_{\text{eff}} = \hbar\sum_n \Omega_{n-1,n}|i, n-1\rangle\langle m, n|e^{i(\phi'-\phi+\Delta k z^0)} + H.C., \tag{4.26}$$

where $|m, n\rangle$ includes the motional Fock state $|n\rangle$,
$\Omega_{n-1,n} \equiv \Omega_0|\langle n-1|e^{i\eta(a+a^\dagger)}|n\rangle| = \Omega exp(-\eta^2/2)\eta L^1_{n-1}(\eta^2)/\sqrt{n}$, and
$L^\alpha_n(X) = \sum_{m=0}^{n}(-1)^m \begin{pmatrix} n+\alpha \\ n-m \end{pmatrix} \frac{X^m}{m!}$ is the generalized Laguerre polynomial. To the first order of η, we can still approximate the Hamiltonian as the Jaynes-Cummings type

$$H_{\text{eff}} = \hbar\Omega|i\rangle\langle m|a\ e^{i(\delta t+\phi'-\phi+\Delta k z^0)} + H.C., \tag{4.27}$$

where $\Omega = \Omega_0\eta e^{-\eta^2/2}$. This Hamiltonian serves as a starting point to understand the couplings between the spin and motion in this thesis. With this coupling, transition $|m, n\rangle \leftrightarrow |i, n-1\rangle$ is driven. This coupling can be used to provide cooling with hyperfine state repumping of $|i\rangle \to |m\rangle$,

---

[2] The analysis for $\nu' + \omega \equiv \delta \ll 1$ is similar

[3] motional excitation would happen for the opposite case driving from $|i\rangle$ to $|m\rangle$

to generate a repeated cooling cycle $|m,n\rangle \leftrightarrow |i,n-1\rangle \rightarrow |m,n-1\rangle \rightarrow ...|m,0\rangle$. This is the case of resolved Raman sideband cooling, where dissipation of the internal states is transferred to motion with the internal-motional state coupling. The cooling can be applied in a continuous manner, where the sideband coupling and repumping are applied simultaneously. With repumping rate $\gamma \gg \Omega$, the effective cooling rate is proportional to Ω^2/γ. It can also be applied in a stepwise way, where sideband and repumping pulses are alternatively applied. The process starts from repumping to the $|m\rangle$ state, then ideally, every step contains a sideband π transition from $|m,n\rangle \rightarrow |i,n-1\rangle$ followed by a repump pulse. Assuming the ion is at Fock state $|N\rangle$ initially, the i^{th} step sideband pulse duration corresponds to the Rabi rate for Fock state $|N-i+1\rangle$. Typically, N is chosen to be large to cover enough Fock states after Doppler cooling [105].

4.2.4 Raman sideband coupling for two ions: resonant case

From the previous section, the sideband Hamiltonian for two ions can be written

$$H_{\text{SB}} = \hbar\Omega(|i\rangle_1\langle m|e^{i\Delta k z_1^0} + |i\rangle_2\langle m|e^{i\Delta k z_2^0})a\ e^{i(\delta t+\phi'-\phi)} + H.C., \tag{4.28}$$

where we assume equal Rabi rates on the two ions, labeled as ion $i = 1, 2$, and z_i^0 represents the equilibrium position of ion i. From now on we label $|i\rangle \equiv |\downarrow\rangle$ and $|m\rangle \equiv |\uparrow\rangle$. By choosing the location of ion 1 as the origin, and defining $\Delta z = z_2^0 - z_1^0$, we have

$$H_{\text{SB}} = \hbar\Omega(\sigma_1^- + \sigma_2^- e^{i(\Delta k \Delta z)})a\ e^{i(\delta t+\phi'-\phi)} + H.C., \tag{4.29}$$

where $\sigma^- = |\downarrow\rangle\langle\uparrow|$ is the Pauli lowering operator. By controlling the separation Δz of the two ions, the relative phase between the σ^- operators can be controlled. This corresponds to a relative phase added to the states and is important when creating different entangled states, such as $|T\rangle = \frac{1}{\sqrt{2}}(|\uparrow\downarrow\rangle + |\downarrow\uparrow\rangle)$ versus $|S\rangle = \frac{1}{\sqrt{2}}(|\uparrow\downarrow\rangle - |\downarrow\uparrow\rangle)$. To analyze the eigensystem of H_{SB}, we first choosing $\Delta k \Delta z = 2M\pi$, where M is an integer number. And we set $\delta = 0$ and $\phi' - \phi = 0$. Thus the Hamiltonian is simplified as

$$H_{\text{SB}} = \hbar\Omega(\sigma_1^- + \sigma_2^-)a + H.C., \tag{4.30}$$

eigenenergy/$\hbar$	eigenstate
0	$\vert\uparrow\uparrow, 0\rangle$
0	$\vert S, n\rangle$
0	$\vert\Psi_0, n\rangle = \frac{1}{\sqrt{2n+3}}(\sqrt{n+2}\vert\downarrow\downarrow, n\rangle - \sqrt{n+1}\vert\uparrow\uparrow, n+2\rangle)$
$\pm\sqrt{2}\Omega$	$\frac{1}{\sqrt{2}}(\vert T, 0\rangle \pm \vert\uparrow\uparrow, 1\rangle)$
$\pm\sqrt{4n+2}\Omega$	$\vert\Psi_\pm, n\rangle = \frac{1}{\sqrt{4n+2}}(\sqrt{n+1}\vert\uparrow\uparrow, n+1\rangle \pm \sqrt{2n+1}\vert T, n\rangle + \sqrt{n}\vert\downarrow\downarrow, n-1\rangle)$.

The eigenenergy and eigenstates are the following:

Here we point out some properties of this Hamiltonian.

1. The eigenenergies of states $|\uparrow\uparrow, 0\rangle$, $|S, n\rangle$ and $|\Psi_0, n\rangle$ are 0 since they do not couple to H_{SB}, and are thus "dark" states.

2. The state $|\downarrow\downarrow, 0\rangle$ can be expressed in a superposition of eigenstates as $|\downarrow\downarrow, 0\rangle = \frac{1}{\sqrt{6}}(|\Psi_+, 1\rangle + |\Psi_-, 1\rangle + 2|\Psi_0, 0\rangle$. Thus the evolution starting from this state is thus $|\downarrow\downarrow, 0\rangle \rightarrow \frac{1}{\sqrt{6}}(|\Psi_+, 1\rangle e^{-i\sqrt{6}\Omega t} + |\Psi_-, 1\rangle e^{i\sqrt{6}\Omega t} + 2|\Psi_0, n\rangle))$. The half period of the evolution is thus $t_\pi = \pi/(\sqrt{6}\Omega)$. The population of $|T\rangle$ is maximized to $\frac{1}{3}$ at $t = \frac{2M+1}{2}t_\pi$, where M is an integer, and the population of $|\uparrow\uparrow\rangle$ is maximized to $\frac{8}{9}$ at $t = (2M+1)t_\pi$, as shown in Fig. 4.2. Thus a resonant sideband alone is not sufficient to produce $|T\rangle$. This is due to the Fock state dependence of the coupling strengths.

3. The above analysis is relevant to the dissipative entanglement experiment in this thesis. For $\Delta k \Delta z = (2M+1)\pi$, the results are similar except for an exchange between $|T\rangle$ and $|S\rangle$. This sideband interaction is also important for the experiment of confined dynamics in this thesis.

4.2.5 Raman sideband coupling for two ions: detuned case

As described in previous section, for the resonant case, the $|\downarrow\downarrow, 0\rangle$ state contains the $|\Psi_0, 0\rangle$ dark state. For the confined dynamics described in this thesis in Chapter 7, the desired interaction would only have dark states of $|\uparrow\uparrow, 0\rangle$ and $|T, 0\rangle$. It turns out that the sieband interaction with $\delta \neq 0$ can realize this case. As we will see below, in a suitable frame the non zero detuning is

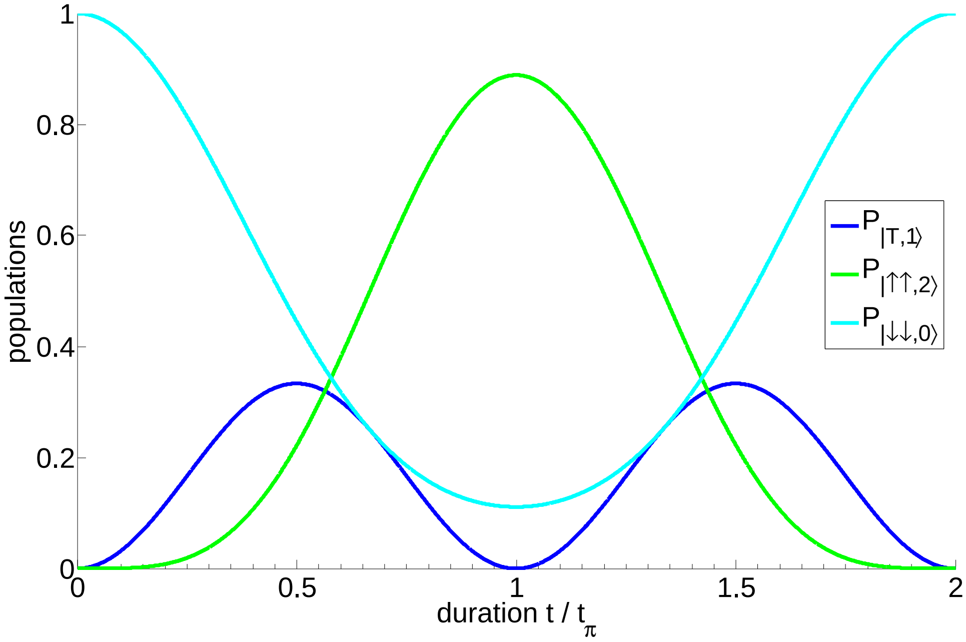

Figure 4.2: State evolution subject to the sideband Hamiltonian of Eq. 4.30, starting from state $|\downarrow\downarrow, 0\rangle$.

equivalent to introducing extra shifts on different Fock state, and thus $|\Psi_0, 0\rangle$ is dressed and energy shifted since it contains more than one Fock states. Here we provide detailed analysis for this case and find the optimal δ that gives the maximal energy shift of the $|\downarrow\downarrow, 0\rangle$ state from its unperturbed value.

To simplify the discussion we choose $\phi' - \phi = 0$ and $\Delta k \Delta z = (2M+1)\pi$. Thus the sideband Hamiltonian becomes

$$H_{\text{SB}} = \hbar\Omega(\sigma_1^- - \sigma_2^-)a\ e^{i\delta t} + H.C.. \tag{4.31}$$

To make the Hamiltonian time independent, we move to an interaction frame for the motion defined by $U = e^{i\delta a^\dagger a t}$, equivalent to a transformation of wavefunction $|\Psi'\rangle = U|\Psi\rangle$. The Hamiltonian in this frame is

$$H'_{\text{SB}} = -iU\partial_t(U^\dagger) + UH_{\text{SB}}U^\dagger \tag{4.32}$$

$$= -\hbar\delta a^\dagger a + (\hbar\Omega(\sigma_1^- - \sigma_2^-)a + H.C.). \tag{4.33}$$

To analyse the eigenenergies and eigenstates of this Hamiltonian, we express H_{SB} in terms of the subspace $\{|{\downarrow\downarrow}, 0\rangle, |S, 1\rangle, |{\uparrow\uparrow}, 2\rangle\}$. We have

$$H'_{\mathrm{SB}} = \begin{pmatrix} 0 & \sqrt{2}\Omega & 0 \\ \sqrt{2}\Omega & -\delta & -2\Omega \\ 0 & -2\Omega & -2\delta \end{pmatrix}. \tag{4.34}$$

The eigenvalues versus the detuning are shown in Fig. 4.3. All three eigenstates have components of the $|{\downarrow\downarrow}, 0\rangle$ state.

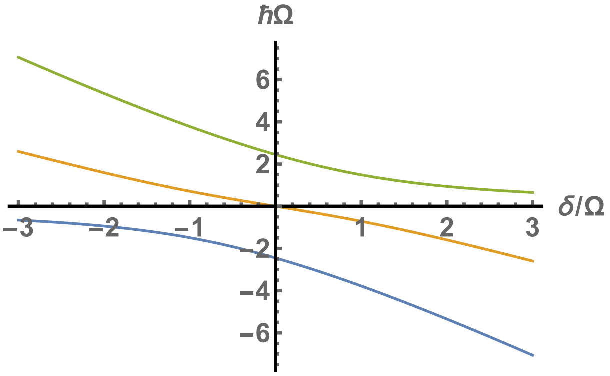

Figure 4.3: Eigenvalues of the detuned sideband.

As described in Chapter 7, we will want to find δ values, where all eigenvalues are shifted maximally from zero. From Fig. 4.3, this condition is fulfilled when two of the eigenenergies are equal but opposite sign with $\delta \neq 0$. Imposing this condition, we find $\delta = \pm\sqrt{\frac{7}{3}}\Omega$, and for the positive case the eigenenergies and eigenstates are

eigenenergy/$\hbar$	eigenstate
$\lambda_1 = \sqrt{\frac{4}{3}}\Omega,$	$|\Psi_1\rangle = -\sqrt{\frac{3}{118}(19+\sqrt{7})}|{\downarrow\downarrow}, 0\rangle - \sqrt{\frac{1}{59}(19+\sqrt{7})}|S, 1\rangle + \sqrt{\frac{3}{23+5\sqrt{7}}}|{\uparrow\uparrow}, 2\rangle$
$\lambda_2 = -\sqrt{\frac{4}{3}}\Omega,$	$|\Psi_2\rangle = \sqrt{\frac{3}{118}(19-\sqrt{7})}|{\downarrow\downarrow}, 0\rangle - \sqrt{\frac{1}{59}(19-\sqrt{7})}|S, 1\rangle + \sqrt{\frac{1}{118}(23+5\sqrt{7})}|{\uparrow\uparrow}, 2\rangle$
$\lambda_3 = -\sqrt{21}\Omega,$	$|\Psi_3\rangle = -\sqrt{\frac{2}{59}}|{\downarrow\downarrow}, 0\rangle + \sqrt{\frac{21}{59}}|S, 1\rangle + \frac{6}{\sqrt{59}}|{\uparrow\uparrow}, 2\rangle$

Chapter 5

Sympathetic electromagnetically-induced-transparency(EIT) laser cooling

To achieve high fidelity multi-qubit operations with trapped ions, the qubit ions should be laser cooled as close as possible to the ground state of motion. At the same time, the laser beams that provide the cooling should not perturb information stored in the qubits. To achieve this, one needs to trap ions specifically for cooling, the "refrigerants", in the same trap as the qubit ions. The regrigerant ions can be same species as the qubit ions and be cooled with laser beams focused strongly enough to not perturb the qubit ions, but in practice this isolation is difficult to achieve. An alternative procedure is to make the refrigerant ions to be a different species that has resonant wavelengths substantially different from the resonant wavelengths of qubit ions. This process, known as sympathetic cooling [44], can be implemented with Raman sideband cooling [106]. An alternative method is to use electromagnetically-induced-transparency (EIT) laser cooling. We will see that this method significantly reduces the cooling duration and the required laser power compared with sideband cooling, by applying near-detuned lasers to induce the EIT effect.

In this chapter, we describe experiments and simulations applying EIT laser cooling on the motional modes of a linear ion chain [78]. We first describe the general aspects of sympathetic laser cooling of trapped ions and the conventional method of Raman sideband cooling. Second, we discuss principles of EIT laser cooling, and experimental implementations on sympathetic cooling $^{9}\mathrm{Be}^{+}$ ions by $^{24}\mathrm{Mg}^{+}$ ions in $^{9}\mathrm{Be}^{+}$ - $^{24}\mathrm{Mg}^{+}$ ion pairs and $^{9}\mathrm{Be}^{+}$ - $^{24}\mathrm{Mg}^{+}$ - $^{24}\mathrm{Mg}^{+}$ - $^{9}\mathrm{Be}^{+}$ ion chains. We then compare cooling speeds and final temperatures of Raman sideband cooling and EIT laser cooling in our experiments. We achieve approximately an order-of-magnitude reduction in the duration required to cool the motional modes to near the ground state; we also achieve approximately two orders-of-magnitude reduction in the required laser beam intensity, compared to previous implementations of conventional Raman sideband cooling. Finally, we discuss further aspects of cooling ^{24}Mg^{+} ions to sympathetically cool qubit ions of different mass, and possible improvements on future EIT-cooling experiments that use ^{24}Mg^{+} ions.

5.1 General description of sympathetic laser cooling

One proposal for building a quantum information processor is to use trapped, laser-cooled ions [17, 47, 107]. The internal states of the ions serve as individual qubits that can be manipulated by laser beams or microwave radiation. The Coulomb coupling between ions establishes normal modes of motion; sideband transitions involving both the qubit states and motional modes enable entangling-gate operations between multiple qubits. For high-fidelity deterministic entangling gates, the extent of the motion of the relevant modes should be in the Lamb-Dicke regime [107] where the amplitude of the ions' motion from equilibrium is much less than the effective wavelength of the coupling radiation[1] . Thus for most experiments, the motion needs be cooled to near the quantum-mechanical ground state, which has typically been achieved with sideband laser cooling [39, 107, 108].

Ion motion can be excited by ambient noisy electric fields [22]. Therefore, a method for recooling the ions is needed for implementation of lengthy quantum algorithms. One recooling strategy is to trap the qubit ions together with "refrigerant" ions. With Coulomb coupling between these ions, the qubits in the cooling process can be "sympathetically" cooled without disturbing the internal states [2, 3, 22, 34, 74–76, 109]. Demonstrations of this technique in information processing have so far used stimulated sideband cooling [3, 34, 39, 74–76]. While effective, stimulated Raman sideband cooling can typically cool only one mode at a time because of the differences in mode frequencies and narrowness of the sideband transitions. Furthermore, the laser-beam intensities and detuning must be sufficiently large to avoid heating from spontaneous emission. In experiments

---

[1] Probabilistic schemes for entanglement do not require such strong confinement[37]

performed in a scalable configuration, the duration required for recooling has been an important limiting factor [42, 45, 75]. The larger recooling duration for multiple recooling steps can enhance errors due to qubit dephasing [73].

A technique that can mitigate these problems is electromagnetically induced transparency (EIT) laser cooling, described theoretically in [8, 9] and demonstrated on a single ion in [110–112]. For EIT cooling, the required laser beam intensities are relatively small, and the cooling bandwidth is large enough that multiple modes can be cooled simultaneously, which speeds up the overall cooling process for multiple motional modes. To demonstrate these features, we investigate EIT cooling of multiple modes of linear ion chains containing $^9\mathrm{Be}^+$ and $^{24}\mathrm{Mg}^+$ ions. EIT cooling is applied to the $^{24}\mathrm{Mg}^+$ ions and cools all modes along the axis of the chain to near the ground state. This process thereby sympathetically cooling the $^9\mathrm{Be}^+$ ions.

5.2 Theoretical description of sympathetic EIT cooling

5.2.1 EIT effect on a stationary ion

The complete theoretical description of EIT laser cooling is given in [8]. Consider the three-level Λ system comprised of the bare states $|g_1\rangle$, $|g_2\rangle$ and $|e\rangle$ shown in Fig. 5.1(a), where the excited state $|e\rangle$ has a rate γ to decay back to the ground state manifold $\{|g_1\rangle,\ |g_2\rangle\}$. For an ion at rest, laser beams with resonant Rabi rates Ω_1 and Ω_2 and equal detunings $\Delta_1 = \Delta_2 \equiv \Delta > 0$ dress the bare states such that the system relaxes to the "dark" steady state $|\psi_\mathrm{D}\rangle = (\Omega_2|g_1\rangle - \Omega_1|g_2\rangle)/\Omega$ with $\Omega \equiv \sqrt{\Omega_1^2 + \Omega_2^2}$. This results from the Λ system Hamiltonian in the rotating frame [8] $H_\mathrm{static} = H_0 + V_0$, where $H_0 = \hbar\Delta(|g_1\rangle\langle g_1| + |g_2\rangle\langle g_2|)$, and $V_0 = \frac{\hbar}{2}(\Omega_1|e\rangle\langle g_1| + \Omega_2|e\rangle\langle g_2|) + H.c.$ represents the laser induced interactions. With a basis transformation from $\{|g_1\rangle, |g_2\rangle\}$ to $\{|\psi_\mathrm{D}\rangle, |\psi_\mathrm{C}\rangle = (\Omega_1|g_1\rangle + \Omega_2|g_2\rangle)/\Omega\}$, we have $H_\mathrm{static} = -\hbar\Delta(|\psi_\mathrm{D}\rangle\langle\psi_\mathrm{D}| + |\psi_\mathrm{C}\rangle\langle\psi_\mathrm{C}|) + \frac{\hbar}{2}\Omega(|e\rangle\langle\psi_\mathrm{C}| + |\psi_\mathrm{C}\rangle\langle e|)$. We can see $|\psi_\mathrm{C}\rangle$ is coupled to the excited $|e\rangle$ state, while $|\psi_\mathrm{D}\rangle$ is not coupled and remains "dark". Thus applying the laser beams in the Λ configuration pumps the system into the "dark" state.

Additionally, H_{static} can be further diagonalized as

$$\begin{aligned} H_{\text{static}} =& \frac{\hbar}{2}(\Delta + \sqrt{\Delta^2+\Omega^2})|\psi_+\rangle\langle\psi_+| \\ &+ \frac{\hbar}{2}(\Delta - \sqrt{\Delta^2+\Omega^2})|\psi_-\rangle\langle\psi_-| \\ &+ \hbar\Delta|\psi_{\text{D}}\rangle\langle\psi_{\text{D}}|, \end{aligned} \tag{5.1}$$

where $|\psi_+\rangle = \cos\theta|e\rangle + \sin\theta|\psi_{\text{C}}\rangle$, $|\psi_-\rangle = \sin\theta|e\rangle - \cos\theta|\psi_{\text{C}}\rangle$, and $\tan\theta = \frac{\sqrt{\Delta^2+\Omega^2}+\Delta}{\Omega}$. This basis $\{|\psi_D\rangle, |\psi_\pm\rangle\}$ is called "EIT basis". Assuming $\Delta \gg \Omega$, $\sin\theta \approx 1 - \frac{\Omega^2}{8\Delta^2}$ and $\cos\theta \approx \frac{\Omega}{2\Delta}$. Thus $|\psi_-\rangle$ state is approximately given by the $|e\rangle$ state, while $|\psi_+\rangle$ has a component of $|e\rangle$ with amplitude on the order of $\frac{\Omega}{2\Delta}$ in population. Both $|\psi_\pm\rangle$ states contain an excited state amplitude and are subject to decay to the ground state. Thus if we added a weak laser beam that probes the system, it would create an absorption spectrum as depicted in Fig. 5.1(c), where the narrow/broad peak correspond to the transition driving $|\psi_{\text{D}}\rangle \to |\psi_\pm\rangle$, respectively. The frequency shift between the absorption null and the relatively narrow absorption peak on the right side of the spectrum is

$$\delta = (\sqrt{\Delta^2+\Omega^2} - \Delta)/2, \tag{5.2}$$

corresponding to the energy difference of $|\psi_{\text{D}}\rangle$ and $|\psi_+\rangle$ in Eq. 5.1.

5.2.2 EIT effect with a trapped ion in motion

If the difference in k-vectors for the two dressing beams has a component along the direction of a motional mode, excitations in ion's motion will prevent it from being in the dark state. As we will see below, the transition of $|\psi_{\text{D}}, n\rangle \to |\psi_+, n-1\rangle$ is driven, where $|n\rangle$ denotes the motional Fock state. $|\psi_+, n-1\rangle$ subsequently decays back to the ground state manifold and is quickly pumped to $|\psi_{\text{D}}, n-1\rangle$, neglecting photon recoil heating. Thus ideally an effective close cooling cycle of $|\psi_{\text{D}}, n\rangle \to |\psi_{\text{D}}, n-1\rangle$ is formed until the ground state is achieved. The final phonon occupation number $\bar{n}$ is limited by the off-resonant motional heating transition of $|\psi_{\text{D}}, n\rangle \to |\psi_-, n+1\rangle$. Here we provide more detailed analysis of the above process.

The Hamiltonian is $H = H_0 + H_{\text{mec}} + V$, where $H_{\text{mec}} = \hbar\omega\left(a^\dagger a + \frac{1}{2}\right)$, $a = \sum_n \sqrt{n}|n-1\rangle\langle n|$ is the annihilation operator or, ω is the motional frequency, and V is now modified from the stationary

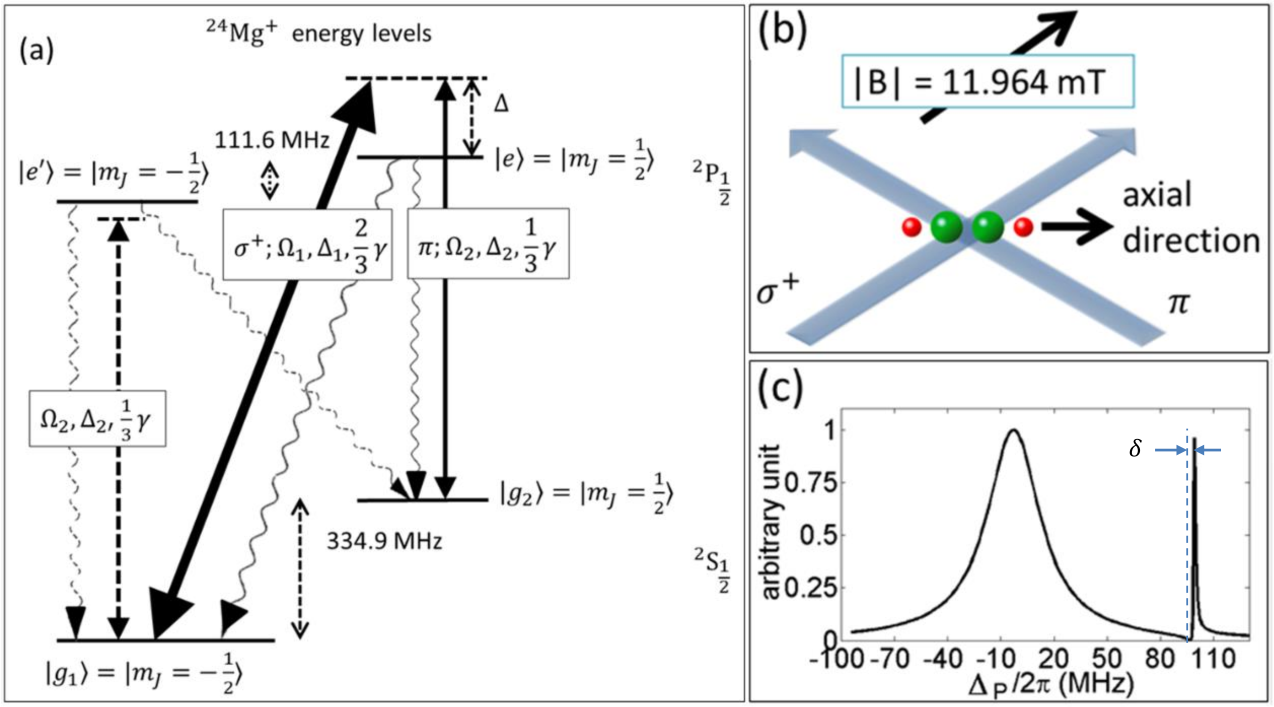

Figure 5.1: ^{24}Mg$^+$ energy levels, laser setup and a spectrum showing the EIT effect. (a) Relevant energy levels for ^{24}Mg$^+$, in an applied magnetic field of 11.964 mT. The three levels $|g_1\rangle$, $|g_2\rangle$ and $|e\rangle$ serve as a Λ system for EIT cooling. Laser beams with σ^+ and π polarizations couple the ground states to the excited state with Rabi rates Ω_1 and Ω_2 and common detuning Δ. Wavy lines show spontaneous emission from the excited state to the ground states and the excited-level decay rate is denoted by $\gamma \simeq 2\pi\times 41$ MHz. The fourth level $|e'\rangle$ can perturb the EIT cooling when the π polarized laser beam has frequency near the $|g_1\rangle$ to $|e'\rangle$ resonance. (b) Beam configuration and a depiction of the ^{9}Be$^+$–^{24}Mg$^+$ – ^{24} Mg$^+$–^{9}Be$^+$ ion, shown as balls from left to right. This figure is viewed in an angle from top view.(c) Simulation of the absorption spectrum of a stationary ion by a weak σ^+ probe beam for $\Delta = 2\pi\times 96.7$ MHz, $\Omega_1/2\pi = 30$ MHz, and $\Omega_2/2\pi = 12$ MHz. For simplicity, the fourth level $|e'\rangle$ is ignored. The probe detuning from the $|g_2\rangle$ to $|e\rangle$ resonance is denoted by $\Delta_{\rm P}$. This Fano-like profile contains a narrow and broad feature corresponding to dressed states $|\psi_+\rangle$ and $|\psi_-\rangle$ respectively [8], and the separation between the peak on the right side and the null is labeled as δ. When $\Delta_{\rm P} = \Delta$, absorption vanishes due to coherent population trapping.

V_0 to take account the motion

$$V = \frac{\hbar}{2}\left(\Omega_1 \mathrm{e}^{\mathrm{i}k_1 z\cos\phi_1}|e\rangle\langle g_1| + \Omega_2 \mathrm{e}^{\mathrm{i}k_2 z\cos\phi_2}|e\rangle\langle g_2| + H.c.\right), \tag{5.3}$$

where z is the position operator of the ion along the axial direction, $k_i\cos\phi_i$ is the projection of the laser beam $\mathbf{k}_i$ vector along the trap axis. We will assume the ion is in the Lamb-Dicke regime, so we expand the term $\mathrm{e}^{\mathrm{i}k_i z\cos\phi_i}$ up to the first order to show the physics of the cooling process.

Higher order expansions are considered in the full simulations. Thus we have $V \approx V_0 + zV_1$. The latter can be expressed in the basis of $\{|\psi_{\mathrm{D}}\rangle, |\psi_{\mathrm{C}}\rangle\}$,

$$V_1 = \frac{\mathrm{i}\hbar}{2} \sum_{j=1,2} k_i \cos\phi_j \Omega_j \left(|e\rangle\langle g_j| - |g_j\rangle\langle e|\right) \tag{5.4}$$

$$\begin{aligned} &= \frac{\mathrm{i}\hbar}{2}\Big(\frac{\Omega_1\Omega_2}{\Omega}\Delta k(|e\rangle\langle\psi_D| - |\psi_D\rangle\langle e|) \\ &+ \frac{\Omega_1^2 k_1\cos\phi_1 + \Omega_2^2 k_2 \cos\phi_2}{\Omega}(|e\rangle\langle\psi_C| - |\psi_C\rangle\langle e|)\Big), \end{aligned} \tag{5.5}$$

where the difference $\mathbf{k}$ vector $\Delta k = (k_1\cos\phi_1 - k_2\cos\phi_2)$, with $z = z_0(a + a^\dagger)$. When the EIT condition is fulfilled with $\Delta_1 = \Delta_2$, population in $|\psi_C\rangle$ would be pumped out quickly and relax to the dark state $|\psi_{\mathrm{D}}\rangle$, thus we will ignore the second term of V_1. Turning to EIT eigenbasis for the first term, we have

$$V_1 = \frac{\mathrm{i}\hbar}{2}\frac{\Omega_1\Omega_2}{\Omega}(\Delta k)\Big(\cos\theta|\psi_+\rangle\langle\psi_D| + \sin\theta|\psi_-\rangle\langle\psi_D| - H.c.\Big). \tag{5.6}$$

The total Hamiltonian can now be written as $H = H_0 + V_0 + H_{\mathrm{mec}} + zV_1$, and as shown above in (5.1), $H_0 + V_0$ is diagonal in the EIT eigenbasis. One can now transform zV_1 to the interaction picture $zV_{1,int} = e^{i(H_0+V_0+H_{\mathrm{mec}})t/\hbar} zV_1 e^{-i(H_0+V_0+H_{\mathrm{mec}})t/\hbar}$, where[2]

$$\begin{aligned} zV_{1,int} = \frac{\mathrm{i}\hbar}{2}\frac{\Omega_1\Omega_2}{\Omega}(z_0\Delta k)\sum_n(\sqrt{n}e^{-i\omega t}|n-1\rangle\langle n| + \sqrt{n}e^{i\omega t}|n\rangle\langle n-1|) \times \\ (e^{i\frac{-\Delta+\sqrt{\Delta^2+\Omega^2}}{2}t}\cos\theta|\psi_+\rangle\langle\psi_D| + e^{i\frac{-\Delta-\sqrt{\Delta^2+\Omega^2}}{2}t}\sin\theta|\psi_-\rangle\langle\psi_D| - H.c.). \end{aligned} \tag{5.7}$$

Here Δ is defined to be positive for blue detuned laser in contrast with [8]. As defined above, the Stark shift $\delta = \frac{-\Delta+\sqrt{\Delta^2+\Omega^2}}{2}$. By imposing the condition $\delta = \omega$ and applying the rotating wave approximation(RWA), V_1 will drive the transition from $|\psi_D\rangle|n\rangle$ to $|\psi_+\rangle|n-1\rangle$. [3] Combining this coherent transition with the EIT dark state re-establishing process, the cooling cycle is complete. With $\frac{-\Delta+\sqrt{\Delta^2+\Omega^2}}{2} = \omega$, we have $\Omega^2 = 4\omega(\omega+\Delta)$, which can be called the EIT cooling condition[4] , consistent with [8]. Intuitively, this condition corresponds to match the energy shift δ in Fig. 5.1(c)

---

[2] Detailed derivation is in the appendix.

[3] For a red detuned $\Delta < 0$, from Eq. 5.7 the transition $|\psi_D\rangle|n\rangle$ to $|\psi_-\rangle|n+1\rangle$ is driven with motion adding. Thus cooling can only occur for blue detuned laser beam configurations. This is different from the requirements of Doppler cooling.

[4] The sign of Δ is changed between this thesis and [8]

with the motional frequency ω. We note that the width of the right-hand peak can be made broad enough[5] that the condition for cooling is met for multiple modes for the same value of δ. This may facilitate experiments involving many ions such as simulations where the mode frequencies have a relatively narrow distribution [113–116].

5.3 Experiment sympathetic EIT laser cooling

We trap ^{9}Be$^+$ and ^{24}Mg$^+$ ions in a linear radio-frequency Paul trap described in [3, 74] and depicted schematically in Fig. 5.1(b). The ions form a linear chain along the axis of the trap, the axis of weakest confinement. We perform experiments on either a single ^{9}Be$^+$ -^{24}Mg$^+$ pair or a four-ion chain with the ions in the order of ^{9}Be$^+$-^{24}Mg$^+$-^{24}Mg$^+$-^{9}Be$^+$ [3, 74]. A single trapped ^{9}Be$^+$ ion has a motional frequency $\omega_z = 2\pi \times 2.97$ MHz along the trap axis and $\{\omega_x, \omega_y\} = 2\pi \times \{12.4, 11.7\}$ MHz, along the transverse directions. An internal-state quantization magnetic field B is applied along a direction 45° to the trap axis in Fig. 5.1(b). This breaks the degeneracy of the magnetic sublevels of ^{9}Be$^+$ and ^{24}Mg$^+$, denoted by quantum number m_J. As in Fig. 5.1(a), m_J indicates the projection of the ^{24}Mg$^+$ ion's angular momentum along the direction of B. For B = 11.964 mT, the energy splitting of the qubit states $2s\ ^2\mathrm{S}_{1/2}\ |F=2, m_F=1\rangle$ and $|F=1, m_F=0\rangle$ of ^{9}Be$^+$ is first-order insensitive to changes in B, leading to long coherence times of superposition states [73].

We apply two laser beams near the $3s\ ^2\mathrm{S}_{1/2}$ to $3p\ ^2\mathrm{P}_{1/2}$ transition in ^{24}Mg$^+$ at approximately 280.353 nm [Fig. 5.1(a)]. These two beams are derived from the same laser and frequency shifted by acousto-optic modulators [106]. As indicated in Fig. 5.1(b), one of the beams propagates along the direction of B with σ^+ polarization to couple $|g_1\rangle$ to $|e\rangle$ with resonant Rabi rate Ω_1 and detuning Δ_1 from the excited state. The other beam has π polarization and couples $|g_2\rangle$ to $|e\rangle$ with resonant Rabi rate Ω_2 and detuning Δ_2. To meet the EIT prerequisite, we set $\Delta_1 = \Delta_2 = \Delta$, where $\Delta/2\pi$ can be set to a precision of approximately 1.5 MHz. To maximize the cooling, we set the difference wave-vector of the two beams parallel to the trap axis, so that the net momentum from the lasers

---

[5] From the Fano profile, the width is estimated to be $\gamma\omega/\Delta$, assuming the Rabi rates meet the EIT condition. Thus lowering Δ helps broadening the cooling bandwidth, however at the cost of cooling rates proportional to $\frac{4\omega(\omega+\Delta)}{\gamma}$ and the final phonon occupation number $\bar{n} \approx (\frac{\gamma}{4\Delta})^2$ [9].

have maximum projection on trap axis. To meet the EIT cooling condition Eq. 5.2, we control the values of Ω_1 and Ω_2 by adjusting laser beam powers with acousto-optic modulators, and the values of Ω_1 and Ω_2 are determined from measurements of the Rabi rate for Raman carrier transitions and the AC Stark shift from the σ^+ polarized beam when the laser is detuned from resonance.

The EIT laser cooling experiment includes the following processes. We first apply Doppler cooling to $^9\mathrm{Be}^+$, which initializes the temperatures of the axial modes of motion to near the Doppler limit given approximately by $\hbar\gamma_{\mathrm{Be}}/(2k_{\mathrm{B}})$, where γ_{Be} is the $^9\mathrm{Be}^+$ excited-state decay rate, and k_{B} is Boltzmann's constant). We then apply the EIT cooling beams to $^{24}\mathrm{Mg}^+$ for a duration t_c. To determine the final mean motional-state quantum number $\bar{n}$ of the normal modes, we use a pair of 313.220 nm laser beams [39, 106, 117] to compare the strength of the red and blue Raman sideband transitions in the $^9\mathrm{Be}^+$ ions on the $|2,1\rangle \rightarrow |1,0\rangle$ transition, as a temperature measurement for the sympathetically-cooled qubit ion [106]. We measure temperature on $^9\mathrm{Be}^+$ is that the $^{24}\mathrm{Mg}^+$ $S_{1/2} \rightarrow P_{1/2}$ transition is not a cycling transition and therefore not useful for state discrimination.

5.3.1 EIT cooling on the $^9\mathrm{Be}^+$-$^{24}\mathrm{Mg}^+$ ion pair

The ion pair has two axial motional modes: a mode where the two ions oscillate in-phase (**I**) with frequency $\omega_{\mathrm{I}}/2\pi = 2.1$ MHz and an out-of-phase mode (**O**) with frequency $\omega_{\mathrm{O}}/2\pi = 4.5$ MHz. The relevant ground state mode amplitudes for the $^{24}\mathrm{Mg}^+$ ion are denoted by z_0^{I} and z_0^{O} respectively. The contribution of $^{24}\mathrm{Mg}^+$ vibration to the mode is given by the unitless Lamb-Dicke parameters, defined as $\eta_{\mathrm{I,O}} = \Delta k_z z_0^{\mathrm{I,O}}$. This parameter reflects the effectiveness of $^{24}\mathrm{Mg}^+$ laser with the mode; here, $\eta_{\mathrm{I}} = 0.294$ and $\eta_{\mathrm{O}} = 0.083$. The EIT cooling condition $\delta \simeq \omega$ cannot be satisfied exactly for both modes simultaneously, since the mode frequencies are substantially different.

To investigate steady state performance of the EIT cooling, we EIT cool $^{24}\mathrm{Mg}^+$ in the pair for 800 μs, long enough for the system to reach equilibrium. We set $\Delta/2\pi = 96.7$ MHz and $\Omega_2/2\pi = 12.5$ MHz and we scan the value of Ω_1 to vary δ, as shown in Eq. (5.2). The minimum values of $\bar{n}_{\mathrm{I}} = 0.08(1)$ and $\bar{n}_{\mathrm{O}} = 0.04(1)$ are obtained when δ closely matches the respective mode frequency, as shown in Fig. 5.2(a). We observe a deviation $\simeq 10\%$ of the value of δ needed for optimum cooling compared to the mode frequency. The deviation can be explained by additional AC Stark shifts and photon scattering from the π-polarized beam that couples $|g_1\rangle$ to $|e'\rangle \equiv {}^2\mathrm{P}_{1/2}\ |m_J = -1/2\rangle$ in $^{24}\mathrm{Mg}^+$, see Fig. 5.1(a). We perform a numerical simulation of the full dynamics, including state $|e'\rangle$. We include the effects of heating rates of both modes, $\dot{\bar{n}}_\mathrm{I} = 0.38$ quanta/ms and $\dot{\bar{n}}_\mathrm{O} = 0.06$ quanta/ms. The simulation shows the average occupation numbers as solid lines in Fig. 5.2(a) and are in good agreement with our experimental results. For these simulations, we use the treatment of [8], which is valid in the Lamb-Dicke regime, adjusted for the relevant modes and mode amplitudes of the $^{24}\mathrm{Mg}^+$ ions.

To investigate the temporal dynamics of the cooling, we set δ to be near a mode frequency and measure $\bar{n}$ vs cooling duration t_c. We first Doppler-cool both modes with $^9\mathrm{Be}^+$ reaching $\bar{n}_\mathrm{I} \sim 5$ and $\bar{n}_\mathrm{O} \sim 2$. We find that at the experimentally determined optimum values of $\delta/2\pi$ of 2.55(5) MHz and 4.87(5) MHz, the $1/e$ cooling time for the **I** mode is 4(1) μs and for the **O** mode is 15(1) μs. The faster cooling rate for the in-phase mode is expected because of its larger $^{24}\mathrm{Mg}^+$ Lamb-Dicke parameter. This difference in equilibration times can be use to efficiently cool both modes, as shown in Fig. 5.2(b). We first set $\delta \simeq \omega_\mathrm{O}$ and apply cooling for 75 μs, yielding $\bar{n}_\mathrm{O} = 0.04(1)$. During this stage, the **I** mode is cooled to $\bar{n}_\mathrm{I} = 0.36(3)$. We then set $\delta \simeq \omega_\mathrm{I}$ and apply the cooling beams for an additional 10 μs, reaching $\bar{n}_\mathrm{I} = 0.08(1)$. In this second cooling stage, the **O** mode begins to heat to its equilibrium value of $\bar{n} = 0.19(3)$, shown in Fig. 5.2(a) for this value of δ. However in 10 μs, this heating is small, leading to a final value of $\bar{n}_\mathrm{O} = 0.07(2)$. Therefore, this two-stage cooling enables cooling of both modes to near their minimum $\bar{n}$ values in 85 μs[6] .

5.3.2 EIT cooling on the $^9\mathrm{Be}^+$-$^{24}\mathrm{Mg}^+$-$^{24}\mathrm{Mg}^+$-$^9\mathrm{Be}^+$ four-ion chain

We also investigate sympathetic EIT cooling for the four-ion chain. We label the four-ion axial modes $\{1, 2, 3, 4\}$. They have mode frequencies $\simeq \{2.0, 4.1, 5.5, 5.8\}$ MHz and corresponding $^{24}\mathrm{Mg}^+$ Lamb-Dicke parameters $\{0.21, 0.12, 0.063, 0.089\}$. Fig. 5.3 shows the final $\bar{n}$ of each mode vs.

---

[6] To achieve this result we roughly tune the laser power to be approximately 50% larger than expected, then stabilize the laser power and use the set points as a fine control of the laser power, to satisfy the EIT condition. In our previous experiments on $^9\mathrm{Be}^+$-$^{24}\mathrm{Mg}^+$ ion pair, the duration of the conventional Raman sideband cooling to cool both axial modes are ∼300 μs.

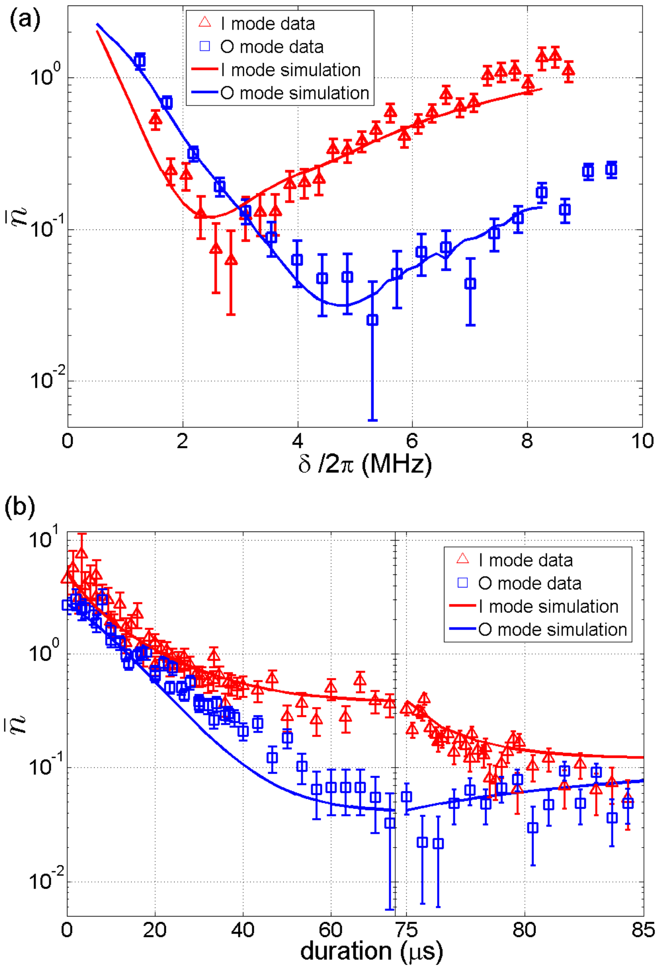

Figure 5.2: Mean motional excitation number $\bar{n}$ for the **I** (red triangles, $\omega/2\pi = 2.1$ MHz) and **O** (blue squares, $\omega/2\pi = 4.5$ MHz) axial modes of a ${}^{9}\mathrm{Be}^{+}$-${}^{24}\mathrm{Mg}^{+}$ ion pair. (a) $\bar{n}$ after 800 μs of EIT cooling as a function of $\delta/2\pi$. Optimal cooling for each mode occurs when δ approximately equals the mode frequency. (b) $\bar{n}$ plotted as a function of EIT cooling duration t_c. From 0 to 74 μs, $\delta \simeq \omega_{\mathrm{O}}$, the out-of-phase mode frequency. From 75 to 85 μs, $\delta \simeq \omega_{\mathrm{I}}$, the in-phase mode frequency. In both figures, error bars represent statistical uncertainty of the sideband amplitude ratios. The solid lines are simulations of the full dynamics including the $|e'\rangle$ level in ${}^{24}\mathrm{Mg}^{+}$, measured ambient heating rates, detuning and beam intensities. In the simulations, we truncated the motion to the first 6 Fock states for both modes for the steady-state simulation in (a) and to the first 10 (6) Fock states for the **I** (**O**) mode for temporal simulation in (b).

$\delta/2\pi$ after 800 μs of cooling to ensure steady state. We set $\Delta/2\pi = 96.7$ MHz, $\Omega_2/2\pi = 9.6$ MHz, and scan $\Omega_1/2\pi$ from 17 to 73 MHz. The EIT cooling bandwidth, estimated by $\delta\gamma/\Delta \approx 2\pi\times 2.5$ MHz , is sufficient that modes 2, 3, and 4 can be simultaneously cooled to near their minimum $\bar{n} < 0.15$ by setting $\delta/2\pi = 6.1$ MHz; however, at this value, mode 1 is cooled only to $\bar{n} = 0.7(1)$.

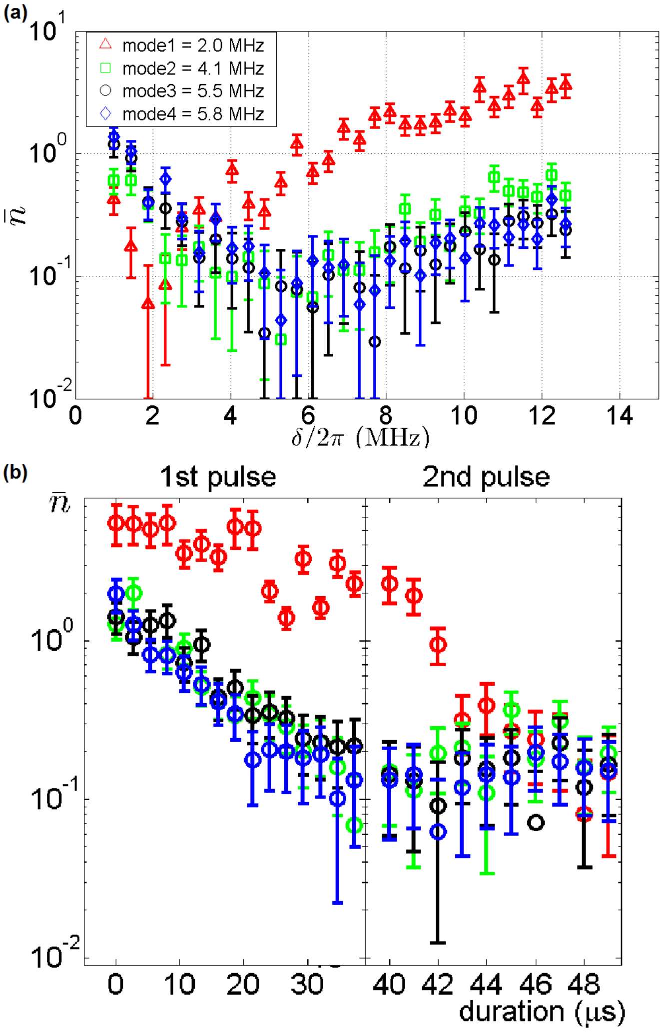

Figure 5.3: Sympathetic EIT cooling on a ^{9}Be$^+$-^{24}Mg$^+$-^{24}Mg$^+$-^{9}Be$^+$ ion chain. (a)Minimum $\bar{n}$ values for each of the four axial modes of a ^{9}Be$^+$-^{24}Mg$^+$-^{24}Mg$^+$-^{9}Be$^+$ ion chain as a function of $\delta/2\pi$ after 800 μs of cooling to ensure steady state. Modes 1 to 4 are shown in the legend, and labeled as red triangles, green squares, black circles and blue diamonds, respectively. (b) $\bar{n}$ plotted as a function of EIT cooling duration t_c. From 0 to 40 μs, $\delta \simeq \omega_3$, the mode 3 frequency. From 40 to 45 μs, $\delta \simeq \omega_1$, the mode 1 frequency. In both figures, error bars represent statistical uncertainty of the sideband amplitude ratios.

We therefore cool in two stages, similar to the ^{9}Be$^+$-^{24}Mg$^+$ case: (1) we first apply 40 μs of cooling with $\delta/2\pi = 6.1$ MHz to cool modes 2, 3, and 4, (2) then we cool 5 μs with $\delta/2\pi = 2.4$ MHz tuned to match mode 1. After these two steps, we achieve $\bar{n} = \{0.11(2), 0.20(5), 0.14(5), 0.18(5)\}$. In our experiments, laser beam power of the pi(sigma)-polarized beam ranges between 3 and 10 μW (3

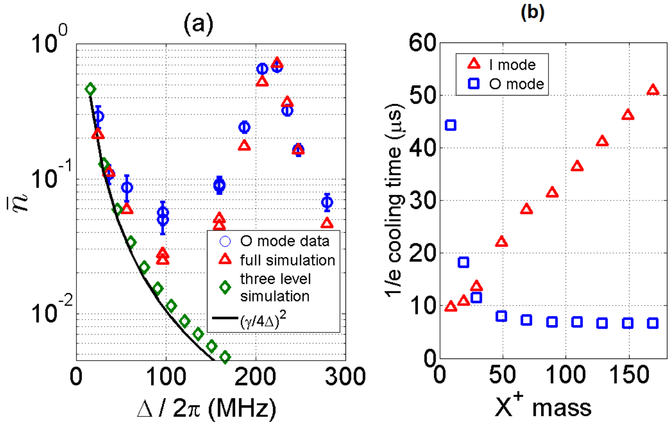

Figure 5.4: (a) Minimum values of $\bar{n}$ for the two-ion **O** mode vs. $\Delta/2\pi$. The peak near 223 MHz results from resonant scattering on the $|g_1\rangle \leftrightarrow |e'\rangle$ transition from the π polarized light. Blue circles are the experimental data and red triangles are simulations based on [8]. Green diamonds are simulations not including $|e'\rangle$ and the black solid line shows $\bar{n} = (\gamma/4\Delta)^2$ [9]. (b) Simulation of 1/e cooling time vs. the mass of ion X$^+$ that is sympathetically cooled by ^{24}Mg$^+$ (axial modes), with fixed trap potential such that $\omega_{\mathrm{I(O)}}/2\pi = 2.1$ (4.5) MHz when X$^+$ is ^{9}Be$^+$. Red triangles are for the **I** mode; blue squares for the **O** mode. Optimum values of δ were chosen for each mode and ion-mass combination, with $\Omega_2/2\pi = 5.9$ MHz and $\Delta/2\pi = 96.7$ MHz. (Here $|e'\rangle$ is neglected)

and 17 μW), respectively[7] . In previous implementations of sequential-Raman-sideband cooling [42, 74–76], cooling of these modes from Doppler temperatures to $\bar{n} \sim 0.1$ for each mode required $\sim 600\ \mu$s with approximately an order-of-magnitude higher laser intensities[8] .

5.3.3 Technical notes for EIT laser cooling

5.3.3.1 Off-resonant photon scattering from extra excited states

The $|g_1\rangle$ to $|e'\rangle$ transition frequency is 223.3 MHz higher than that of the $|g_2\rangle$ to $|e\rangle$ transition. Thus, EIT cooling will be strongly affected for Δ near 223.3 MHz because of recoil from scattering on the $|g_1\rangle$ to $|e'\rangle$ transition. To illustrate this effect, we measure the minimum value of $\bar{n}$ for cooling the **O** mode of the ^{9}Be$^+$–^{24}Mg$^+$ ion pair as a function of the detuning Δ depicted in Fig. 5.4(a). For each value of Δ, we optimize the EIT cooling by varying δ. The height of this recoil peak depends on the Rabi rate ratio Ω_2/Ω_1, with higher ratios leading to higher values of $\bar{n}$. For

---

[7] We did not measure the beam waists to high precision but they can be estimated to be approximately $100 \times 50\ \mu$m in $1/e^2$ intensity.

[8] with similar beam waists

data shown in Fig. 5.4(a), the ratio was held at 0.24. We note that for large detuning Δ, higher laser intensity is needed to maintain values of δ near the mode frequencies.

5.3.3.2 Induced transverse direction heating

When Δk_z is aligned along the trap axis, the motional modes along the transverse axes are heated by photon recoil. To study this effect we first cool one of the transverse modes of a $^9\mathrm{Be}^+$-$^{24}\mathrm{Mg}^+$ pair (frequency $\simeq 4.6$ MHz) to near its ground state with Raman sideband cooling on $^9\mathrm{Be}^+$. We then apply an EIT cooling pulse on the **O** mode, with similar laser beam conditions as above. After 60 μs the **O** mode is cooled from the Doppler temperature $\bar{n} \simeq 2$ to $\bar{n} = 0.04(1)$, while the transverse mode is heated from $\bar{n} = 0.20(6)$ to 0.9(2). Once the **O** mode is cooled to near its minimum value, the heating rate of the transverse mode decreases because the ion becomes approximately trapped in the dark state for spin and the ground state of axial motion. This relatively low transverse excitation should cause a negligible error on a two-qubit gate which is affected by the transverse modes only through second-order coupling to the axial mode frequencies due to Coulomb repulsions between the ions[9] [118, 119]. Furthermore, Doppler cooling of all modes before EIT cooling would prohibit any cumulative effect of the heating in experiments requiring many rounds of sympathetic cooling.

5.3.3.3 Sympathetic cooling efficiency on other ion pairs

To study the efficiency of EIT sympathetic cooling on other commonly used qubit ion species, such as $^{27}\mathrm{Al}^+$, $^{43}\mathrm{Ca}^+$ and $^{171}\mathrm{Yb}^+$, etc., we simulate cooling of an ion pair $^{24}\mathrm{Mg}^+$ - X^+, where X^+ is the sympathetically cooled ion of different mass, as shown in Fig. 5.4(b). Smaller differences in ion mass lead to more balanced mode amplitudes and a reduction in the difference of cooling rates for individual modes. Large mass imbalances lead to at least one motional mode having a small $^{24}\mathrm{Mg}^+$ amplitude and thus a long cooling time [109].

---

[9] In [118, 119], an effect is described where a frequency shift of the axial mode would be induced

5.4 Conclusion and future applications

In summary, we have described sympathetic cooling of ^{9}Be$^+$ ions by EIT cooling of ^{24}Mg$^+$ ions held in the same trap. We investigated the cooling for both an ion pair and a four-ion chain crystal that can be used as a configuration for performing entangling gates between pairs of ^{9}Be$^+$ ions in a scalable architecture [74–76]. By taking advantage of the different cooling rates for different modes of motion, we demonstrate a two-stage EIT-cooling scheme that can bring all modes to near their ground states. Compared to previous implementations of conventional Raman sideband cooling, sympathetic EIT cooling provides a broad cooling bandwidth, requires less laser power, and is technically easier to implement. This method may also be useful for sympathetic cooling of molecular ions, and for use in quantum logic spectroscopy [34], trapped-ion quantum simulation [113–116], strongly-confined neutral atoms [120], and nano-mechanical resonators [121].

5.5 Appendix: derivation for EIT cooling condition

Here, we present more detail on the derivation of Eq. 5.7.

$$zV_{1,int} = e^{iH_{\mathrm{mec}}t/\hbar} z e^{-iH_{\mathrm{mec}}t/\hbar} e^{i(H_0+V_0)t/\hbar} V_1 e^{-i(H_0+V_0)t/\hbar}. \tag{5.8}$$

From the definition of H_{mec} in the main text, we obtain for the motional part of $zV_{1,int}$,

$$\begin{aligned}
& e^{iH_{\mathrm{mec}}t/\hbar} z e^{-iH_{\mathrm{mec}}t/\hbar} && (5.9)\\
=& z_0 e^{iH_{\mathrm{mec}}t/\hbar} \Big(\sum_n (\sqrt{n}|n-1\rangle\langle n| + \sqrt{n}|n\rangle\langle n-1|)\Big) e^{-iH_{\mathrm{mec}}t/\hbar} \\
=& z_0 \sum_n (\sqrt{n} e^{i(n-1)\omega t}|n-1\rangle\langle n| e^{-in\omega t} + \sqrt{n} e^{in\omega t}|n\rangle\langle n-1| e^{-i(n-1)\omega t}) \\
=& z_0 \sum_n (\sqrt{n} e^{-i\omega t}|n-1\rangle\langle n| + \sqrt{n} e^{i\omega t}|n\rangle\langle n-1|), && (5.10)
\end{aligned}$$

and for the internal part, with the help from (5.1),

$$
\begin{aligned}
&e^{i(H_0+V_0)t/\hbar}V_1 e^{-i(H_0+V_0)t/\hbar}\\
=&\frac{i\hbar}{2}\frac{\Omega_1\Omega_2}{\Omega}(\Delta k)e^{i(H_0+V_0)t/\hbar}\Big(\cos\theta|\psi_+\rangle\langle\psi_D| + \sin\theta|\psi_-\rangle\langle\psi_D| - H.c.\Big)e^{-i(H_0+V_0)t/\hbar}\\
=&\frac{i\hbar}{2}\frac{\Omega_1\Omega_2}{\Omega}(\Delta k)\Big(\cos\theta e^{i\frac{\Delta+\sqrt{\Delta^2+\Omega^2}}{2}t}|\psi_+\rangle\langle\psi_D|e^{-i\Delta t} + \sin\theta e^{i\frac{\Delta-\sqrt{\Delta^2+\Omega^2}}{2}t}|\psi_-\rangle\langle\psi_D|e^{-i\Delta t} - H.c.\Big)\\
=&\frac{i\hbar}{2}\frac{\Omega_1\Omega_2}{\Omega}(\Delta k)(e^{i\frac{-\Delta+\sqrt{\Delta^2+\Omega^2}}{2}t}\cos\theta|\psi_+\rangle\langle\psi_D| + e^{i\frac{-\Delta-\sqrt{\Delta^2+\Omega^2}}{2}t}\sin\theta|\psi_-\rangle\langle\psi_D| - H.c.) \qquad (5.11)
\end{aligned}
$$

With (5.9) and (5.11),

$$
\begin{aligned}
zV_{1,int} =&\frac{i\hbar}{2}\frac{\Omega_1\Omega_2}{\Omega}(z_0\Delta k)\sum_n(\sqrt{n}e^{-i\omega t}|n-1\rangle\langle n| + \sqrt{n}e^{i\omega t}|n\rangle\langle n-1|)\times\\
&(e^{i\frac{-\Delta+\sqrt{\Delta^2+\Omega^2}}{2}t}\cos\theta|\psi_+\rangle\langle\psi_D| + e^{i\frac{-\Delta-\sqrt{\Delta^2+\Omega^2}}{2}t}\sin\theta|\psi_-\rangle\langle\psi_D| - H.c.). \qquad (5.12)
\end{aligned}
$$

Thus with $\frac{-\Delta+\sqrt{\Delta^2+\Omega^2}}{2} \approx \omega$, the $|\psi_{\mathrm{D}}, n\rangle \rightarrow |\psi_+, n-1\rangle$ transition is driven. For $\Delta \gg \Omega$, $\cos\theta \approx \frac{\Omega}{2\Delta}$, and the transition Rabi rate is approximately $\frac{\Omega_1\Omega_2 z_0\Delta k}{4\Delta}\sqrt{n}$.

Chapter 6

Steady state entanglement from dissipation

Quantum entanglement is a key phenomenon of quantum mechanics and plays an important role in quantum information processing, quantum simulation and quantum computation. Traditionally in trapped ion systems, entanglement can be generated by deterministic interactions such as coherent quantum operations [53, 122]. These operations can function as quantum logic gates, the work horse for quantum computation. Similar operations can also produce effective interactions that simulates interesting quantum systems such as Ising models [83, 123, 124]. High operation fidelity has been continually pursued, and although it's a technically difficult task, impressive progress has been made [43, 125]. In recent years, researchers have also studied different ways of generating quantum entanglement. One way is to use photons to link ions in separate traps [126], which is useful for distributed quantum computation, one way quantum computation and quantum networks. By this method, the entangled pair generation rate has been increased up to several Hertz [127]. On the other hand, entanglements can also be generated with measurement based methods, for example by photons interference [128, 129], by performing quantum-non-demolition measurements [33, 130] and by applying heralded methods [131] to atoms in a cavity. Another way is to introduce dissipation, where ideally all other states are pumped to the desired entangled state. In this case, previous experimental works include using quantum logic gates and optical repumping on auxiliary qubits, to pump to a Bell state [61], and using photons leaking between cavities to couple two atom ensembles together [60].

Here we study novel methods to generate entangled states without using entangling quantum logic operations. In this chapter, we introduce a dissipative steady state preparation method, where we do not use auxiliary qubits, but continuously apply spin-motion coupling, microwave fields, optical pumping and sympathetic cooling, which leads to a steady state highly overlapped with the desired entangled state.

6.1 Theory and concepts

Generating entanglement with dissipation has recently become a hot topic. Traditionally, a successful quantum information system implied extreme isolation from the environment because couplings with the environment destroys the fragile quantum information. For example, consider atoms trapped by optical lattices in a cavity, where atoms are coupled with the cavity photon mode. Because the cavity mirrors have finite reflectivity, photons have a non negligible possibility to be lost by escaping the cavity or being absorbed by the mirror. In this case, the environment is the space or materials out of the cavity, and the coupling to the environment is the loss of the cavity mirrors. However, a recent proposal [132, 133] suggests that the loss of photons can actually lead to effects analogous to optical pumping of the system, and a dark entangled state exists where all other states will eventually be pumped to that state, and entanglement is established and maintained as steady state. This proposal can be translated into the trapped ion context because of their similarity in couplings, and we implemented it here, with theoretical collaboration with F. Reiter and A. S. Sørensen from University of Copenhagen.

The experiment uses four trapped ions, in a $^9\mathrm{Be}^+ - ^{24}\mathrm{Mg}^+ - ^{24}\mathrm{Mg}^+ - ^9\mathrm{Be}^+$ ion chain. The ^{9}Be ions the quantum bits, and the goal is to form the entangled singlet state $|S\rangle \equiv \frac{1}{\sqrt{2}}(|\uparrow\downarrow\rangle - |\downarrow\uparrow\rangle)$, where the spins are defined in the hyperfine $S_{1/2}$ ground states of the ^{9}Be ions, as $|\uparrow\rangle \equiv |F = 1, m_F = 1\rangle$ and $|\downarrow\rangle \equiv |F = 2, m_F = 2\rangle$. We use a pair of Raman sideband laser beams to couple the ions via the motion, or phonons, in analogy to how the atoms in a cavity are coupled via photons. We also induce a repumping laser and microwave drive to create selective spin state pumping, as detailed below. The $^{24}\mathrm{Mg}^+$ ions serves as coolants. We can apply 280 nm laser beams to drive Raman sideband transitions and provide repumping to ground state cool the $^{24}\mathrm{Mg}^+$ ions.

In this case, we cool the entire ion chain without scattering photons on the qubit $^9\mathrm{Be}^+$ ions. This technique is called sympathetic cooling, and such a loss of phonons is analogous to the loss of photons from a cavity, however in the ion experiment, we can turn the cooling on and off and tune the strength conveniently while one cannot control the cavity mirror loss.

The two $^9\mathrm{Be}^+$ ions spins can be expressed in a basis spanned by the symmetric $|\uparrow\uparrow\rangle$, $|T\rangle$, $|\downarrow\downarrow\rangle$ and asymmetric $|S\rangle$ states, where $|T\rangle \equiv \frac{1}{\sqrt{2}}(|\uparrow\downarrow\rangle + |\downarrow\uparrow\rangle)$ is the triplet state. The core of our scheme is trying to induce dissipation to all the symmetric states, and pump the ions to the $|S\rangle$ state, while trying to have minimize leakage from $|S\rangle$ state, as illustrated by Fig. 6.2 a). In other words we try to minimize dissipation on the $|S\rangle$ state. It is a common misunderstanding that the scheme creates entanglement directly from the dissipation components. In our case, the dissipative components do not couple the ion spins. In fact, the entanglement is indirectly induced by the sideband laser; however this interaction is reshaped by a combination of dissipation and other coherent processes to create the targeted state. None of the ingredients of the scheme other than the sideband interaction are able to entangle the two qubit ions.

The dissipation is comprised of two distinct parts. The first part is a combination of sympathetic cooling and Raman sideband transitions, to pump within the symmetric subspace from $|\downarrow\downarrow\rangle \rightarrow |T\rangle \rightarrow |\uparrow\uparrow\rangle$, as depicted with Fig. 6.1. We apply the "blue" sideband, the motion adding sideband from the $|\downarrow\rangle$ state point, denoted by $H_s = \Omega_s(\sigma_1^+ + \sigma_2^+)b^\dagger + H.C.$, where Ω_s is the Rabi rate, $\sigma^+ = |\uparrow\rangle\langle\downarrow|$, subscript i denotes the i$^{\mathrm{th}}$ ion and b is annihilation operator. The plus sign between the two σ^+ operators in H_s is crucial to our experiment to define the target singlet dark state, and thus need to be handled carefully, as detailed below. If spin is in the $|\downarrow\downarrow\rangle$ and $|T\rangle$ states, the spin down component will get a spin flip up and gain one quantum of motion, which will be removed by the cooling process. However, with ground state cooling, if the spin state is $|\uparrow\uparrow\rangle$, the sideband cannot flip spin down and subtract a quanta from motion, so the $|\uparrow\uparrow\rangle$ state is a "dark" state for both the cooling and sideband coupling.

The second part of dissipation is a combination of microwave and optical pumping, to pump from the remaining symmetric state $|\uparrow\uparrow\rangle$ to the final targeted state $|S\rangle$. This process is tricky

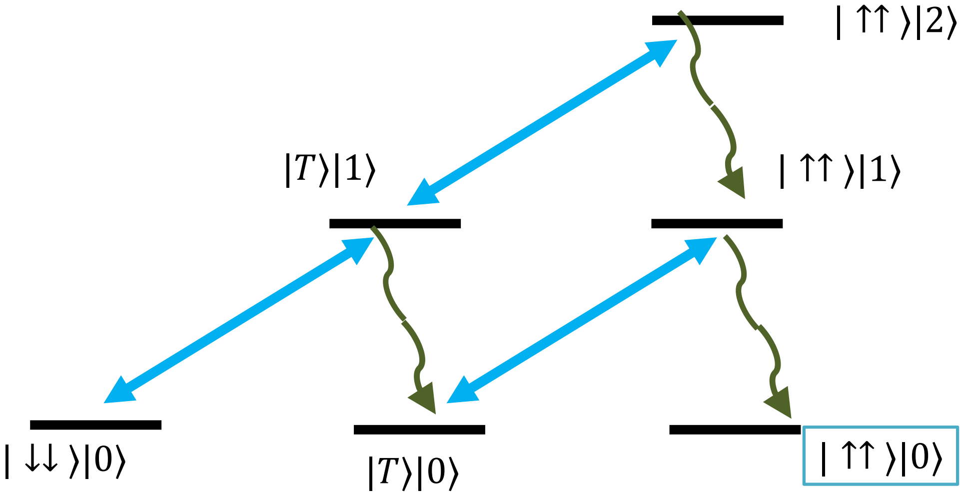

Figure 6.1: Sideband interactions together with sympathetic cooling. The former is expressed by blue double arrows and the latter green wavy arrows. Other than the $|\uparrow\uparrow, n = 0\rangle$ state, all other spin states can be driven by the sideband interaction, which produces spin flips and motional excitation simultaneously. However, with sympathetic cooling, the evolution would lead to pumping to the dark state of the sideband, the $|\uparrow\uparrow, n = 0\rangle$ state. This state is dark since the sideband could not flip spin down and subtract motional quanta at the same time.

because any direct optical pumping on the spin level will result in destruction of the target state. To prevent that, we use an auxiliary state $|a\rangle$, which the optical pumping acts on with rate γ, and a microwave carrier drive $H_c = \Omega_c(|\uparrow\rangle_1\langle a| + |\uparrow\rangle_2\langle a|) + H.C.$, from spin up to the auxiliary for both ion 1 and 2. We would like to have state-selected drive only on the $|\uparrow\uparrow\rangle$ state while keeping the $|S\rangle$ state untouched. This is accomplished by a side effect of the continuous Raman sideband interaction mentioned above. The microwave drives transitions $|\uparrow\uparrow\rangle \leftrightarrow \frac{1}{\sqrt{2}}(|\uparrow a\rangle + |a\uparrow\rangle) \leftrightarrow |aa\rangle$. These spin states at the ground state of motion are dark to the sideband excitation; therefore the microwave transitions occurs without being perturbed. In this case, repumping the $|a\rangle$ state returns the ions back to the qubit manifold, with a probability of creating the $|\uparrow\downarrow\rangle$ or $|\downarrow\uparrow\rangle$ states, which contain the targeted $|S\rangle$ state and the $|T\rangle$ state. Note that the $|T\rangle$ state is dissipatively pumped to the $|\uparrow\uparrow\rangle$ state. Considering the microwave transition $|S\rangle \leftrightarrow \frac{1}{\sqrt{2}}(|\downarrow a\rangle - |a\downarrow\rangle)$, the $|S\rangle$ state is unperturbed by the sideband excitation while the $\frac{1}{\sqrt{2}}(|\downarrow a\rangle - |a\downarrow\rangle)$ state is a superposition of two dressed eigenstates resulting from the sideband interaction, with eigenenergy of $\pm\Omega_s$ in the interaction frame of the strong sideband. The eigenstates are $\frac{1}{2}((|\downarrow a\rangle - |a\downarrow\rangle)|n=0\rangle \pm (|\uparrow a\rangle - |a\uparrow\rangle)|n=1\rangle)$, respectively. Thus if the microwave carrier Rabi rate Ω_c is weak enough, i.e. $\Omega_c \ll \Omega_s$, the transition from $|S\rangle$ is out of resonance, while the $|\uparrow\uparrow\rangle$ state is driven to auxiliary state resonantly and then pumped to the $|S\rangle$ state. Thus we have all the ingredients depicted in Fig. 6.2 b).

6.2 Experimental setup and results

We trapped a $^9\text{Be}^+ -^{24}\text{Mg}^+ -^{24}\text{Mg}^+ -^9\text{Be}^+$ ion chain in the linear trap described above. For the $^9\text{Be}^+$ ion, we label the $2s^2S_{1/2}$ internal states $|F=1, m_F=1\rangle \equiv |\uparrow\rangle$, $|2,2\rangle \equiv |\downarrow\rangle$ and $|2,1\rangle \equiv |a\rangle$. With such a choice of spin definitions, we can conveniently apply the red-Doppler "blue" laser beam as in Fig. 3.4 mentioned above to repump the $|a\rangle$ state back to the qubit manifold, with laser setup depicted in Fig. 6.2, and we set the strength of depletion for the $|a\rangle$ state with $1/e$ repump time to be 88 μs. The drawback of this selection is the unwanted depumping on the $|2,2\rangle$ states if the polarization of the repump beam is not purely σ^+, and the unwanted transition is ∼140 MHz red detuned from the laser frequency [87]. One way to get around this issue is interchanging the $|\uparrow\rangle$ and $|a\rangle$, and use the red-Doppler "red" beam Sec. 3.2 as repumper instead, however in our case we did not have Raman laser frequency and microwave coil setup to drive transitions between the $|2,2\rangle$ and $|2,1\rangle$ states, at the time of our experiment. For other choices of three ground state levels as the spin and auxiliary levels, however, one can use the field insensitive transition between $|2,1\rangle$ and $|1,0\rangle$ or $|2,0\rangle$ and $|1,1\rangle$ by selecting relevant magnetic field and have longer coherence time. However that induces difficulty on the repumping. For example define the spins as $|2,1\rangle$ and $|1,0\rangle$ states and auxiliary state to be the $|2,0\rangle$ state. The repumping process from the $|2,0\rangle$ state would also have a probability to populate the unwanted $|2,2\rangle$ and $|1,1\rangle$ states, which would require extra repumping laser beams to pump these states back to the manifold.

We measure the axial motional mode frequency to be $2\pi\times\{2.0,\ 4.1,\ 5.5,\ 5.8\}$MHz, labeled as mode $\nu_{\{1-4\}}$ respectively. The related mode amplitudes, Lamb-Dicke parameters [22] are in the Table 6.1. We apply our scheme to the stretch mode ν_3 to couple the ^{9}Be ions. This mode is chosen because it has the highest Lamb-Dicke parameters for the $^9\mathrm{Be}^+$ ions for better efficiency of Raman laser coupling, while having the lowest Lamb-Dicke parameters for the $^9\mathrm{Be}^+$ ions for low recoil during cooling, and it has relatively low ambient heating rate of the axial modes, ∼0.06 quantum/ms.

mode	frequency /(2πMHz)	amplitudes	$\lambda(^9\mathrm{Be}^+)$	$\lambda(^{24}\mathrm{Mg}^+)$
1	2.0	{0.322,0.629,0.629.0322}	0.155	0.207
2	4.1	{-0.466,-0.532,0.532,0.466}	0.155	0.121
3	5.5	{0.629,-0.322,-0.322,0.629}	0.180	0.063
4	5.8	{0.532,-0.466,0.466,-0.532}	0.149	0.089

Table 6.1: list of parameters for repumping, cooling and heating processes

6.2.1 Continuous application

For the Raman sideband, we use a pair of 313 nm laser beams, set up as Sec. 3.2. We tune the sideband laser frequency difference to be $f_0+\nu_3$, where f_0 is the qubit resonant frequency $2\pi\times1.018$ GHz. These two lasers are set to be ∼270 GHz red detuned from the $2s^2S_{1/2}$ to $2p^2P_{1/2}$ transition.

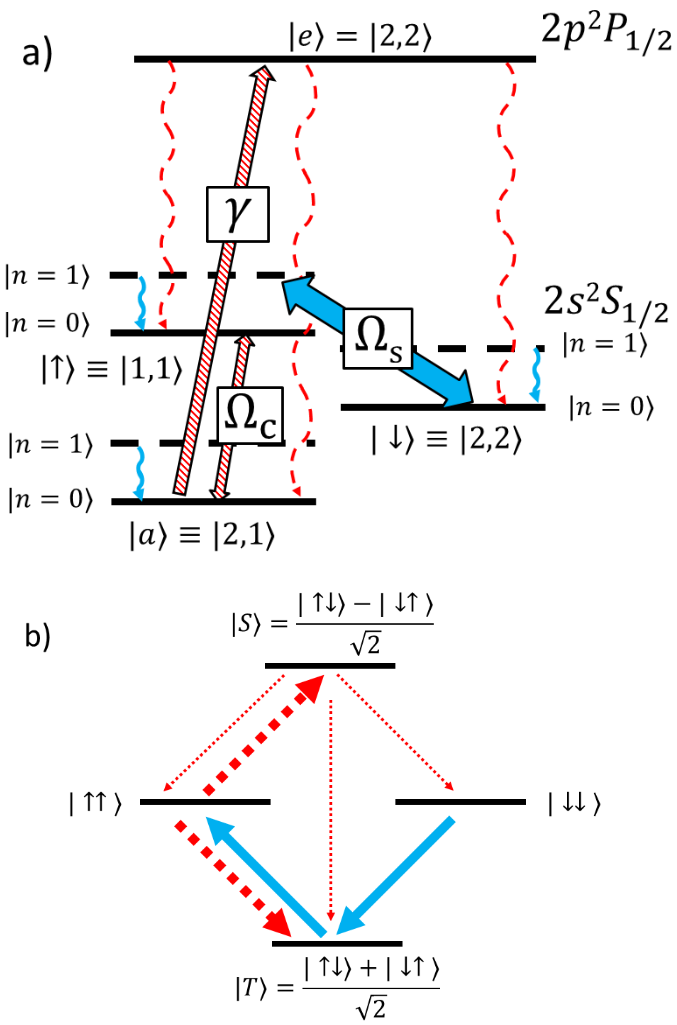

Figure 6.2: Energy Levels and Entanglement Preparation Scheme a) The internal energy levels (not to scale) of ^{9}Be$^+$ are shown as solid black lines for the ground motional state and dashed lines for the first excited motional state. The couplings needed to produce steady-state entanglement are shown with blue double arrows for the strong sideband coupling with Rabi rate Ω_s and sympathetic cooling; the patterned and dashed red arrows for the weak microwave coupling with Rabi rate Ω_c, repumper, and spontaneous emission from the $|e\rangle$ state. Wavy arrows depict the dissipative processes. b) Four spin states that span the $|\uparrow\rangle$, $|\downarrow\rangle$ qubit manifold of the two ^{9}Be$^+$ ions are shown as horizontal lines. Transfer processes that are accomplished by the sideband drive and sympathetic cooling are shown as blue arrows, while processes that occur by coupling the $|\uparrow\rangle$ state to the auxiliary $|\mathrm{a}\rangle$ state followed by excitation with the repumper and decay by spontaneous emission are shown as dashed red arrows. Processes shown as thin lines are shifted out of resonance due to the strong sideband coupling, leading to accumulation of population in the maximally entangled state $|\mathrm{S}\rangle$ in steady state.

More details of Raman sideband is described in Chapter 4. We measure the sideband Rabi rate to be $\Omega_s = 2\pi \times 7.8(1)$kHz, by scanning the laser pulse duration of the sideband transition, and fit the flopping curve to a cosine function. To control the sign between the two ions in H_s, since mode ν_3 has same sign of the mode amplitudes between the two $^9\mathrm{Be}^+$ ions, we need to set the laser phases on the ions to be also the same. For this purpose this we set the ion spacing so that the laser phase difference is integer m of 2π. The laser phase difference can be calculated with $\Delta_k z$, where $\Delta_k \approx \frac{2\pi}{313\mathrm{nm}}\sqrt{2}$ as the difference k vector along the trap axis, with laser beams incident 45° along the trap axis, but 90° between each other. For our confinement and for ν_3, $z \approx 11\mu$m, and m is near 50. We optimized the ion spacing by maximizing the creation of the target state. Better ways of doing it would be to apply the Zeno dynamics to compare the laser phase with the microwave uniform phase across the ions as described in Chapter 7, and if possible the most sensitive way is to apply the σ_z two ion phase gate [52].

We implement the microwave transition by using a dipolar antenna described in Sec. 3.2, and we set the power of the microwave input such that the carrier Rabi rate is $\Omega_c = 2\pi \times 0.543(6)$ kHz, which is determined by scanning the microwave pulse duration and fitting the curve to sinusoidal function. This gives $\Omega_s/\Omega_c \sim$14.

We continuously laser-cool the $^{24}\mathrm{Mg}^+$ ions to sympathetically cool the ion chain. We apply a pair of red sideband Raman lasers beams, and a repump beam simultaneously, setup as in Fig. 3.3. These lasers, with wavelength approximately at 280 nm and total laser power less than a few mW, interact negligibly with the spins of the $^9\mathrm{Be}^+$ ions. With the ^{24}Mg sideband Rabi rate $\Omega_{s,\mathrm{Mg}}$ and repump rate γ_{Mg}, controlled by laser power. We apply the sideband and repump laser beams simultaneously for continuous cooling. We set sideband laser beams resonant with the red sideband of mode 3, with $\Omega_{s,\mathrm{Mg}} \approx 2\pi \times 11.9$kHz and $\gamma_{\mathrm{Mg}} \approx 2\pi \times 625$ kHz, measured by observing the $1/e$ repumping time of $1.6\mu s$, giving a 1/e cooling time to be 203 μs, and cool to $\bar{n} = 0.11(1)$. We also observe off resonant cooling on modes 1, 2 and 4, with 1/e cooling times to be 1300 μs, 294 μs and 181 μs, with steady state $\bar{n}$ to be approximately 2.9, 0.95 and 0.12, respetively. We also tried using EIT cooling [78] for continuous sympathetic cooling, however we didn't achieve as good fidelity for the $|S\rangle$ state. One speculation is that due to the strong sideband couplings on both $^9\mathrm{Be}^+$ and $^{24}\mathrm{Mg}^+$ ions during the EIT cooling, the internal spins between $^9\mathrm{Be}^+$ and $^{24}\mathrm{Mg}^+$ ions is coupled via exchange of motional quanta, thus adds extra depumping channel for the targeted state. Also the EIT cooling is less controllable in terms of making the sideband coupling small but repumping to be strong, compared with the Raman sideband cooling case, since the same beam is providing both repumping and sideband coupling.

We apply all the interactions simultaneously and after about 6 ms, a steady state is obtained and with 0.75(3) fidelity obtaining the targeted $|S\rangle$ state, as shown in Fig. 6.3. Definition of fidelity is described in Sec. 1.1. This fidelity can be explained by numerical simulation, where we modeled the system with experimental parameters and imperfections, as explained in Sec. 6.2.3. The fidelity is obtained by averaging measurements between 6 and 12 ms. To measure spin population, we drive the cycling transition $|{\downarrow}\rangle \leftrightarrow 2p^2P_{3/2}|3,3\rangle$ for both $^9\mathrm{Be}^+$ ions for 250 μs, and by fitting the detected photon count histogram to Poisson distributions, we can distinguish the number of ions populated on the $|{\uparrow}\rangle$ state, i.e., $|{\uparrow\uparrow}\rangle$, $|{\downarrow\downarrow}\rangle$ and the combination of $|S\rangle$ and $|T\rangle$ states, which contains one spin up and one spin down. To further distinguish the latter two states, we need to insert microwave $\pi/2$ pulses on the spin transition, with varied phases. This detection method is explained in Sec. 3.4.

6.2.2 Stepwise Application

For the continuous application, we apply strong Raman sidebands, weak microwave drive, repumping laser beams, and sympathetic cooling simultaneously. We expect to achieve a steady entangled state with error on the order of Ω_c^2/Ω_s^2, due to the finite ratio between Ω_s and Ω_c, κ and γ, assuming the latter rates are on the same order of magnitude. Experimentally, this case also suffers from the spontaneous emission from the Raman sideband lasers as a significant source of error and the error rate will increase proportional to the duration of the laser application, as detailed below in Sec. 6.2.3.

One way to mitigate these issues is to apply the interactions in a stepwise manner, as shown

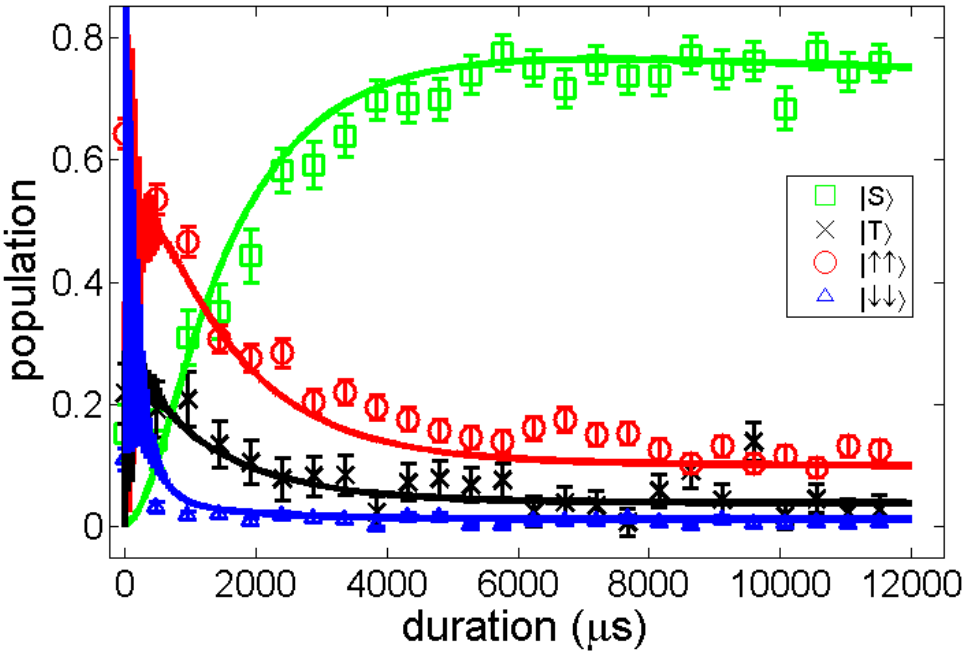

Figure 6.3: Steady State Entanglement. The measured populations of the singlet, triplet, $|\uparrow\uparrow\rangle$ and $|\downarrow\downarrow\rangle$ states are shown as squares, crosses, circles, and triangles, respectively, as a function of the duration that all the elements of the dissipative entanglement scheme are applied simultaneously. The system reaches a steady state with a 0.75(3) population in the target singlet state after a few milliseconds. The solid lines are the result of a simulation based on the experimental parameters. The slow decrease in the singlet state fidelity at long times visible in the simulation is due to a leak of the qubits to spin states outside the $|\uparrow\rangle$, $|\downarrow\rangle$, $|a\rangle$ manifold caused by spontaneous photon scattering from the Raman laser beams that generate the sideband coupling. Strictly speaking this depumping means that the state is only a quasi-steady state. For our parameters there is, however, a clear separation of the preparation and depumping time scales, justifying the description as steady state. Error bars represent standard deviations of each point.

in Fig. 6.4 a). In this case, we use a pulse sequence to create the $|S\rangle$ state, where each round of pulses contains one coherent segment and one dissipative segment. The coherent segment turns on the sideband and microwave, and the dissipative segment turns on the repumping and sympathetic cooling. The following gives a qualitative explanation of how this works by a comparison with the continuous application. In the continuous scheme, due to the stochastic property of the dissipative elements, the coherent evolution due to the combination of sideband and microwave is interrupted by repumping and cooling events. With finite Ω_c/Ω_s ratio, the $|S\rangle$ state is off-resonantly coupled to $\frac{1}{\sqrt{2}}(|\downarrow a\rangle + |a\downarrow\rangle)$ state, and the evolution, from the $|S\rangle$ state to superposition of the $|S\rangle$ state and the $\frac{1}{\sqrt{2}}(|\downarrow a\rangle + |a\downarrow\rangle)$ state, is interrupted by the dissipative repump event at random time stamp, causing a finite leak rate from the $|S\rangle$ state. However, in the stepwise application, we time the coherent segment to be $\frac{2\pi}{\sqrt{\Omega_s^2+\Omega_c^2}}$, so that we stop at the time where the evolution causes a return to the $|S\rangle$ state, as shown in Fig. 6.4 b), and at the same time we try to optimize the transition from the $|\uparrow\uparrow\rangle$ state by adjusting Ω_c. The combination of these two processes minimizes the leak rate from the $|S\rangle$ state and at the same time optimizes the creation rate of the $|S\rangle$ state. Therefore we can in theory eliminate the requirement of $\Omega_c/\Omega_s \ll 1$, increase Ω_s and make the entire application much shorter and less susceptible to spontaneous emisson error. In this case we lose some advantage of the continuous pumping where we can obtain a true steady state, but we can control Ω_c/Ω_s to be still not so large, and during the coherent evolution the qubits are not too far driven from the $|S\rangle$ state, thus on average it is an approximate steady state. Also for $|n \neq 0\rangle$, the oscillation period is dependent on n, and for non perfect ground state cooling this will give raise to extra errors. The true steady state would still be the most insensitive to laser power fluctuation and pulse duration imprecisions.

In the stepwise application, we set $\Omega_s = 2\pi \times 8.4(1)$ kHz and $\Omega_c = 2\pi \times 1.24(6)$ kHz, and we turn on the coherent subpulse with both sideband and microwave carrier for 106.5 μs, matching approximately with $2\pi/\sqrt{\Omega_s^2 + \Omega_c^2}$. For the dissipative subpulse, we set the repumping beam 1/e time to be approximately 3μs and turn on for 6 μs; and then we turn on sympathetic cooling for the axial modes for approximately 100 μs. In each cooling cycle, we cool each mode of motion by

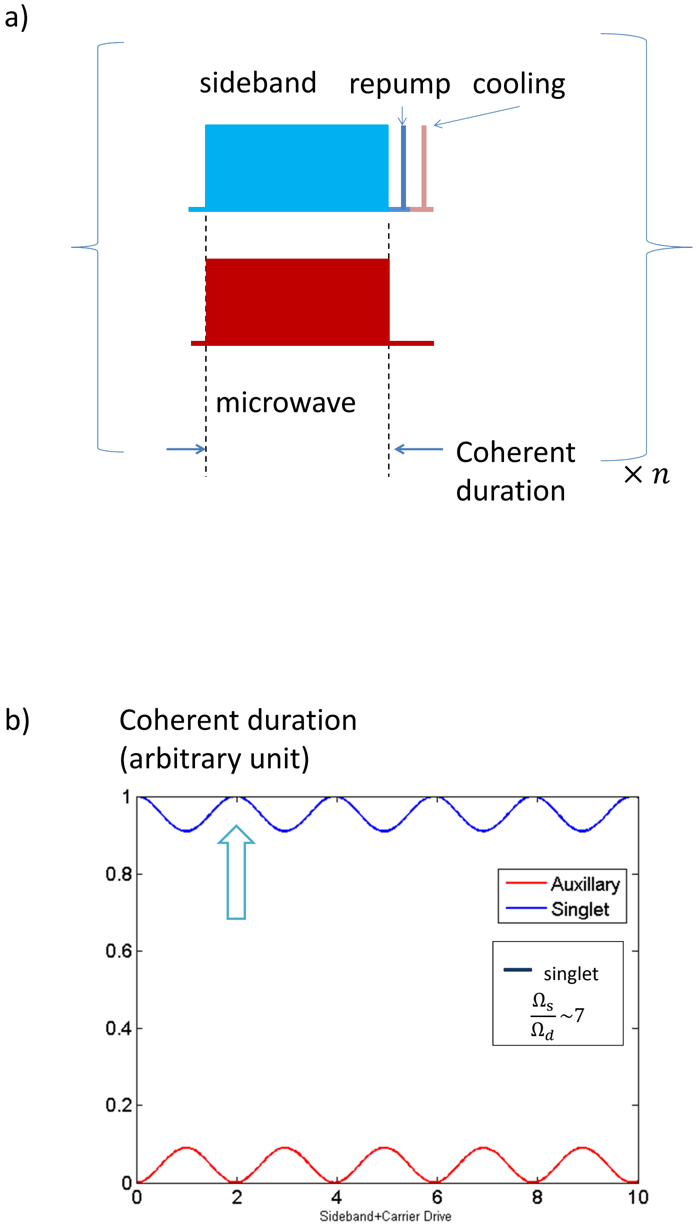

Figure 6.4: Stepwise application of the dissipative entanglement scheme. a) We show the pulse sequence for one step. In this case, we set the repump and cooling to be full power, and we turn them on with enough duration so that they act as a complete pumping step. These pulses remain short compared with the coherent pulse, thus not introducing too much gap time in between the coherent evolution. b) We assume initial state to be the target $|S\rangle$ state, and we show a simulation with the sideband and microwave drives are applied simultaneously. In this case, with $\Omega_s/\Omega_c \approx 7$, similar to the parameter in the stepwise experiment. We can see the microwave flops part of the $|S\rangle$ state out to the auxiliary level but the population can be fully revived at certain durations, as shown by an arrow in the figure. We set the duration of the coherent pulse in a) to be at one of those durations, so we eliminate the leakage out from the $|S\rangle$ state.

applying a red sideband π pulse followed by a repump beam to remove one motional quanta. The cooling cycles cools mode 1 first, which has the highest heating rate on the order of one quanta per ms; then we cool mode 2 and 4, and we cool mode 3 last to minimize heating on mode 3 between the cooling and the subsequent application of the coherent subpulses. We repeat the above cycle and we observe creation of steady state at about 30 steps. Note that in this case, the duration for the sideband laser at 30 step is approximately 3 ms, which is half of the continuous case. We measure the population of the $|S\rangle$ state, and we measure $|S\rangle$ state fidelity 0.89(2).

6.2.3 Numerical Simulation

With a numerical model, we simulation the scheme, including various experimental imperfections, such as (1) beam pointing fluctuations, which induces Rabi rate imbalance between the two ions (2) spontaneous photon scattering from the Raman laser beams which causes couplings of sideband laser to upper levels, which induces random spin flip and pumping to states out of the manifold of $\{|\uparrow\rangle, |\downarrow\rangle$ and $|a\rangle\}$ (3) imperfect cooling, and ambient heating process, (4) off resonant coupling to other axial motional modes.

We assume a Markovian process of the system-environment coupling, and we use the Lindblad master equation for modeling [134, 135]

$$\dot{\rho} = -i[H_{coh}, \rho] + \sum_j (L_j \rho L_j^\dagger - \frac{1}{2}(L_j^\dagger L_j \rho + \rho L_j^\dagger L_j)), \tag{6.1}$$

where H_{coh} is the Hamiltonian for the coherent interactions, as detailed below; L_j are different dissipative components for the process; and ρ is the system density matrix. Here we model ρ including the $|\uparrow\rangle$, $|\downarrow\rangle$, and $|a\rangle$ for each ${}^9\text{Be}^+$ ion. Additionally, two more ${}^9\text{Be}^+$ levels $|o\rangle \equiv |F = 1, m_F = 0\rangle$ and $|t\rangle \equiv |F = 2, m_F = 0\rangle$ are included, to capture the effect of spontaneous emission that pumps the system out of the desired manifold. For the motional levels, we include the first 7 motional levels for mode 3, the motional mode for Raman sidebands; and we include the first 3 motional levels for mode 4, where the Raman sideband has a small off resonance coupling.

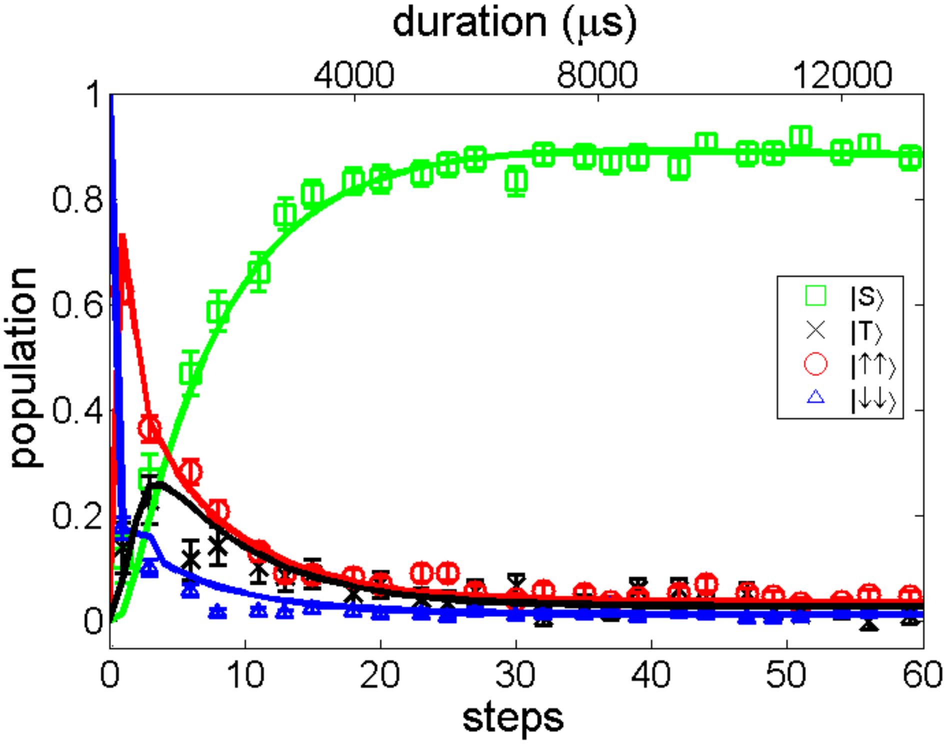

Figure 6.5: Entanglement With Stepwise Scheme. The measured populations of the singlet, triplet, $|\uparrow\uparrow\rangle$ and $|\downarrow\downarrow\rangle$ states are shown as squares, crosses, circles, and triangles, respectively, as a function of the number of applied steps. Each step has a duration of approximately 220 μs. The solid lines are the result of a model as explained in the Methods section. Error bars represent standard deviations of each point.

6.2.3.1 Dissipative Components

We assume the dissipative components are the same on both ions. We model the repumping in the desired manifold by $L_{\gamma_{j,a}} = \sqrt{\gamma_{j,a}}|a\rangle\langle\uparrow|$, where j denotes the $|\uparrow\rangle$, $|\downarrow\rangle$ and $|a\rangle$states. We model the continuous sympathetic cooling on $^{24}\mathrm{Mg}^+$ ions to be $L_\kappa = \sqrt{\kappa}b$, measured by observing the 1/e cooling time for mode 3, which was 203 μs, determined by exponential fit of the $\bar{n}$ from Doppler-cooled value of $\bar{n} \approx 2.5$ to the sideband coupling steady state $\bar{n} = 0.11(1)$. And we account for a heating process that limits the cooling represented by $L_{\kappa_h} = \sqrt{\kappa_h}b^\dagger$, where $\kappa_h = \kappa\frac{\bar{n}}{1+\bar{n}}$, with experimentally measured $\bar{n}$ from sideband cooling. The parameter κ and κ_h include the ambient motional heating rate of 0.06 quantum/ms. We similarly define κ_4 and $\kappa_{4,h}$ for mode 4, with annihilation operator c. The parameter κ_4 and $\kappa_{4,h}$ include the ambient motional heating rate of mode 4 of 0.0085 quantum/ms. For the stepwise case, we model the sympathetic cooling by simulating the sideband π pulse with Hamiltonian $H_{\mathrm{Mg}} = \Omega_{s,\mathrm{Mg}}(\sigma^+_{1,\mathrm{Mg}} + \sigma^+_{2,\mathrm{Mg}})b + H.C.$, taking into account the imperfection of driving a π sideband pulse of two $^{24}\mathrm{Mg}^+$ ions for motional population $|n \geq 2\rangle$. This is followed by a repump pulse with Lindblad operator $L_{\mathrm{rep,Mg}} = \sqrt{\gamma_{\mathrm{Mg}}|\uparrow_{\mathrm{Mg}}\rangle\langle\downarrow_{\mathrm{Mg}}|}$. In this case, the κ and κ_h mostly reflected the ambient heating. The above parameters for the continuous and stepwise application are in Table 6.1 and Table 6.2. For the stepwise case, we turn up the laser powers for the repumping and cooling so that we apply the repumping and cooling in much shorter pulses than the continuous case. The imperfection of motional mode cooling affects the creation rate for the $|S\rangle$ state, reducing its steady state population, or giving an error by 0.02 for the continuous application. The $|S\rangle$ state creation was also affected by beam pointing fluctuation, detailed below, giving an error of 0.02 for the continuous case. For the step wise application, if we eliminates the heating processes the error in the numerical simulation decreases by 0.04. This error is a combination of the above effects and the motional Fock state dependence of the oscillation from $|S\rangle$ to the $\frac{1}{\sqrt{2}}(|\downarrow a\rangle - |a\downarrow\rangle)$ state.

We model the spontaneous photon scattering processes from Raman laser beams as random spin flips from the state i to the state j with Lindblad operator $L_{j,i} = \sqrt{\Gamma_{j,i}}|j\rangle\langle i|$, where $\Gamma_{j,i}$

can be calculated using the Kramers-Heisenberg formula [46]. We experimentally measure $\Gamma_{j,i}$ by preparing at state i and observing the population build up at state j over time. Since the spontaneous emission rate is on the order of $10^{-4}\Omega_s$, we can to a good approximation ignore multi scattering events during the measurements, and use a linear fit to extract the spontaneous emission rates for short durations. The parameters we used in the simulation are shown in Table 6.2. The similarity of continuous and stepwise cases are due to the similar Raman sideband Rabi rates. For the simulation, we found the error due the the spontaneous emission to be approximately 0.07 for the continuous and 0.04 for the stepwise applications. To make the error smaller, one possibility is to create the sideband coupling with near-field microwave [136] or static field gradients [86], but the require field strength may be difficult to achieve for this scheme.

property	values	property	values
$\Gamma_{\downarrow,\uparrow}/(2\pi)$, $\Gamma_{\uparrow,\downarrow}/(2\pi)$	1.32 Hz	$\Gamma_{a,\uparrow}/(2\pi)$	0.39 Hz
$\Gamma_{t,\uparrow}/(2\pi)$	0.49 Hz	$\Gamma_{o,\uparrow}/(2\pi)$	0.28 Hz
$\Gamma_{a,\downarrow}/(2\pi)$	0.78 Hz	$\Gamma_{\downarrow,a}/(2\pi)$	0.39 Hz
$\Gamma_{t,a}/(2\pi)$	0.83 Hz	$\Gamma_{o,a}/(2\pi)$, $\Gamma_{a,o}/(2\pi)$	0.49 Hz
$\Gamma_{\uparrow,t}/(2\pi)$	0.29 Hz	$\Gamma_{a,t}/(2\pi)$	0.83 Hz
$\Gamma_{\uparrow,o}/(2\pi)$	0.49 Hz		

Table 6.2: list of parameters for spontaneous photon scattering processes from Raman laser beams; we use the same numbers for simulation in both the continuous and stepwise cases.

6.2.3.2 Coherent Components

We model the coherent Hamiltonian as

$$H_{coh} = H_s' + H_c + H_4, \tag{6.2}$$

$$H_s = \Omega_s((1-\frac{r}{2})\sigma_1^+ + (1+\frac{r}{2})\sigma_2^+)b^\dagger + H.C., \tag{6.3}$$

$$H_c = \Omega_c(|\uparrow\rangle_1\langle a| + |\uparrow\rangle_2\langle a|) + H.C. \tag{6.4}$$

$$H_4 = \Omega_s\frac{\eta_4}{\eta_3}\frac{\zeta_4}{\zeta_3}(|\uparrow\rangle_1\langle a| - |\uparrow\rangle_2\langle a|)c^\dagger e^{-i\delta t} + H.C. \tag{6.5}$$

where H_4 denotes the off resonant coupling to mode 4. In the following we will describe and define components of the above equations.

In Eq. 6.3, r is a parameter to represent Rabi rate imbalance between ions, due to the finite Gaussian beam waist and beam pointing fluctuations. To determine the r value induced by each of the Raman sideband beams, we perform a Stark shift experiment on each of the beams. We apply two $\pi/2$ microwave pulses sandwiched with one of the off resonant Raman laser beam, and observe the decay of sinusoidal flopping of spin populations due to a combination of laser intensity fluctuation on the ion and spontaneous emission. Laser beam intensity fluctuation can be caused by the overall laser power fluctuations and beam pointing fluctuations. To extract each component, we perform the same measurements on a single $^9\mathrm{Be}^+$ ions and a $^9\mathrm{Be}^+ -^{24}\mathrm{Mg}^+ -^{24}\mathrm{Mg}^+ -^{9}\mathrm{Be}^+$ chain and compare the difference, since the single ion experiment will be more sensitive to power fluctuations and the ion chain experiment will be more sensitive to beam position fluctuations. We model the decay spin flopping for one and two $^9\mathrm{Be}^+$ ion cases as

$$P_1 = \frac{1}{2} + \frac{1}{2}e^{-\eta t} Re[\langle e^{i\Omega_0 t - \frac{1}{4}\delta_1^2 t^2} e^{-2\xi^2/w_0^2} \rangle_{\xi \sim e^{-\xi^2/\delta_2^2}}], \tag{6.6}$$

$$P_2 = \frac{1}{2} + \frac{1}{2}e^{-\eta t} Re[\langle e^{i\Omega_0 t - \frac{1}{4}\delta_1^2 t^2} e^{-2(\xi - x_0)^2/w_0^2} \rangle_{\xi \sim e^{-\xi^2/\delta_2^2}}] \tag{6.7}$$

respectively, where P_1 is the probability of one ion at spin up after the sequence of the Ramsey experiment, and P_2 is the average value of P_1 on each $^9\mathrm{Be}^+$ ion in the $^9\mathrm{Be}^+ -^{24}\mathrm{Mg}^+ -^{24}\mathrm{Mg}^+ -^{9}\mathrm{Be}^+$ chain; η represents the decay due to spontaneous emission, Ω_0 is the free flopping rate for the Stark experiment, δ_1 represents the overall laser intensity fluctuation assuming a Gaussian noise ($\Omega \sim e^{-(\Omega - \Omega 0)^2/\delta^2}$), w_0 is the beam waist (intensity profile $\sim e^{-2x^2/w_0^2}$), x_0 is the position of ion away from center, δ_2 represents the beam pointing position fluctuation assuming Gaussian noise, and the notation $\langle f(x) \rangle_{x \sim g(x)}$ means the average of function $f(x)$ over a distribution of parameter x over function $g(x)$. The expression $r = 2\sqrt{2}x_0\delta_2$ relates position fluctuation to r. We fit the data of the CO and 90 Raman beams, and we extract a list of relevant values, as shown in Table. 6.3. We determine the final root-mean-square of r values to put in Eq. 6.3 as $\frac{r_{90}+r_{CO}}{\sqrt{2}} = 0.014$. In the full simulation, we compare the steady state fidelity with and without the effect from r$\neq$ 0, and we observe an error change by 0.02 for the continuous and 0.01 for the stepwise application of the scheme. In addition to our thoughts in the supplementary information in [79], we found a good way to reduce the beam pointing fluctuation by applying the photonic crystal structure UV wavelength fibers [7], which converts beam pointing noise into amplitude noise, and combines this with laser power stabilization using a detector after the fiber.

property	CO beam	90 beam
x_0/ω	0.11	0.07
δ_1/Ω_0	0.02	0.01
δ_2/ω	0.04	0.04
r	0.012	0.008

Table 6.3: fit values from the Stark experiment decaying flopping

In Eq. 6.5, $\delta \approx 2\pi \times 250$kHz is the mode frequency difference between modes 3 and 4, and $\{\eta_3 = 0.180,\ \zeta_3 = 0.629\}$ and $\{\eta_4 = 0.155,\ \zeta_4 = 0.532\}$ are the Lamb-Dicke parameters and mode amplitude for ^{9}Be$^+$ ion of modes 3 and 4, respectively. Note that since the mode amplitudes for modes 3 and 4 are opposite on the ^{9}Be$^+$ ions, the signs between the ion operators are opposite between H_s and H_4. Thus for H_4, the $|S\rangle$ state is no longer a dark state, and is coupled to $|\uparrow\uparrow\rangle|n_4 = 1\rangle$, with motional excitation in mode 4, which is then dissipated by the sympathetic cooling for this mode during the scheme. We find this effect creates a drop of fidelity in the simulations to be 0.006 and 0.016 for the continuous and stepwise applications, respectively. The reason why this effect is more important for the stepwise case is not completely understood. One possible explanation is that in the stepwise case, the duration for the coherent pulse makes the transition from the $|S\rangle$ state more favorable than the continuous case.

Chapter 7

Entanglement generation by confining dynamics in a subspace

7.1 Introduction

Entangled states are a crucial resource in quantum-based technologies such as computers and communication systems [27]. With current errors in entanglement generation, it is important to explore new methods. Here we restrict the number of energy states available to global rotations with applied laser fields, in an approach that has become known as quantum Zeno dynamics [54–56]. Under suitable microwave driving fields, a separable state evolves into an entangled state. With two trapped ions, we obtain Bell state fidelities up to 0.992(2); with three ions, a W-state [137] fidelity of 0.905(5). The procedure is relatively insensitive to certain imperfections such as fluctuations in laser intensity and frequency, and motional mode frequency. Since the function of the laser beams here is to provide strong restriction of the microwave driven dynamics, the exact laser parameters are not critical. This technique can be generalized to other systems.

The quantum Zeno effect has usually been referred to as the inhibition of quantum dynamics due to frequent measurements [55, 138]. This basic idea can be generalized to restrict the dynamics to within an unmeasured subspace of the overall system. Recent proposals [139–147] show that the subspace isolation can also be created by coupling the remainder of the system to auxiliary levels. Dynamics within the isolated subspace[1] can be implemented even though the system may undergo unitary evolution, without measurement. For sufficiently large perturbations, the system dynamics become confined to the unperturbed subspace. For measurement-based Zeno dynamics,

---

[1] also known as quantum Zeno dynamics

there will be a finite probability of escaping from the desired subspace disspatively. However, if the restriction is brought about by coherent interactions, there will be no dissipation, and thus the state amplitudes that leak from the restricted subspace remain coherent and can in principle be recovered with unitary operations.

Dynamics in the restricted subspace have recently been demonstrated with atoms in Bose-Einstein condensates [148], atoms in a cavity [149], atoms with Rydberg-Rydberg interactions [150] and photons in superconducting cavities [151]. In this work, we apply coherent laser fields to confine the quantum evolution of effective spin-$\frac{1}{2}$ particles realized with trapped ions between an initial product state and an entangled state of the internal states of the ions. This represents a novel technique to create entanglement, which can have important applications to quantum computing and quantum communication systems [27, 152]. We also demonstrate an advantage of the coherent subspace creation where, with application of composite pulse sequence, amplitudes escaped from the desired subspace can be brought back, thus improving the production of entangled state.

In our implementation, the dynamics within the confined subspace is driven by single-qubit unitary rotations operations, which can achieve high fidelity as demonstrated experimentally in [57–59, 153, 154]. However, these operations alone cannot directly generate entanglement between multiple qubits. For example, when applying a global rotation to an initial state with N spin-$\frac{1}{2}$ systems in the spin up state $|\uparrow\rangle$, each spin rotates independently and remains separable. In the Dicke states basis [155], the spins evolve in the symmetric angular momentum manifold $|J = N/2, m_J\rangle$ [156], where J is the total angular momentum quantum number and m_J is the projection of angular momentum along a quantization axis. All individual $|J, m_J\rangle$ states are entangled states except the maximal spin states, $|\uparrow\uparrow ... \uparrow\rangle = |J, J\rangle$ and $|\downarrow\downarrow ... \downarrow\rangle = |J, -J\rangle$. To generate entanglement, one can perturb specific $|J, m_J\rangle$ states in the manifold to alter the dynamics. A simple case is to apply a perturbation to shift the $|J, J-2\rangle$ state out of resonance, as depicted in Fig. 7.1. In this case, the dynamics are restricted within the $|J, J\rangle$ and $|J, J-1\rangle$ states. Thus starting from $|J, J\rangle$, with one effective π-pulse, the entangled $|J, J-1\rangle$ state [137, 157], is prepared. For two and three spins, these states are the triplet Bell state $|T\rangle = \frac{1}{\sqrt{2}}(|\uparrow\downarrow\rangle + |\downarrow\uparrow\rangle)$; and W-state [137]

$|W\rangle = \frac{1}{\sqrt{3}}(|\uparrow\uparrow\downarrow\rangle + |\uparrow\downarrow\uparrow\rangle + |\downarrow\uparrow\uparrow\rangle)$, respectively.

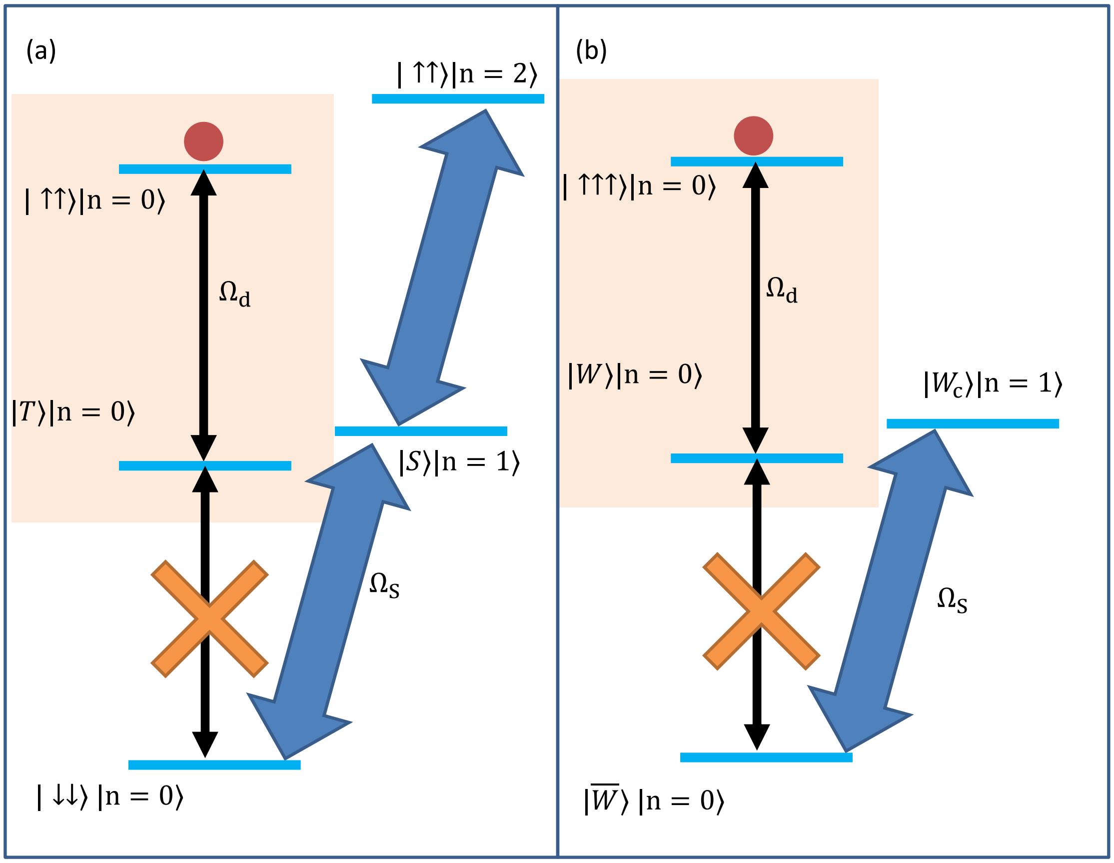

Figure 7.1: Schematics for confined dynamics, for the cases of (a) two ions, and (b) three ions. The thin black double arrows depict the relatively weak microwave coupling, and the thick blue double arrow depicts the strong laser sideband coupling. With $|\uparrow ... \uparrow\rangle$ states initially populated (red dots), the microwaves drive the state down the symmetric manifold, the states on the left, where $|\overline{W}\rangle = \frac{|\uparrow\downarrow\downarrow\rangle + |\downarrow\uparrow\downarrow\rangle + |\downarrow\downarrow\uparrow\rangle}{\sqrt{3}}$ in (b). However, the sideband excitations perturb the lower states, coupling them to other states, denoted by $|S\rangle$ and $|W_c\rangle = \frac{e^{i2\pi/3}|\uparrow\uparrow\downarrow\rangle + |\uparrow\downarrow\uparrow\rangle + e^{-i2\pi/3}|\downarrow\uparrow\uparrow\rangle}{\sqrt{3}}$. Thus the microwave induced dynamics are confined between the two highest energy states on the symmetric manifold. For (b) we only show the states that are relevant to the dynamics.

7.2 Two ion implementation

We experimentally demonstrate this scheme with trapped $^9\mathrm{Be}^+$ ions aligned along the axis of a linear Paul trap. At an external magnetic-field of 11.946 mT, applied approximately 45° to the axis, as shown in Fig. 3.3, the energy splitting $\omega_0 \approx 2\pi \times 1.2075$ GHz of the $^2S_{1/2}$ hyperfine ground states $|F = 2, m_F = 0\rangle \equiv |\downarrow\rangle$ and $|F = 1, m_F = 1\rangle \equiv |\uparrow\rangle$, is first-order insensitive to magnetic field fluctuations [73]. The effective rotation in the restricted subspace is produced by a uniform resonant microwave field, while the perturbations are provided by a laser-induced coupling between ions via a shared motional mode.

With two ions in the trap, the center-of-mass "COM" and the "stretch" axial normal modes of motions has frequencies $\{\omega_c, \omega_s\} \approx 2\pi \times \{3.58, 6.20\}$ MHz, as described in Sec. 4.1. The microwave field couples the unperturbed Dicke states with the Hamiltonian

$$H_d = \hbar\Omega_d \sum_{i=1,2} \sigma_i^x = \sqrt{2}\hbar\Omega_d(|\downarrow\downarrow\rangle\langle T| + |T\rangle\langle\uparrow\uparrow|) + H.C., \tag{7.1}$$

where $\hbar$ is the reduced Planck constant, Ω_d is the single-ion Rabi rate, and σ_i^x is the Pauli operator on the i^{th} ion. If the spins are initially in a product state, evolution under this Hamiltonian will not generate entanglement. The perturbation from laser couplings effectively remove the terms $|\downarrow\downarrow\rangle\langle T| + H.C.$ from H_d, thus an effective dynamics is implemented between $|\uparrow\uparrow\rangle$ and $|T\rangle$ states with Rabi rate $\sqrt{2}\Omega_d$. The effective π time for the $|\uparrow\uparrow\rangle \leftrightarrow |T\rangle$ transition is thus $t_\pi = \pi/(2\sqrt{2}\Omega_d)$.

To generate the desired dynamics, we induce the sideband interaction by applying a pair of laser beams (Be CO and BE 90) such that the difference of their momentum vectors $\mathbf{\Delta k}$ aligned along the trap axis and their frequency difference set to $\omega_0 + \omega_s + \delta$, as shown in Fig. 3.3. Setting the equilibrium position of ion 1 to be the origin of the axis, we denote the equilibrium position of ion 2 to be z. The lasers induce a near-resonant "blue sideband" coupling described in the interaction frame by

$$H_s = \hbar\Omega_s(\sigma_1^- - e^{i|\mathbf{\Delta k}|z}\sigma_2^-)ae^{-i\delta t + i\phi} + H.C., \tag{7.2}$$

where $e^{i|\mathbf{\Delta k}|x}$ is the differential optical laser phase. The minus sign between the σ operators results from the opposite motional mode amplitudes of the ions in the stretch mode. The common phase of the laser beams at the origin for $t = 0$ is denoted as ϕ, and will become important for the scheme based on composite pulse sequence. To obtain the coupling of Eq. 7.3, we adjust the axial confinement such that the ion-spacing x is near $M\frac{2\pi}{|\mathbf{\Delta k}|}$, where M is an integer number here with $M = 18$. Since ϕ is not important in the single pulse application, here we set it to zero. With this setting, we have

$$H_s = \hbar\Omega_s(\sigma_1^- - \sigma_2^-)ae^{-i\delta t} + H.C., \tag{7.3}$$

where Ω_s is the Rabi rate, a is the annihilation operator of the stretch mode, and $\sigma^- = |\downarrow\rangle\langle\uparrow|$. This interaction does not couple to the $|T, n\rangle$ state. However, it couples the states $|\downarrow\downarrow\rangle|n\rangle \leftrightarrow |S\rangle|n+1\rangle \leftrightarrow |\uparrow\uparrow\rangle|n+2\rangle$, where $|n\rangle$ denotes a stretch mode Fock state, and $|S\rangle = \frac{1}{\sqrt{2}}(|\uparrow\downarrow\rangle - |\downarrow\uparrow\rangle)$. The energies of the coupled states are shifted by approximately $\pm\hbar\Omega_s$ and $4\hbar\Omega_s$, if the δ is set to $\sqrt{\frac{7}{3}}\Omega_s$, as shown in Sec. 4.2.5. In addition, H_s couples $|\uparrow\uparrow, n\rangle$ to $|S, n-1\rangle$ for $n > 0$, therefore we want to initialize the stretch mode in the ground state. Thus for n=0, if the shifts are much larger than $\hbar\Omega_d$, the system evolves as an effective two-level system between $|\uparrow\uparrow\rangle|0\rangle$ and $|T\rangle|0\rangle$ under the combined influence of H_s and H_d. However, $|\uparrow\uparrow, n > 0\rangle$ states will also couple to the laser interaction and the desired subspace will not be isolated, therefore, high fidelity ground state motional preparation is crucial.

To initialize the spin and motional states, we first cooled both axial modes of the ions to near the ground state, achieving average motional occupation of $\bar{n} < \{0.01, 0.006\}$ for the COM and stretch mode after 30 repeatitions of Raman sideband cooling [39]. Optical pumping prepares both ions in the $|F = 2, m_F = 2\rangle$ atomic state. We then apply a global composite microwave π-pulse to initialize to the $|\uparrow\uparrow\rangle$ state [95]. We set the laser and microwave intensities such that $\Omega_s = 2\pi \times 17.7$ kHz and $\Omega_d = 2\pi \times 1.52$ kHz; and set $\delta = 2\pi \times 27.1$ kHz. We simultaneously apply microwaves and laser beams for a variable duration t, followed by detection pulses. We observe coherent Rabi flopping between the $|\uparrow\uparrow\rangle$ and $|T\rangle$ states as shown in Fig. 7.2, where the populations in the $|\uparrow\uparrow\rangle$, $|T\rangle$, and $|\downarrow\downarrow\rangle$ are determined as described in Sec. 3.4.

We observe a maximal fidelity of the $|T\rangle$ state of 0.980(2) at a duration of t_π =116 μs,[2] matching to the theoretical prediction of $t_\pi = \pi/(2\sqrt{2}\Omega_d)$. Several effects lead to imperfect preparation of the $|T\rangle$ state in our experiment. (1) Spontaneous emission from laser-excited electronic states, which projects the spin state to product states. Through simulation we estimate the

---

[2] In the experiment, we turn on/off the laser beams approximately 0.4 μs before/after the microwave field. Here we only refer to durations when the laser beams and microwave field are applied simultaneously.

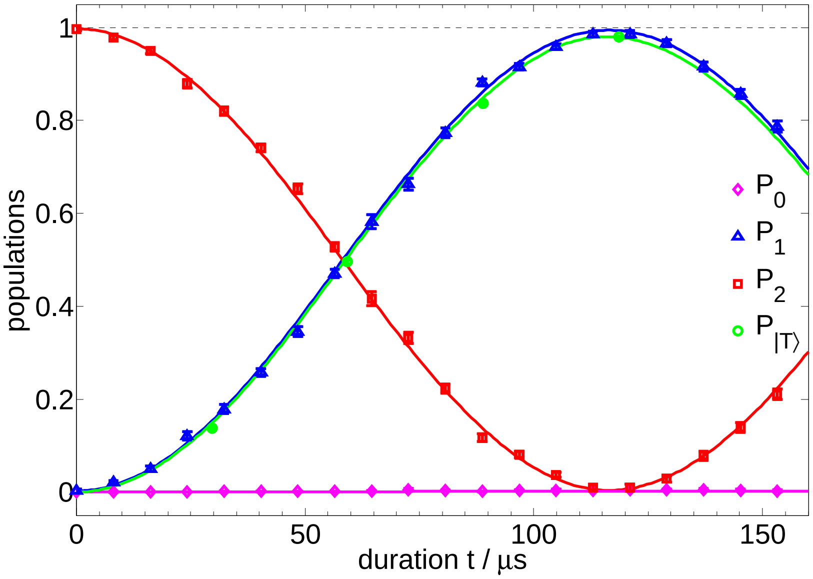

Figure 7.2: Two ion population evolution for confined dynamics with microwave and sideband excitations applied simultaneously. Population mainly evolves between the $|\uparrow\uparrow\rangle$ and the $|T\rangle$ state, while other states have very small populations. The pink diamonds, blue triangles, red squares and green circles represent the measured populations of states with all spins down, one spin up, two spins up and the $|T\rangle$ state, respectively. The difference between P_1 and $P_{|T\rangle}$ is due to the populations in the $|S\rangle$ state. The solid lines shows the results of the numerical simulation taking into account known experimental imperfections, with the same coloring convention as for the measured populations. The black dashed line shows unit population. The error bars for $P_{|T\rangle}$ state are indicated by the size of the symbols. All error bars are from data resampling of a maximum likelihood analysis.

reduction of the maximal $|T\rangle$ state caused by this effect is approximately 0.008. This infidelity can be reduced by tuning the laser frequencies further from the excited states at the cost of reduced coupling strength, which may be compensated using increased laser power [46]. Another potential possibility would be to use a magnetic-field gradient to directly couple the spins to the motion instead of using lasers [86, 136]. (2) Imperfect ground state cooling. The $|\uparrow\uparrow, n \neq 0\rangle$ state is not a dark state of the laser interaction and will be coupled to other states. We estimate this infidelity to be less than 0.006. In simulations of thermal states with mean motional occupation $\bar{n} \in \{0, 0.05\}$, the infidelity of the scheme is approximately equal to $\bar{n}$. This infidelity could be reduced if the lasers were set to a frequency difference near $\omega_0 + 2\omega_s \pm \delta'$ such that they only couple states separated by two motional quanta. In this case the scheme will work as long as the motional mode is prepared in either the $|n=0\rangle$ or $|n=1\rangle$ state, however, the corresponding Rabi rate will be smaller by a factor of the Lamb-Dicke parameter. Ambient heating of the motional mode can cause extra infidelities; however, we apply the sideband near the resonance of the stretch mode, which is insensitive to uniform electric field noise and therefore has a low heating rate, leading to a negligible infidelity. (3) Imperfect initialization of the $|\uparrow\uparrow\rangle$ spin state. This can be due to imperfect optical pumping to the initial $|2,2\rangle$ states or state-preparation π-pulses. We estimate this infidelity to be less than 0.002. (4) Not satisfying the condition $\Omega_s \gg \Omega_d$. In this case, off-resonant excitations from the $|T,0\rangle$ state to the $\{|\downarrow\downarrow, n=0\rangle, |S, n=1\rangle$ and $|\uparrow\uparrow, n=2\rangle\}$ states will play a role. In simulations with $\Omega_s/\Omega_d \approx 12$, we observe a reduction in the maximal value of the $|T\rangle$ state population of 0.0096 due to this effect. This infidelity can be reduced by making the ratio larger, which requires reducing the Rabi rate of the microwaves or increasing the laser power. In both cases this will lead to increased infidelity due to spontaneous emission. Thus, for a given spontaneous emission rate, there is an optimal Ω_s/Ω_d, which is around 12 for our conditions. In Fig. 7.2, we plot the numerical simulation as a solid line in Fig. 7.2 and find good agreement with the data. Detailed theoretical modeling and analysis of the infidelity sources have been done by F. Reiter and A. S. Sørensen [158].

7.3 Two ion implementation with a composite pulse sequence

The evolution is ideally unitary and thus the state amplitudes outside the intended subspace can in principle be recovered. To demonstrate this, we apply a suitable composite pulse pair which allows us to return the population of the undesired states $|\downarrow\downarrow, n=0\rangle$, $|S, n=1\rangle$ and $|\uparrow\uparrow, n=2\rangle$ into the isolated subspace and thereby increase the population of $|T\rangle$. The idea of the composite pulse sequence is originated from an observation that the optimal confinement of Hilbert space can be achieved for both $\delta = \pm\sqrt{\frac{7}{3}}\Omega_s$ and any value of ϕ. Thus switching the sign of δ and/or ϕ during the evolution would not heavily affect the dynamics within the confined subspace, however the dynamics involving the undesired states are significantly affected. To construct the composite pulse, for simplicity we only consider a two-segment sequence, where the signs of δ and/or ϕ are flipped between the two segments. Numerically we find that it works best to switch the sign of both δ and ϕ at $\frac{1}{3}$ of the π time for the $|\uparrow\uparrow\rangle \to |T\rangle$ transition [158]. Thus we split the laser pulse into two segments of duration t_1 and t_2, flipping the sign of δ and changing the laser phase by π at t_1. We set $\Omega_s = 2\pi \times 17.4$ kHz, $\Omega_d = 2\pi \times 2.55$ kHz, $\delta_1 = -\delta_2 = 2\pi \times 26.8$ kHz, $t_1 = 25.4$ μs, and $t_2 = 47.3$ μs to obtain a $|T\rangle$ state population of 0.992(2). Fig. 7.3 shows the population evolution during the composite pulse sequence, in agreement with numerical simulations (solid lines). Higher fidelity is achieved despite weaker isolation for $\Omega_s/\Omega_d \approx 7$. Reducing Ω_s/Ω_d has the beneficial effect of reducing spontaneous emission infidelity to 0.0048, with negligible infidelity from the finite ratio of Ω_s/Ω_d. Other infidelities are less than 0.002 from state preparation and detection, and less than 0.005 from initial cooling.

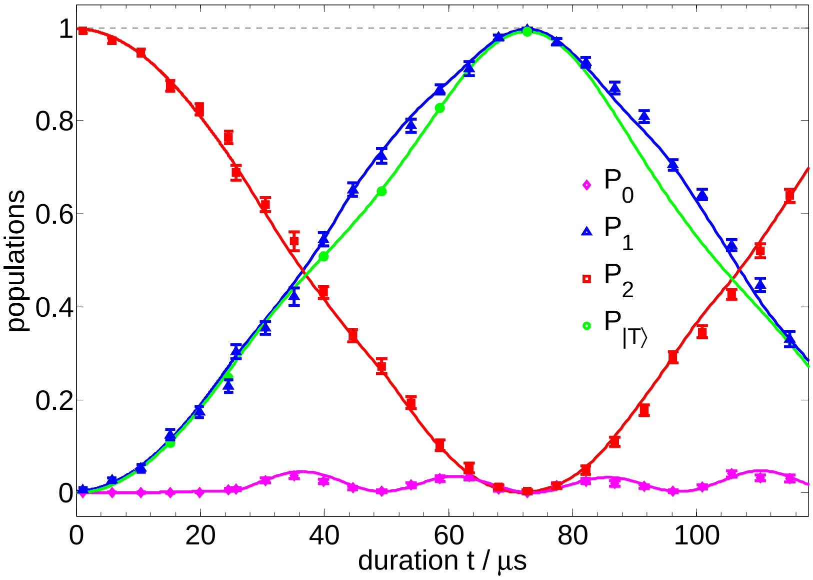

Figure 7.3: State evolution for confined dynamics of two trapped ions using a composite pulse sequence. Similar to Fig. 7.2, populations are mainly confined to the $|\uparrow\uparrow\rangle$ and $|T\rangle$ states. The coloring and labeling conventions are the same as Fig. 7.2. The laser phase and detuning are flipped 25.4 μs after the start of the experiment. Note that the oscillations of $|\downarrow\downarrow\rangle$ are enhanced at $t > 25.4$ μs; however the maximal population of $|T\rangle$ state is increased compared to the single pulse used for the data in Fig. 7.2. All error bars are from data resampling of a maximum likelihood analysis.

7.4 Three ion implementation

We also demonstrate the confined dynamics on three $^9\text{Be}^+$ ions. We tune the laser frequency close to the center-of-mass (COM) mode sideband, which has equal mode amplitudes on each ion. Similar to the case of two ions, we set the center ion equilibrium position to zero, and the outer ions' positions are $\pm z'$. Thus the sideband interaction can be expressed as

$$H'_s = \hbar\Omega'_s(e^{i|\Delta\mathbf{k}|z'}\sigma_1^- + \sigma_2^- + e^{-i|\Delta\mathbf{k}|x'}\sigma_3^-)ae^{-i\delta' t} + H.C., \tag{7.4}$$

where δ' is the detuning from the sideband resonance. We adjust the inter-ion spacing x' near $M'\frac{2\pi}{|\Delta\mathbf{k}|}$, here with $M' = 15 + \frac{1}{3}$. With this we obtain a sideband interaction

$$H'_s = \hbar\Omega'_s(e^{i2\pi/3}\sigma_1^- + \sigma_2^- + e^{-i2\pi/3}\sigma_3^-)ae^{-i\delta' t} + H.C.. \tag{7.5}$$

The microwave coupling can be expressed with the Hamiltonian

$$\begin{aligned} H'_d &= \hbar\Omega_d \sum_{i=1,2,3} \sigma_i^x \\ &= \sqrt{3}\Omega_d(|\uparrow\uparrow\uparrow\rangle\langle W| + \sqrt{3}|W\rangle\langle\overline{W}| + |\overline{W}\rangle\langle\downarrow\downarrow\downarrow| \\ &\quad - |W_{\text{ac}}\rangle\langle\overline{W_{\text{ac}}}| - |W_{\text{c}}\rangle\langle\overline{W_{\text{c}}}|) + H.C., \end{aligned} \tag{7.6}$$

where Ω_d is the single-ion Rabi rate, and $|\overline{W}\rangle = \frac{|\uparrow\downarrow\downarrow\rangle+|\downarrow\uparrow\downarrow\rangle+|\downarrow\downarrow\uparrow\rangle}{\sqrt{3}}$; and the asymmetric "cyclic" states $|W_{\text{c}}\rangle = \frac{e^{i2\pi/3}|\uparrow\uparrow\downarrow\rangle+|\uparrow\downarrow\uparrow\rangle+e^{-i2\pi/3}|\downarrow\uparrow\uparrow\rangle}{\sqrt{3}}$, the "anti-cyclic" $|W_{\text{ac}}\rangle = \frac{e^{-i2\pi/3}|\uparrow\uparrow\downarrow\rangle+|\uparrow\downarrow\uparrow\rangle+e^{i2\pi/3}|\downarrow\uparrow\uparrow\rangle}{\sqrt{3}}$. The definition of $|\overline{W_{\text{c}}}\rangle$ and $|\overline{W_{\text{ac}}}\rangle$ are similar except that the individual spin directions are reversed.

Thus the sideband interaction shifts the energy of the $|\overline{W}\rangle$ state out of resonance, but does not couple to the $|W\rangle$ and $|\uparrow\uparrow\uparrow\rangle|n = 0\rangle$ states. Compared to H_s in the two ion case, the three ion case is special because with detuning $\delta' = 0$, H'_s is sufficient to shift $|\overline{W}, n = 0\rangle$ state out of resonance, by coupling it to only the cyclic asymmetric state $|W_{\text{c}}\rangle|1\rangle$. Thus with $\Omega'_s \gg \Omega_d$, and cooling of the axial modes to near the ground state, the weak microwave excitation only couples the initial state to the $|W\rangle$ state, while further coupling to $|\overline{W}\rangle$ state is off resonance. Similar to the two-ion case, the maximum population of the $|W\rangle$ state is obtained at the duration of $\pi/(2\sqrt{3}\Omega_d)$.

After ground state cooling and preparing the ions in the $|{\uparrow\uparrow\uparrow}\rangle$ state we apply the sideband interaction and resonant microwave radiation to couple the Dicke states. We set the sideband and microwave Rabi rate $\Omega_s' = 2\pi \times 17.1$ kHz and $\Omega_d = 2\pi \times 1.22$ kHz. We denote population for i spins in the $|{\uparrow}\rangle$ state as P_i, i= 0-3. We observe flopping between the $|{\uparrow\uparrow\uparrow}\rangle$ and $|W\rangle$ states, in agreement with numerical simulations. We obtain the $|W\rangle$ state fidelity to be 0.905(5) after a duration of 114.1 μs.

We determine that the infidelity of $|W\rangle$ state has contributions of 0.016 from imperfect isolation, 0.010 from spontaneous emission and less than 0.005 from state preparation. Since we need to apply the scheme on the common mode for the three ions, this mode experiences significant ambient heating rate, which also results in poorer ground state cooling. We estimate the heating rate to be approximately 136 quanta/s, giving an infidelity of 0.011 and with initial $\bar{n} \approx 0.02$, giving an infidelity of 0.018.

Also, due to the finite laser beam waist across the ions, the outer ions will experience different Stark shifts from the center ion, in turn leading to slightly different microwave resonant frequencies. We estimate the infidelity from this effect to be 0.023. This effect can be mitigated by use of laser beams with larger beam waists, and/or reduced spacing between the ions. Combining all known effects, simulation predicts a maximum population of $|W\rangle$ state population of 0.915, approximately agreed with the experimental result. Since the infidelity for three ions is dominated by other sources than considered in Sec. 4, we expect the gain from using a composite pulse to be limited and we do not investigate it here.

For more than three ions in a chain, simulations indicate that unwanted dark states appear so that straightforward application of the sideband interaction does not yield an effective two-level system between the first two Dicke states. However, by using a combination of multiple sideband laser interactions and engineering the phases of the sideband couplings on each ion, the scheme may be scaled up to isolate an effective an effective two-level system. Our scheme can be generalized to other experimental platforms, for example superconducting qubits and atoms in a cavity, since the interaction Hamiltonians are in the same form.

Chapter 8

Conclusion

In this thesis, we have mainly described two novel methods of generating entanglement, with subspace engineering and including dissipation to the system. Both of these methods use laser sideband interactions to induce strong energy shifts to reshape the system evolution determined by the symmetry of the coupling across the ions, which provides certain robustness to fluctuations of laser intensity, laser frequency and trapping frequency. Compared to the conventional entangling quantum logic gates, this robustness may help to improve fidelities in the future. Since the world-record entangling gate fidelity with trapped ions using Raman lasers is currently 0.999(1) [125], we can see that our implementations still have lower fidelities. The primary reason is that in our schemes we need to have strong laser sidebands compared with the evolutions which introduces more spontaneous emission infidelities. In other systems this problem can be suppressed. For example consider the scheme implemented with two $^{171}\mathrm{Yb}^{+}$ ions, where very low spontaneous emission can be achieved [159, 160]. Given the same trapping potential as in our experiment, the spontaneous emission infidelity may be suppressed by roughly an order of magnitude using a high intensity mode-locked pulsed laser operating in the weak pulse regime [159, 160]. In this case, for the subspace engineering scheme, simulation predicts an infidelity of the $|T\rangle$ state preparation below 0.001 with weaker microwave drive. In this case the simple scheme without composite pulses would be sufficient to achieve high fidelity, with robustness to fluctuations.

The subspace engineering described here relies on high-fidelity ground state cooling, which is not an issue for the state-of-the-art Mølmer-Sørensen gate as long as the Lamb-Dicke limit is satisfied [50]. Despite these drawbacks of the scheme, we still see that for the first demonstration of the technique with subspace engineering we have already achieved fidelity up to 0.99. Future schemes combining these techniques to more tasks of quantum information processing could be very interesting, not limited to using Raman laser sidebands to induce entanglement or even not limited to trapped ion systems. The idea of our scheme is more naturally extendable to systems with strong couplings, which may be noisy but do not induce projective spin errors.

For the dissipative entanglement, we have introduced dissipation as part of the processes of generating entanglement. Robustness is inherent for the dissipations we introduce purposely; however there was still uncontrolled dissipation such as spontaneous emission, and at the time of the experiment, the beam pointing fluctuations. The optimal case for generation of entangled state by dissipation is that major dissipation sources are all accounted as part of the scheme. Indeed, our scheme was originally proposed for atoms in optical cavity [132], where the photon loss from cavity is used as part of the dissipative process as a fundamental loss mechanism for that system. In our case, this photon loss process is replaced by sympathetic cooling - a controlled phonon loss process.

Thanks for reading my thesis! If you find this thesis interesting or have questions or remarks, please send me an email at yiheng.lin@colorado.edu or yihenglin.ustc@gmail.com.

Bibliography

[1] J. J. Bollinger, D. J. Heizen, W. M. Itano, S. L. Gilbert, and D. J. Wineland. A 303-mhz frequency standard based on trapped be/sup+/ions. Instrumentation and Measurement, IEEE Transactions on, 40(2):126–128, 1991.

[2] D. Kielpinski, C. Monroe, and D. J. Wineland. Architecture for a large-scale ion-trap quantum computer. Nature, 417(6890):709–11, June 2002.

[3] J. D. Jost. Entangled mechanical oscillators. PhD thesis, University of Colorado, Boulder, 2010.

[4] R. B. Blakestad, C. Ospelkaus, A. P. VanDevender, J. M. Amini, J. Britton, D. Leibfried, and D. J. Wineland. High-fidelity transport of trapped-ion qubits through an x-junction trap array. Phys. Rev. Lett., 102(15):153002, 2009.

[5] B. R. Coherent Ion Transport in a Multi-electrode Trap Array. PhD thesis, University of Colorado, Boulder, 2015.

[6] G. D. Boyd and D. A. Kleinman. Parametric interaction of focused gaussian light beams. J. Appl. Phys., 39(8):3597–3639, 1968.

[7] Y. Colombe, D. H. Slichter, A. C. Wilson, D. Leibfried, and D. J. Wineland. Single-mode optical fiber for high-power, low-loss uv transmission. Opt. Express, 22(16):19783–19793, 2014.

[8] G. Morigi. Cooling atomic motion with quantum interference. Phys. Rev. A, 67(3):033402, March 2003.

[9] G. Morigi, J. Eschner, and C. H. Keitel. Ground state laser cooling using electromagnetically induced transparency. Phys. Rev. Lett., 85(21):4458–4461, November 2000.

[10] G. E. Moore. Cramming more components onto integrated circuits. Proceedings of the IEEE, 86(1):82–85, 1998.

[11] I. L. Chuang and M. A. Nielsen. Quantum computing and quantum information, 2000.

[12] D. Deutsch and R. Jozsa. Rapid solution of problems by quantum computation. In Proceedings of the Royal Society of London A: Mathematical, Physical and Engineering Sciences, volume 439, pages 553–558. The Royal Society, 1992.

[13] P. W. Shor. Algorithms for quantum computation: Discrete logarithms and factoring. In Foundations of Computer Science, 1994 Proceedings., 35th Annual Symposium on, pages 124–134. IEEE, 1994.

[14] S. Lloyd. Universal quantum simulators. Science, 273(5278):1073–1078, August 1996.

[15] J. I. Cirac and P. Zoller. Goals and opportunities in quantum simulation. Nature Phys., 8(4):264–266, 2012.

[16] I. Bloch, J. Dalibard, and S. Nascimbène. Quantum simulations with ultracold quantum gases. Nature Phys., 8(4):267–276, 2012.

[17] R. Blatt and C. F. Roos. Quantum simulations with trapped ions. Nature Phys., 8(4):277–284, April 2012.

[18] A. Aspuru-Guzik and P. Walther. Photonic quantum simulators. Nature Phys., 8(4):285–291, 2012.

[19] H. Walther, B. T. Varcoe, B.-G. Englert, and T. Becker. Cavity quantum electrodynamics. Rep. Prog. Phys., 69(5):1325, 2006.

[20] M. Saffman, T. G. Walker, and K. Mølmer. Quantum information with rydberg atoms. Rev. Mod. Phys., 82(3):2313, 2010.

[21] P. S. Jessen and R. Stock. Quantum information processing with trapped neutral atoms. Quantum Information Processing, 3(1-5):91–103, 2004.

[22] D. J. Wineland, C. Monroe, W. M. Itano, D. Leibfried, B. E. King, and D. M. Meekhof. Experimental issues in coherent quantum-state manipulation of trapped atomic ions. J. Res. Natl. Inst. Stand. Technol., 103(3):259, May 1998.

[23] P. Kok, W. J. Munro, K. Nemoto, T. C. Ralph, J. P. Dowling, and G. J. Milburn. Linear optical quantum computing with photonic qubits. Rev. Mod. Phys., 79(1):135, 2007.

[24] T. E. Northup and R. Blatt. Quantum information transfer using photons. Nature Photonics, 8(5):356–363, 2014.

[25] Y. Makhlin, G. Schön, and A. Shnirman. Quantum-state engineering with josephson-junction devices. Rev. Mod. Phys., 73(2):357, 2001.

[26] Preskill. lecture notes for course quantum computation, http://www.theory.caltech.edu/people/preskill/ph229/.

[27] M. A. Nielsen and I. L. Chuang. Quantum computation and quantum information. Cambridge University Press, Cambridge, 2011.

[28] J. S. Bell. On the einstein-podolsky-rosen paradox. Physics, 1(3):195–200, 1964.

[29] J. F. Clauser, M. A. Horne, A. Shimony, and R. A. Holt. Proposed experiment to test local hidden-variable theories. Phys. Rev. Lett., 23(15):880, 1969.

[30] J. S. Bell. Introduction to the hidden-variable question, in: Foundations of Quantum Mechanics: Rendiconti della Scuola Internazionale di Fisica “Enrico Fermi”. Academic Press, New York, 1971.

[31] J. F. Clauser and A. Shimony. Bell's theorem. experimental tests and implications. Rep. Prog. Phys., 41(12):1881, 1978.

[32] D. Leibfried, M. D. Barrett, T. Schaetz, J. Britton, J. Chiaverini, W. M. Itano, J. D. Jost, C. Langer, and D. J. Wineland. Toward heisenberg-limited spectroscopy with multiparticle entangled states. Science, 304(5676):1476–1478, 2004.

[33] Z. Chen, J. G. Bohnet, S. R. Sankar, J. Dai, and J. K. Thompson. Conditional spin squeezing of a large ensemble via the vacuum rabi splitting. Phys. Rev. Lett., 106(13):133601, 2011.

[34] P. O. Schmidt, T. Rosenband, C. Langer, W. M. Itano, J. C. Bergquist, and D. J. Wineland. Spectroscopy using quantum logic. Science, 309(5735):749–52, July 2005.

[35] D. B. Hume, T. Rosenband, and D. J. Wineland. High-fidelity adaptive qubit detection through repetitive quantum nondemolition measurements. Phys. Rev. Lett., 99(12):120502, 2007.

[36] A. Louchet-Chauvet, J. Appel, J. J. Renema, D. Oblak, N. Kjaergaard, and E. S. Polzik. Entanglement-assisted atomic clock beyond the projection noise limit. New J. Phys., 12(6):065032, 2010.

[37] C. Monroe, R. Raussendorf, A. Ruthven, K. R. Brown, P. Maunz, L.-M. Duan, and J. Kim. Large-scale modular quantum-computer architecture with atomic memory and photonic interconnects. Phys. Rev. A, 89(2):022317, 2014.

[38] U. Warring, C. Ospelkaus, Y. Colombe, R. Jördens, D. Leibfried, and D. Wineland. Individual-ion addressing with microwave field gradients. Phys. Rev. Lett., 110(17):173002, 2013.

[39] C. Monroe, D. M. Meekhof, B. E. King, W. M. Itano, and D. J. Wineland. Demonstration of a fundamental quantum logic gate. Phys. Rev. Lett., 75(25):4714–4717, December 1995.

[40] K. R. Brown, C. Ospelkaus, Y. Colombe, A. Wilson, D. Leibfried, and D. J. Wineland. Coupled quantized mechanical oscillators. Nature, 471(7337):196–199, 2011.

[41] A. C. Wilson, Y. Colombe, K. R. Brown, E. Knill, D. Leibfried, and D. J. Wineland. Tunable spin-spin interactions and entanglement of ions in separate potential wells. Nature, 512(7512):57–60, 2014.

[42] J. P. Gaebler, A. M. Meier, T. R. Tan, R. Bowler, Y. Lin, D. Hanneke, J. Jost, J. Home, E. Knill, D. Leibfried, and D. J. Wineland. Randomized benchmarking of multiqubit gates. Phys. Rev. Lett., 108(26):260503, 2012.

[43] J. Benhelm, G. Kirchmair, C. F. Roos, and R. Blatt. Towards fault-tolerant quantum computing with trapped ions. Nature Phys., 4(6):463–466, 2008.

[44] D. J. Larson, J. C. Bergquist, J. J. Bollinger, W. M. Itano, and D. J. Wineland. Sympathetic cooling of trapped ions: A laser-cooled two-species nonneutral ion plasma. Phys. Rev. Lett., 57(1):70, 1986.

[45] R. Bowler, J. Gaebler, Y. Lin, T. Tan, D. Hanneke, J. D. Jost, J. P. Home, D. Leibfried, and D. J. Wineland. Coherent diabatic ion transport and separation in a multizone trap array. Phys. Rev. Lett., 109(8):080502, 2012.

[46] R. Ozeri, W. Itano, R. Blakestad, J. Britton, J. Chiaverini, J. Jost, C. Langer, D. Leibfried, R. Reichle, S. Seidelin, J. H. Wesenberg, and D. J. Wineland. Errors in trapped-ion quantum gates due to spontaneous photon scattering. Phys. Rev. A, 75(4):042329, 2007.

[47] J. I. Cirac and P. Zoller. Quantum Computations with Cold Trapped Ions. Phys. Rev. Lett., 74(20):4091–4094, May 1995.

[48] K. Mølmer and A. Sørensen. Multiparticle entanglement of hot trapped ions. Phys. Rev. Lett., 82(9):1835, 1999.

[49] E. Solano, R. L. de Matos Filho, and N. Zagury. Deterministic bell states and measurement of the motional state of two trapped ions. Phys. Rev. A, 59(4):R2539, 1999.

[50] A. Sørensen and K. Mølmer. Quantum computation with ions in thermal motion. Phys. Rev. Lett., 82(9):1971, 1999.

[51] G. J. Milburn, S. Schneider, and D. F. V. James. Ion trap quantum computing with warm ions. Fortschritte der Physik, 48(9-11):801–810, 2000.

[52] D. Leibfried, B. DeMarco, V. Meyer, D. Lucas, M. Barrett, J. Britton, W. Itano, B. Jelenković, C. Langer, T. Rosenband, and D. J. Wineland. Experimental demonstration of a robust, high-fidelity geometric two ion-qubit phase gate. Nature, 422(6930):412–415, 2003.

[53] A. Bermudez, P. O. Schmidt, M. B. Plenio, and A. Retzker. Robust trapped-ion quantum logic gates by continuous dynamical decoupling. Phys. Rev. A, 85(4):040302, 2012.

[54] V. Frerichs and A. Schenzle. Quantum zeno effect without collapse of the wave packet. Phys. Rev. A, 44(3):1962, 1991.

[55] P. Facchi and S. Pascazio. Quantum zeno subspaces. Phys. Rev. Lett., 89(8):080401, 2002.

[56] P. Facchi and S. Pascazio. Quantum zeno dynamics: mathematical and physical aspects. J. Phys. A, 41(49):493001, 2008.

[57] J. M. Chow, L. DiCarlo, J. M. Gambetta, A. Nunnenkamp, L. S. Bishop, L. Frunzio, M. H. Devoret, S. M. Girvin, and R. J. Schoelkopf. Detecting highly entangled states with a joint qubit readout. Phys. Rev. A, 81:062325, June 2010.

[58] K. R. Brown, A. C. Wilson, Y. Colombe, C. Ospelkaus, A. Meier, E. Knill, D. Leibfried, and D. J. Wineland. Single-qubit-gate error below 10^-4 in a trapped ion. Phys. Rev. A, 84(3):030303, 2011.

[59] T. P. Harty, D. T. C. Allcock, C. J. Ballance, L. Guidoni, H. A. Janacek, N. M. Linke, D. N. Stacey, and D. M. Lucas. High-fidelity preparation, gates, memory, and readout of a trapped-ion quantum bit. Phys. Rev. Lett., 113(22):220501, 2014.

[60] H. Krauter, C. A. Muschik, K. Jensen, W. Wasilewski, J. M. Petersen, J. I. Cirac, and E. S. Polzik. Entanglement generated by dissipation and steady state entanglement of two macroscopic objects. Phys. Rev. Lett., 107:080503, Aug 2011.

[61] J. T. Barreiro, M. Müller, P. Schindler, D. Nigg, T. Monz, M. Chwalla, M. Hennrich, C. F. Roos, P. Zoller, and R. Blatt. An open-system quantum simulator with trapped ions. Nature, 470(7335):486–491, 2011.

[62] S. Shankar, M. Hatridge, Z. Leghtas, K. M. Sliwa, A. Narla, U. Vool, S. M. Girvin, L. Frunzio, M. Mirrahimi, and M. H. Devoret. Autonomously stabilized entanglement between two superconducting quantum bits. Nature, 504(7480):419–422, 2013.

[63] D. Leibfried, R. Blatt, C. Monroe, and D. J. Wineland. Quantum dynamics of single trapped ions. Rev. Mod. Phys., 75(1):281, 2003.

[64] W. Paul. Electromagnetic traps for charged and neutral particles. Rev. Mod. Phys., 62(3):531, 1990.

[65] P. K. Ghosh. Ion Traps. Clarendon Press, 1995.

[66] M. D. Hughes, B. Lekitsch, J. A. Broersma, and W. K. Hensinger. Microfabricated ion traps. Contemporary Physics, 52(6):505–529, 2011.

[67] A. P. VanDevender, Y. Colombe, J. Amini, D. Leibfried, and D. J. Wineland. Efficient fiber optic detection of trapped ion fluorescence. Phys. Rev. Lett., 105(2):023001, 2010.

[68] C. L. D. A. J. M. W. K. D. S. C. P. C.-S. H. H. K. T. F. D. B. K. R. H. A. W. . S. R. E. Merrill, J. T.; Volin. Demonstration of integrated microscale optics in surface-electrode ion traps. New J. Phys., 13(10):103005, 2011.

[69] F. Schmidt-Kaler, H. Häffner, S. Gulde, M. Riebe, G. P. T. Lancaster, T. Deuschle, C. Becher, W. Hänsel, J. Eschner, C. F. Roos, and R. Blatt. How to realize a universal quantum gate with trapped ions. Appl. Phys. B, 77(8):789–796, 2003.

[70] M. A. Rowe, A. Ben-Kish, B. Demarco, D. Leibfried, V. Meyer, J. Beall, J. Britton, J. Hughes, W. M. Itano, B. Jelenkovic, C. Langer, T. Rosenband, and D. J. Wineland. Transport of quantum states and separation of ions in a dual rf ion trap. Quantum Inf. Comput., 2(4):257–271, 2002.

[71] B. R.B. Transport of Trapped-Ion Qubits within a Scalable Quantum Processor. PhD thesis, Department of Physics, University of Colorado, 2010.

[72] S. Jefferts, C. Monroe, E. Bell, and D. Wineland. Coaxial-resonator-driven rf (paul) trap for strong confinement. Physical Review A, 51(4):3112, 1995.

[73] C. Langer, R. Ozeri, J. D. Jost, J. Chiaverini, B. DeMarco, A. Ben-Kish, R. Blakestad, J. Britton, D. B. Hume, W. M. Itano, D. Leibfried, R. Reichle, T. Rosenband, T. Schaetz, P. O. Schmidt, and D. J. Wineland. Long-Lived Qubit Memory Using Atomic Ions. Phys. Rev. Lett., 95(6):060502, August 2005.

[74] J. D. Jost, J. P. Home, J. M. Amini, D. Hanneke, R. Ozeri, C. Langer, J. J. Bollinger, D. Leibfried, and D. J. Wineland. Entangled mechanical oscillators. Nature, 459(7247):683–685, 2009.

[75] J. P. Home, D. Hanneke, J. D. Jost, J. M. Amini, D. Leibfried, and D. J. Wineland. Complete methods set for scalable ion trap quantum information processing. Science, 325(5945):1227–30, September 2009.

[76] D. Hanneke, J. P. Home, J. D. Jost, J. M. Amini, D. Leibfried, and D. J. Wineland. Realization of a programmable two-qubit quantum processor. Nature Phys., 6(1):13–16, 2010.

[77] T. R. Tan, J. P. Gaebler, R. Bowler, J. D. Lin, Y Gaebler, D. Leibfried, and D. J. Wineland. Demonstration of a dressed-state phase gate for trapped ions. Phys. Rev. Lett., 110(26):263002, 2013.

[78] Y. Lin, J. Gaebler, T. R. Tan, R. Bowler, J. D. Jost, D. Leibfried, and D. J. Wineland. Sympathetic electromagnetically-induced-transparency laser cooling of motional modes in an ion chain. Phys. Rev. Lett., 110(15):153002, 2013.

[79] Y. Lin, J. P. Gaebler, F. Reiter, T. R. Tan, R. Bowler, A. S. Sørensen, D. Leibfried, and D. J. Wineland. Dissipative production of a maximally entangled steady state of two quantum bits. Nature, 504(7480):415–418, 2013.

[80] A. Kramida and W. C. Martin. A compilation of energy levels and wavelengths for the spectrum of neutral beryllium (be i). Journal of Physical and Chemical Reference Data, 26(5):1185–1194, 1997.

[81] W. C. Martin and R. Zalubas. Energy levels of magnesium, mg i through mg xii. Journal of Physical and Chemical Reference Data, 9(1):1–58, 1980.

[82] N. Kjærgaard, L. Hornekær, A. Thommesen, Z. Videsen, and M. Drewsen. Isotope selective loading of an ion trap using resonance-enhanced two-photon ionization. Appl. Phys. B, 71(2):207–210, 2000.

[83] J. W. Britton, B. C. Sawyer, A. C. Keith, C.-C. J. Wang, J. K. Freericks, H. Uys, M. J. Biercuk, and J. J. Bollinger. Engineered two-dimensional ising interactions in a trapped-ion quantum simulator with hundreds of spins. Nature, 484(7395):489–492, 2012.

[84] B. C. Sawyer, J. G. Bohnet, J. W. Britton, and J. J. Bollinger. Reversing hydride-ion formation in quantum-information experiments with be+. Phys. Rev. A, 91(1):011401, 2015.

[85] P. Huang and D. Leibfried. Achromatic catadioptric microscope objective in deep ultraviolet with long working distance. In Optical Science and Technology, the SPIE 49th Annual Meeting, pages 125–133. International Society for Optics and Photonics, 2004.

[86] N. Timoney, I. Baumgart, M. Johanning, A. Varón, M. Plenio, A. Retzker, and C. Wunderlich. Quantum gates and memory using microwave-dressed states. Nature, 476(7359):185–188, 2011.

[87] C. E. Langer. High fidelity quantum information processing with trapped ions. PhD thesis, University of Colorado, 2006.

[88] J. J. Bollinger, J. S. Wells, D. J. Wineland, and W. M. Itano. Hyperfine structure of the 2 p p 1 2 2 state in be+ 9. Phys. Rev. A, 31(4):2711, 1985.

[89] D. J. Wineland, J. J. Bollinger, and W. M. Itano. Laser-fluorescence mass spectroscopy. Phys. Rev. Lett., 50(9):628, 1983.

[90] G. K. Woodgate. ELEMENTARY ATOMIC STRUCTURE. Oxford : Clarendon press, 1992.

[91] O. Poulsen, T. Andersen, and N. J. Skouboe. Fast-beam, zero-field level-crossing measurements of radiative lifetimes, fine and hyperfine structures in excited states of ionic and neutral beryllium. J. Phys. B, 8(9):1393, 1975.

[92] C. Monroe, D. M. Meekhof, B. E. King, and D. J. Wineland. A "schrödinger cat" superposition state of an atom. Science, 272(5265):1131–1136, 1996.

[93] H. J. Metcalf and P. Van der Straten. Laser cooling and trapping. Springer Science & Business Media, New York, 2012.

[94] A. C. Wilson, C. Ospelkaus, A. P. VanDevender, J. A. Mlynek, K. R. Brown, D. Leibfried, and D. J. Wineland. A 750-mw, continuous-wave, solid-state laser source at 313 nm for cooling and manipulating trapped 9be+ ions. Appl. Phys. B, 105(4):741–748, 2011.

[95] M. H. Levitt. Composite pulses. Prog. Nucl. Magn. Reson. Spectrosc., 18(2):61–122, 1986.

[96] H. G. Dehmelt. Bull. Am. Phys. Soc., 20(60), 1975.

[97] B. E. King. Quantum state engineering and information processing with trapped ions. PhD thesis, University of Colorado, 1999.

[98] M. Acton, K.-A. Brickman, P. C. Haljan, P. J. Lee, L. Deslauriers, and C. Monroe. Near-perfect simultaneous measurement of a qubit register. Quantum Inf. Comput., 6(6):465–482, 2006.

[99] J. Rice. Mathematical statistics and data analysis. Cengage Learning, 2006.

[100] M. O. Scully and M. S. Zubairy. Quantum optics. Cambridge university press, Cambridge, UK, 1997.

[101] C. Ospelkaus, Y. Warring, U. and. Colombe, K. R. Brown, J. M. Amini, D. Leibfried, and D. J. Wineland. Microwave quantum logic gates for trapped ions. Nature, 476:181, 2011.

[102] D. F. James and J. Jerke. Effective hamiltonian theory and its applications in quantum information. Canadian Journal of Physics, 85(6):625–632, 2007.

[103] K. E. Cahill and R. J. Glauber. Ordered expansions in boson amplitude operators. Phys. Rev., 177(5):1857, 1969.

[104] D. J. Wineland and W. M. Itano. Laser cooling of atoms. Phys. Rev. A, 20(4):1521, 1979.

[105] C. J. Foot. Atomic physics. OUP Oxford, 2004.

[106] C. Monroe, D. M. Meekhof, B. E. King, S. R. Jefferts, W. M. Itano, D. J. Wineland, and P. Gould. Resolved-sideband raman cooling of a bound atom to the 3d zero-point energy. Phys. Rev. Lett., 75(22):4011–4014, November 1995.

[107] R. Blatt and D. Wineland. Entangled states of trapped atomic ions. Nature, 453(7198):1008–1015, June 2008.

[108] F. Diedrich, J. C. Bergquist, W. Itano, and D. J. Wineland. Laser Cooling to the Zero-Point Energy of Motion. Phys. Rev. Lett., 62(4):403–406, January 1989.

[109] J. Wübbena, S. Amairi, O. Mandel, and P. O. Schmidt. Sympathetic cooling of mixed-species two-ion crystals for precision spectroscopy. Phys. Rev. A, 85(4):043412, April 2012.

[110] C. F. Roos, D. Leibfried, A. Mundt, F. Schmidt-Kaler, J. Eschner, and R. Blatt. Experimental Demonstration of Ground State Laser Cooling with Electromagnetically Induced Transparency. Phys. Rev. Lett., 85(26):5547–5550, December 2000.

[111] F. Schmidt-Kaler, J. Eschner, G. Morigi, C. F. Roos, D. Leibfried, a. Mundt, and R. Blatt. Laser cooling with electromagnetically induced transparency: application to trapped samples of ions or neutral atoms. Appl. Phys. B, 73(8):807–814, December 2001.

[112] S. Webster. Raman Sideband Cooling and Coherent Manipulation of Trapped Ions. PhD thesis, University of Oxford, 2005.

[113] G.-D. Lin, S.-L. Zhu, R. Islam, K. Kim, M.-S. Chang, S. Korenblit, C. Monroe, and L.-M. Duan. Large-scale quantum computation in an anharmonic linear ion trap. Europhys. Lett., 86(6):60004, June 2009.

[114] R. Islam, E. E. Edwards, K. Kim, S. Korenblit, C. Noh, H. Carmichael, G.-D. Lin, L.-M. Duan, C.-C. J. Wang, J. K. Freericks, and C. Monroe. Onset of a quantum phase transition with a trapped ion quantum simulator. Nat. Commun., 2:377, January 2011.

[115] B. C. Sawyer, J. W. Britton, A. C. Keith, C.-C. J. Wang, J. K. Freericks, H. Uys, M. J. Biercuk, and J. J. Bollinger. Spectroscopy and Thermometry of Drumhead Modes in a Mesoscopic Trapped-Ion Crystal Using Entanglement. Phys. Rev. Lett., 108(21):213003, May 2012.

[116] R. Islam, C. Senko, W. C. Campbell, S. Korenblit, J. Smith, A. Lee, E. E. Edwards, C. C. J. Wang, J. K. Freericks, and C. Monroe. Emergence and frustration of magnetism with variable-range interactions in a quantum simulator. Science, 340:583–7, 2013.

[117] B. E. King, C. S. Wood, C. J. Myatt, Q. A. Turchette, D. Leibfried, W. M. Itano, C. Monroe, and D. J. Wineland. Cooling the Collective Motion of Trapped Ions to Initialize a Quantum Register. Phys. Rev. Lett., 81(7):1525–1528, August 1998.

[118] C. F. Roos, T. Monz, K. Kim, M. Riebe, H. Häffner, D. F. V. James, and R. Blatt. Nonlinear coupling of continuous variables at the single quantum level. Phys. Rev. A, 77(4):040302, April 2008.

[119] X. R. Nie, C. F. Roos, and D. F. V. James. Theory of cross phase modulation for the vibrational modes of trapped ions. Physics Letters A, 373(4):422–425, 2009.

[120] T. Kampschulte, W. Alt, S. Manz, M. Martinez-Dorantes, R. Reimann, S. Yoon, D. Meschede, M. Bienert, and G. Morigi. Electromagnetically-induced-transparency control of single-atom motion in an optical cavity. Phys. Rev. A, 89(3):033404, 2014.

[121] K. Xia and J. Evers. Ground state cooling of a nanomechanical resonator in the nonresolved regime via quantum interference. Phys. Rev. Lett., 103(22):227203, 2009.

[122] P. J. Lee, K. A. Brickman, L. Deslauriers, P. C. Haljan, L. M. Duan, and C. Monroe. Phase control of trapped ion quantum gates. J. Opt. B, 7(10):S371, 2005.

[123] K. Kim, M.-S. Chang, S. Korenblit, R. Islam, E. Edwards, J. Freericks, G.-D. Lin, L.-M. Duan, and C. Monroe. Quantum simulation of frustrated ising spins with trapped ions. Nature, 465(7298):590–593, 2010.

[124] B. P. Lanyon, C. Hempel, D. Nigg, M. Müller, R. Gerritsma, F. Zähringer, P. Schindler, J. T. Barreiro, M. Rambach, G. Kirchmair, M. Hennrich, P. Zoller, R. Blatt, and C. F. Roos. Universal digital quantum simulation with trapped ions. Science, 334(6052):57–61, 2011.

[125] C. J. Ballance, T. P. Harty, N. M. Linke, and D. M. Lucas. High-fidelity two-qubit quantum logic gates using trapped calcium-43 ions. arXiv preprint arXiv:1406.5473, 2014.

[126] D. L. Moehring, P. Maunz, S. Olmschenk, K. C. Younge, D. N. Matsukevich, L.-M. Duan, and C. Monroe. Entanglement of single-atom quantum bits at a distance. Nature, 449(7158):68–71, 2007.

[127] D. Hucul, I. V. Inlek, G. Vittorini, C. Crocker, S. Debnath, S. M. Clark, and C. Monroe. Modular entanglement of atomic qubits using photons and phonons. Nature Phys., 2014.

[128] A. Zeilinger, G. Weihs, T. Jennewein, and M. Aspelmeyer. Happy centenary, photon. Nature, 433(7023):230–238, 2005.

[129] J.-W. Pan, Z.-B. Chen, C.-Y. Lu, H. Weinfurter, A. Zeilinger, and M. Żukowski. Multiphoton entanglement and interferometry. Reviews of Modern Physics, 84(2):777, 2012.

[130] J. G. Bohnet, Z. Chen, J. M. Weiner, D. Meiser, M. J. Holland, and J. K. Thompson. A steady-state superradiant laser with less than one intracavity photon. Nature, 484(7392):78–81, 2012.

[131] R. McConnell, C. Bruzewicz, J. Chiaverini, and J. Sage. Reduction of trapped ion anomalous heating by in situ surface plasma cleaning. arXiv preprint arXiv:1505.03844, 2015.

[132] M. J. Kastoryano, F. Reiter, and A. S. Sørensen. Dissipative preparation of entanglement in optical cavities. Phys. Rev. Lett., 106(9):090502, 2011.

[133] F. Reiter, M. J. Kastoryano, and A. S. Sørensen. Driving two atoms in an optical cavity into an entangled steady state using engineered decay. New J. Phys., 14(5):053022, 2012.

[134] G. Lindblad. On the generators of quantum dynamical semigroups. Commun. Math. Phys., 48(2):119–130, 1976.

[135] C. Gardiner and P. Zoller. Quantum noise: a handbook of Markovian and non-Markovian quantum stochastic methods with applications to quantum optics, volume 56. Springer Science & Business Media, 2004.

[136] C. Ospelkaus, U. Warring, Y. Colombe, K. R. Brown, J. M. Amini, D. Leibfried, and D. J. Wineland. Microwave quantum logic gates for trapped ions. Nature, 476(7359):181–184, 2011.

[137] W. Dür, G. Vidal, and J. I. Cirac. Three qubits can be entangled in two inequivalent ways. Phys. Rev. A, 62(6):062314, 2000.

[138] B. Misra and E. C. G. Sudarshan. The zenos paradox in quantum theory. J. Math. Phys., 18(4):756–763, 1977.

[139] S. Maniscalco, F. Francica, R. L. Zaffino, N. L. Gullo, and F. Plastina. Protecting entanglement via the quantum zeno effect. Phys. Rev. Lett., 100(9):090503, 2008.

[140] X.-B. Wang, J. Q. You, and F. Nori. Quantum entanglement via two-qubit quantum zeno dynamics. Phys. Rev. A, 77(6):062339, 2008.

[141] J.-M. Raimond, C. Sayrin, S. Gleyzes, I. Dotsenko, M. Brune, S. Haroche, P. Facchi, and S. Pascazio. Phase space tweezers for tailoring cavity fields by quantum zeno dynamics. Phys. Rev. Lett., 105(21):213601, 2010.

[142] A. W. Chin, S. F. Huelga, and M. B. Plenio. Quantum metrology in non-markovian environments. Phys. Rev. Lett., 109(23):233601, 2012.

[143] A. Smerzi. Zeno dynamics, indistinguishability of state, and entanglement. Phys. Rev. Lett., 109(15):150410, 2012.

[144] D. Burgarth, P. Facchi, V. Giovannetti, H. Nakazato, S. Pascazio, and K. Yuasa. Non-abelian phases from quantum zeno dynamics. Phys. Rev. A, 88(4):042107, 2013.

[145] Y. Li, D. A. Herrera-Martí, and L. C. Kwek. Quantum zeno effect of general quantum operations. Phys. Rev. A, 88(4):042321, 2013.

[146] Y.-R. Zhang and H. Fan. Zeno dynamics in quantum open systems. Sci. Rep., 5, 2015.

[147] B. Zhu, B. Gadway, M. Foss-Feig, J. Schachenmayer, M. L. Wall, K. R. A. Hazzard, B. Yan, S. A. Moses, J. P. Covey, D. S. Jin, Y. J., M. Holland, and A. M. Rey. Suppressing the loss of ultracold molecules via the continuous quantum zeno effect. Phys. Rev. Lett., 112(7):070404, 2014.

[148] F. Schäfer, I. Herrera, S. Cherukattil, C. Lovecchio, F. Cataliotti, F. Caruso, and A. Smerzi. Experimental realization of quantum zeno dynamics. Nat. Commun., 5:3194, 2014.

[149] A. Signoles, A. Facon, D. Grosso, I. Dotsenko, S. Haroche, J.-M. Raimond, M. Brune, and S. Gleyzes. Confined quantum zeno dynamics of a watched atomic arrow. Nature Phys., 10:715–719, 2014.

[150] Y.-Y. Jau, A. M. Hankin, T. Keating, I. H. Deutsch, and G. W. Biedermann. Entangling atomic spins with a strong rydberg-dressed interaction. arXiv preprint arXiv:1501.03862, 2015.

[151] L. Bretheau, P. Campagne-Ibarcq, E. Flurin, F. Mallet, and B. Huard. Quantum dynamics of an electromagnetic mode that cannot contain n photons. Science, 348(6236):776–779, 2015.

[152] N. Gisin, G. Ribordy, W. Tittel, and H. Zbinden. Quantum cryptography. Rev. Mod. Phys., 74(1):145, 2002.

[153] R. Barends, J. Kelly, A. Megrant, A. Veitia, D. Sank, E. Jeffrey, T. White, J. Mutus, A. Fowler, B. Campbell, Y. Chen, Z. Chen, B. Chiaro, A. Dunsworth, C. Neill, P. O/'Malley, P. Roushan, A. Vainsencher, J. Wenner, A. N. Korotkov, A. N. Cleland, and J. M. Martinis. Superconducting quantum circuits at the surface code threshold for fault tolerance. Nature, 508(7497):500–503, 2014.

[154] T. Xia, M. Lichtman, K. Maller, A. W. Carr, M. J. Piotrowicz, L. Isenhower, and M. Saffman. Randomized benchmarking of single-qubit gates in a 2d array of neutral-atom qubits. Phys. Rev. Lett., 114(10):100503, 2015.

[155] R. H. Dicke. Coherence in spontaneous radiation processes. Phys. Rev., 93(1):99, 1954.

[156] F. T. Arecchi, E. Courtens, R. Gilmore, and H. Thomas. Atomic coherent states in quantum optics. Phys. Rev. A, 6(6):2211, 1972.

[157] A. Zeilinger, M. A. Horne, and D. M. Greenberger. Higher-order quantum entanglement. In Workshop on Squeezed States and Uncertainty Relations, volume 3135. NASA Conference Publication, 1992.

[158] Y. Lin, J. P. Gaebler, F. Reiter, T. R. Tan, R. Bowler, Y. Wan, A. Keith, E. Knill, S. Glancy, K. Coakley, A. S. Sørensen, D. Leibfried, and D. J. Wineland. Preparation of entangled states by hilbert space engineering. in preparation, 2015.

[159] W. C. Campbell, J. Mizrahi, Q. Quraishi, C. Senko, D. Hayes, D. Hucul, D. N. Matsukevich, P. Maunz, and C. Monroe. Ultrafast gates for single atomic qubits. Phys. Rev. Lett., 105(9):090502, 2010.

[160] J. Mizrahi, B. Neyenhuis, K. Johnson, W. Campbell, C. Senko, D. Hayes, and C. Monroe. Quantum control of qubits and atomic motion using ultrafast laser pulses. Appl. Phys. B, 114(1-2):45–61, 2014.